

ATOMIC STRUCTURE
AND NONELECTRONIC PROPERTIES
OF SEMICONDUCTORS

Influence of Segregation on the Composition
of GaAs_{1-x}Sb_x Solid Solutions Grown
by Liquid-Phase Epitaxy

Yu. F. Biryulin

*Ioffe Physicotechnical Institute, Russian Academy of Sciences,
Politekhnicheskaya ul. 26, St. Petersburg, 194021 Russia*

e-mail: biryulin@mail.ioffe.ru

Submitted June 17, 2002; accepted for publication June 19, 2002

Abstract—Physical and physicochemical processes potentially responsible for the gradient in the composition of the liquid phase in epitaxial growth of GaAs_{1-x}Sb_x films were analyzed. It is shown that gravity-induced liquation is the dominant mechanism in the case under consideration. © 2002 MAIK “Nauka/Interperiodica”.

When ternary solid solutions based on GaAs are grown, the introduced minority component has either a larger or smaller atomic weight compared to similar parameters of the host atoms (Ga and As). In the course of the liquid-phase epitaxy (LPE) of GaAs-based solid solutions, this circumstance may give rise to the gravity-induced height profile of the solution–melt composition. In addition, one has to take into account the effect of segregation phenomena, which occur owing to the state of pronounced nonequilibrium between the liquid and gas phases in the course of saturating the solution–melt.

The objective of this study was to gain insight into the effects of gravity and segregation during the LPE growth of GaAs_{1-x}Sb_x films from Ga-based solution–melts for various contents of Sb.

Film growth experiments were carried out using a Splav-4 LPE system with a sodium heat pipe. The radial and longitudinal variations in temperature did not exceed 0.1°C within the heated zone of the reactor, with a length of 300 mm and diameter of 80 mm. The graphite sample holder was of the three-level type and could accommodate three GaAs (111) substrates spaced vertically by 8 mm. The liquid-phase column itself was 30 mm high, had a free area of 10 × 15 mm², and was kept in the graphite sample holder for 1.5 h at 800°C in an atmosphere of flowing high-purity hydrogen with a flow rate of 8 l/h. Thereafter, the sliders were moved in order to separate the solution–melt into three thin zones each with a thickness of 2 mm; the solution–melt was then deposited onto substrates. The remaining (unutilized) part of the solution–melt column was poured off into a free cell of the graphite sample holder. Epitaxial layers were grown on substrates using conventional LPE. Batches 1, 2, and 3 of the samples correspond to the lower, middle, and upper levels in the arrangement of substrates in the sample holder (Table 1).

The Sb content in GaAs_{1-x}Sb_x epitaxial layers was determined from the photoluminescence (PL) spectra measured at room temperature. The accuracy of determining the position of the PL-line peak was ±1 meV. The dependence of the band gap on the composition of GaAs_{1-x}Sb_x solid solution reported previously [1] was used. The results of measurements are listed in Table 1. In the three runs, the liquid-zone column in a Ga–As–Sb system was formed for three different fixed weighed portions of the solution–melt.

It can be seen from Table 1 that, in all three runs, the antimony content (x) in the epitaxial layers formed at the lower (first) level of the sample holder exceeds this content in the layers crystallized at the upper levels. Relative variations in the composition of epitaxial layers ($\Delta x/x$) range from 2% (batch 1) to 3.4% (batch 3)

Table 1. Composition of solid phase in GaAs_{1-x}Sb_x epitaxial layers for three runs of growth experiments with different content of Sb in the liquid phase

No. of the run	The sample no. (no. of the level in the holder)	Position of the PL line peak, eV	Antimony content, x	Relative variation in the composition, %
1	3	1.269	0.091	2.17
	2	1.267	0.092	
	1	1.264	0.093	
2	3	1.199	0.133	2.96
	2	1.196	0.135	
	1	1.194	0.137	
3	3	1.138	0.174	3.40
	2	1.135	0.176	
	1	1.129	0.180	

Table 2. Physicochemical characteristics of Ga, Sb, and Bi in the liquid phase

Element	Surface tension, erg/cm ²	Surface energy, 10 ³ cal/mol
Ga	735	60–65
Sb	389	No data
Bi	390	42

and tend to increase as the average content of antimony in the solid phase increases.

Let us now direct our attention to the processes that occur in the solution–melt in the course of homogenization (during saturation of the liquid phase for 1.5 h at a fixed temperature). Since the column of the solution–melt arranged in the graphite sample holder was not enclosed from above in the case of saturation, the evaporation of highly volatile components of this solution–melt into the reactor’s gaseous phase evidently occurred. In a Ga–As–Sb system, arsenic and antimony are highly volatile components. The pressure of As vapors above the solid As phase is lower than that above liquid As since the rate of evaporation of As in the former case is lower [2]. The calculated As pressure at temperatures of 800 and 850°C is equal to 26 and 42 Torr, respectively. In this temperature range, arsenic evaporates in both its molecular (As₂) and atomic (As) forms [2]. The aforementioned results of calculations agree within an order of magnitude with the pressure of As vapors above both the Ga–As melt [3] and the (100) GaAs substrate [4]. At the same temperatures, the pressure of antimony vapors is lower than that of arsenic vapors by an order of magnitude [2]. In this situation, the free surface and surface region of the solution–melt column should be depleted in arsenic to a greater extent compared to depletion in antimony. If mixing of As and Sb in the liquid phase and their diffusion from the lower layers of the column during homogenization have no time to level off the evaporation process, the ratio of the As and Sb concentrations (N_{As}/N_{Sb}) should change in the direction of Sb excess. This would result in enrichment of the solid phase with antimony when the film is grown from the upper part of the solution–melt column.

Experimentally, the opposite situation is observed: the content of antimony in the layer grown at the first (lowest) level is higher than that in the layers grown at higher levels of the sample holder. Such a situation may take place if the work of gravity forces is not compensated completely by the processes occurring in the course of homogenization of the liquid phase.

Another approach (independent of the first one) is based on physical factors related to the surface segregation in a system consisting of the liquid and gas phases. Typically, such an approach involves several criteria [5]. In the case under consideration, two criteria are most appropriate; these are the criteria for the minima of the surface-tension and surface energies. If these two

criteria are fulfilled, the elements that have the lowest surface-tension energy and the lowest surface energy are accumulated in excess at the solution–melt surface. Table 2 lists the relevant physical characteristics of the elements that are constituents of the solution–melt. As can be seen, even when these factors are taken into account, the ratio of the As and Sb surface concentration is such that one may expect an excess of antimony in the surface region of the solution–melt, i.e., an excess of Sb at the upper level of the epitaxial structure.

A thermodynamic approach is also indicative of competition between two factors, one of which is related to diffusion ($D \propto \exp(-W/kT)$) and causes the entropy of the system to increase and the other is gravity-related and reduces the entropy ($\eta \propto T \exp(W/kT)$) (D is the diffusion coefficient, W is the activation energy, η is the dynamic viscosity, T is temperature, and k is the Boltzmann constant). In addition, it is well known that the diffusion coefficient decreases when a one-component system is replaced by a multicomponent one; in the latter case, this coefficient is reduced as the content of the minority component increases. In other words, the gradient of antimony concentration in the vertical liquid phase is preserved under the effect of gravity after 1.5-h saturation and homogenization of the solution–melt. For GaAs_{1-x}Sb_x, this results in a noticeable (up to several percent) difference in the solid-phase compositions of the samples that were grown from three zones of the solution–melt column whose height reaches 30 mm. This circumstance was used in order to obtain the GaAs/GaAs_{1-x}Sb_x photocathode structures with negative electron affinity and a narrow spectral-sensitivity band [6] for precise correspondence to the specified wavelength.

A similar phenomenon, referred to as gravity-related liquation, was observed when polycrystalline CdHgTe was melted in order to obtain single crystals [7]. In this case as well, the heavier component (cadmium telluride) was concentrated in the bottom part of the container, so that the composition of the ingot varied along its length. The required content of cadmium was attained only in a narrow part of the ingot.

The absence of the gravity effect [8] in the case of isovalent doping of GaAs with Bi in a Ga–As–Bi system can be caused by a number of factors, the main one of which is the larger (compared to Ga and As) atomic weight of the metal solvent Bi, which resulted in the fact that there were no significant variations in the galvanomagnetic properties of GaAs:Bi in a wide range of liquid-phase compositions (from 0 to 75% of Bi).

ACKNOWLEDGMENTS

I thank V.N. Karyaeu for performing the experiments and for providing me with the samples.

REFERENCES

1. Yu. F. Biryulin, R. R. Ichkitidze, V. K. Krigel', and Yu. V. Shmartsev, *Fiz. Tekh. Poluprovodn. (Leningrad)* **13** (6), 1235 (1979) [*Sov. Phys. Semicond.* **13**, 727 (1979)].
2. A. N. Nesmeyanov and R. A. Sokolik, *Methods of Organoelemental Chemistry (Boron, Aluminum, Gallium, Indium, Thallium)* (Nauka, Moscow, 1964).
3. J. R. Arthur, *J. Phys. Chem. Solids* **28**, 2257 (1967).
4. J. Ohsawa, K. Ikeda, K. Takahashi, and W. Susaki, *Jpn. J. Appl. Phys.* **21** (1), L49 (1982).
5. A. A. Shebzukhov, *Poverkhnost'*, No. 8, 13 (1983).
6. Yu. F. Biryulin, V. N. Karyaev, and O. F. Lepekhin, *Pis'ma Zh. Tekh. Fiz.* **20** (16), 29 (1994) [*Tech. Phys. Lett.* **20**, 657 (1994)].
7. L. N. Kurbatov, *Prikl. Fiz.*, No. 3, 5 (1999).
8. S. V. Novikov, I. G. Savel'ev, M. Panek, *et al.*, *Pis'ma Zh. Tekh. Fiz.* **19** (14), 70 (1993) [*Tech. Phys. Lett.* **19**, 462 (1993)].

Translated by A. Spitsyn

ELECTRONIC
AND OPTICAL PROPERTIES
OF SEMICONDUCTORS

Temperature Dependence of the Width of the Deep-Level Band in Silicon with a High Concentration of Defects

J. Partyka*, P. W. Żukowski*, P. Węgierek*, A. Rodzik*,
Yu. V. Sidorenko**, and Yu. A. Shostak**

* Lublin Technical University, 20-618 Lublin, Poland

** Belarussian State University, ul. Leningradskaya 14, Minsk, 220080 Belarus

e-mail: pawel@elektron.pol.lublin.pl

Submitted February 28, 2002; accepted for publication March 19, 2002

Abstract—Temperature dependences of the peak location and the half-width of the absorption band related to neutral divacancies in the spectrum of Si irradiated with neutrons at a dose of 10^{19} cm⁻² were studied. The results were analyzed in terms of the concept of the defect-level band, whose width depends on the degree of compensation and on temperature. © 2002 MAIK “Nauka/Interperiodica”.

1. INTRODUCTION

Formation of impurity bands is typical of semiconductors containing high concentrations of shallow-level impurities. In semiconductors doped with shallow-level impurities of the same type, the formation of an impurity band first results in a decrease in the ionization energy. A further increase in the impurity concentration leads to degeneracy. In compensated semiconductors, the impurity band undergoes an additional broadening at low temperatures, which is caused by fluctuations of the electrostatic potential [1].

In Si irradiated with high doses of fast neutrons [2–4] and ions [5], compensation by radiation defects results in an exchange of charges between neutral defects via the hopping mechanism. Most radiation defects in Si are amphoteric, and their main charge state is the neutral state [6]. In this context, the compensation by such defects differs from the compensation in the case of simultaneous doping by shallow-level donors and acceptors, for which the degree of compensation $K_{sh} = N_d/N_a$ (for an *n*-type semiconductor, in which $N_d > N_a$).

This means that the concentration of positively charged donors in a doped compensated *n*-type semiconductor equals the concentration of negatively charged acceptors at low temperatures, and the number of donors that are in the neutral charge state amounts to $N_d - N_a$. The concentrations of shallow-level donors and acceptors should be nearly equal in order to obtain a high degree of compensation.

In the case of compensation by amphoteric deep-level defects using irradiation with high doses of neutrons, the following condition is fulfilled:

$$N_D > N_{sh}, \quad (1)$$

where N_D is the concentration of amphoteric defects and N_{sh} is the concentration of shallow-level impurities.

It follows from inequality (1) that amphoteric deep-level impurities cause no overcompensation at low temperatures. When $N_D > N_d$, all electrons are transferred from donor levels to deep levels of defects, and a further increase in the N_D concentration results in an increase in the concentration of defects in the neutral charge state.

In this context, in the absence of hopping charge exchange, heavily irradiated *n*-Si ($N_D \gg N_d$) is only slightly compensated by amphoteric deep-level defects, because

$$\frac{N_d}{N_D} \ll 1. \quad (2)$$

There is an additional decrease in the degree of compensation due to the formation of irradiation-induced impurity-defect complexes, for example, a phosphorus-vacancy complex. Such complexes, being deep-level centers, reduce the concentration of shallow-level donors. In this case, the degree of compensation of heavily irradiated Si can be written as

$$K_{ir} \ll \frac{N_d}{N_D} \ll 1. \quad (3)$$

Inequality (3) means that the degree of compensation of Si with a high concentration of defects cannot be expressed as N_d/N_D and should be sought in another form.

It has been shown [5, 7] that the hopping exchange of electrons between neutral amphoteric deep-level defects gives rise to pairs of positively and negatively charged defects. The concentrations of such pairs are given by

$$N^+ = N^- = \frac{N_D P(T) \tau}{2P(T) \tau + 1}, \quad (4)$$

where $P(T)$ is the probability of the hopping charge exchange, which can be written, for example, in the form suggested in [8]; and τ is the lifetime of a defect in a charge state.

Then we have

$$K_{ir}(T) = \frac{N^+}{N_D} = \frac{P(T)\tau}{2P(T)\tau + 1}. \quad (5)$$

As can be seen from (5), in Si compensated by amphoteric deep-level defects, the degree of compensation is a function of temperature T , because $P(T)$ and τ depend on temperature. The impurity-band width depends both on the impurity concentration and on the degree of compensation [9].

Fluctuations of the electrostatic potential in a semiconductor can be described by the mean effective magnitude B . In accordance with [10],

$$B \approx \frac{e^2(N_a + N_d)^{2/3}}{\chi(N_a - N_d)^{1/3}}. \quad (6)$$

In the case under consideration, $N_a + N_d \approx N_D$ and $N_a - N_d$ is the concentration of defects in the neutral charge state. In accordance with [7],

$$N_0 = N_a - N_d = \frac{N_D}{2P(T)\tau + 1}. \quad (7)$$

Then,

$$B \approx \frac{e^2 N_D^{1/3} [2P(T)\tau + 1]^{1/3}}{\chi}. \quad (8)$$

The energy distribution of deep centers in the impurity band [10] can be written as

$$N(E) = \frac{N_D}{\sqrt{2\pi}B} \exp\left(\frac{-E^2}{2B^2}\right), \quad (9)$$

where the energy E is reckoned from the middle of the deep-level band. Substitution of expression (8) for B into (9) yields

$$N(E) = \frac{N_D^{2/3} \chi}{\sqrt{2\pi} e^2 [2P(T)\tau + 1]^{1/3}} \times \exp\left[-\frac{E^2}{2} \left(\frac{\chi}{e^2 N_D^{1/3} [2P(T)\tau + 1]^{1/3}}\right)^2\right]. \quad (10)$$

The half-width of the deep-level band can be written as

$$\begin{aligned} \Delta E(T) &= \sqrt{8 \ln 2} B \\ &= \sqrt{8 \ln 2} \frac{e^2 N_D^{1/3} [2P(T)\tau + 1]^{1/3}}{\chi}, \end{aligned} \quad (11)$$

or, taking into account (5), as

$$\begin{aligned} \Delta E(T) &= \sqrt{8 \ln 2} \frac{e^2 N_D^{1/3}}{\chi(1 - 2K_{ir})^{1/3}} \\ &= \Delta E(0)(1 - 2K_{ir})^{-1/3}. \end{aligned} \quad (12)$$

Here, $\Delta E(0)$ is the band half-width in the absence of compensation and at temperatures close to absolute zero. Thus, $\Delta E(0)$ may be regarded as the inherent half-width of the deep-level band; this half-width results from the interaction between similar defects. The electrostatic interaction between defects and atoms of shallow-level impurities, as well as the change in the charge state of the defects due to the hopping exchange by electrons, should result, as can be seen from (12), in additional band broadening.

2. EXPERIMENTAL RESULTS AND DISCUSSION

Divacancies are among the dominant intrinsic amphoteric defects in Si heavily irradiated with neutrons [11]. The production rate of divacancies is about 1 cm^{-1} [12]. Therefore, for the irradiation dose we used (10^{19} cm^{-2}), the concentration of divacancies far exceeds that of impurity-atom-defect complexes that include atoms of both shallow-level and residual impurities [13]. The infrared-absorption band around $1.8 \mu\text{m}$ is related to divacancies in the neutral charge state. In this study, we measured the infrared transmission and reflectance spectra of Si with a concentration of shallow-level donors of about 10^{14} cm^{-3} . The spectra were recorded using a double-beam spectrometer with PC storage. Both the transmittance and reflectance were measured with an error no greater than 0.03%. The measurements were performed in the temperature range of 77–420 K. The sample temperature was maintained at a preset value with an accuracy of $\pm 2 \text{ K}$.

Figure 1 shows the spectral dependences of the transmittance and absorption coefficient measured at different temperatures. The absorption coefficient α was calculated using the formula reported in [14], which accounts for multiple reflections from both surfaces of a sample:

$$\tilde{T} = \frac{(1 - R)^2 \exp(-\alpha d)}{1 - R^2 \exp(-2\alpha d)}. \quad (13)$$

Here, d is the sample thickness, \tilde{T} is the transmittance, and R is the reflectance.

Generally, when $\alpha(E)$ is calculated, tabulated data for the reflectance $R(E)$ are used. Such data can be found, for example, in [15].

The value of $R(E)$ depends both on the quality of the surface treatment and on the irradiation conditions. Therefore, when calculating the absorption coefficients of irradiated Si samples, we used the experimentally determined dependences $R(E)$ for similarly treated irra-

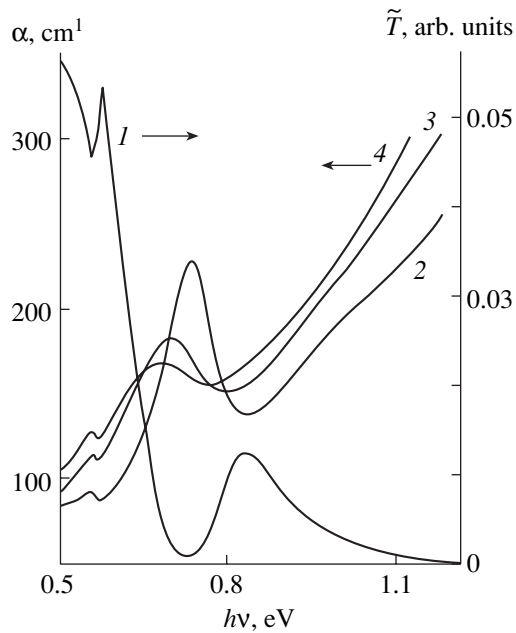


Fig. 1. (1) Transmission and (2–4) absorption spectra of Si irradiated with fast reactor neutrons at a dose of 10^{19} cm^{-2} ; the spectra were measured at (1, 2) 77, (3) 293, and (4) 413 K.

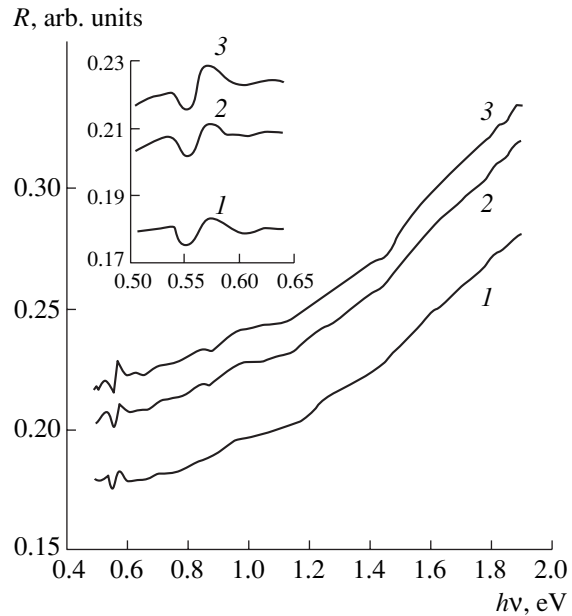


Fig. 2. Spectral dependences of reflectance of neutron-irradiated Si at (1) 77, (2) 293, and (3) 413 K.

diated samples that were much thicker ($d = 0.3$ and 2.5 mm for the samples used in the measurements of the transmission and absorption spectra, respectively). Examples of reflection spectra recorded at different temperatures are shown in Fig. 2. In the studied spectral region, we observed two absorption lines: a wide line peaked at ~ 0.7 eV (related to absorption by neutral divacancies) and a narrow line peaked at ~ 0.56 eV with a half-width of ~ 0.02 eV. In addition, near-edge absorption was also observed. In order to determine the main parameters of the absorption band related to divacancies (the peak location E_w and the band half-width ΔE_w), we subtracted the value of the near-edge-absorption coefficient (that may affect E_w and ΔE_w) from $\alpha(E)$. The values of E_w and ΔE_w , determined in this way, are shown as functions of temperature in Figs. 3 and 4, respectively.

As can be seen from Fig. 3, in the temperature range of 77–420 K, E_w first decreases sublinearly with an increase in T (up to ~ 200 K) and then decreases virtually linearly with a further increase in T . In the range of 200–420 K, the temperature coefficient of variation in the band-peak location is about $(-2.1 \pm 1.5) \times 10^{-4} \text{ eV K}^{-1}$. The value of E_w changes with temperature in the same way as the bandgap does (the latter decreases with temperature nonlinearly at $T < 220$ K and linearly at $T > 220$ K). The temperature coefficient of variation in ΔE_g amounts to $-2.84 \times 10^{-4} \text{ eV K}^{-1}$ [16].

It is generally agreed that the absorption band around 0.7 eV is related to intracenter electronic-vibrational transitions in neutral divacancies.

If we assume that the absorption band around 0.7 eV is related to transitions of electrons from the levels of the ground state of neutral divacancies, a considerable portion of the band half-width (about 0.1–0.12 eV, see Fig. 4) is due to the formation of a band by the deep levels of divacancies. As can be seen from Fig. 4, the half-width of the divacancy-absorption band increases with temperature at $T > 100$ K, remains constant in the range of 250–350 K, and decreases with temperature at $T > 350$ K. Thus, both the location of the peak of the deep-level band and the band width depend on temperature.

For the irradiation dose we used, divacancies are prevalent defects. Therefore, hopping exchange of electrons occurs between neighboring neutral divacancies. It follows from formula (11) that at sufficiently low temperatures, when the probability of hopping exchange is low (i.e., $P(T)\tau \approx 0$), the inherent width of the deep-level band $\Delta E(0)$ depends on the defect concentration N_D . Assuming that $P(T)\tau = 0$ in (11), we find a correlation between the inherent width of the deep-level band and the defect concentration

$$N_D = \left(\frac{\Delta E(0)\chi}{\sqrt{8 \ln 2} e^2} \right)^3. \quad (14)$$

Formula (14) allows us to calculate the defect concentration using the results of low-temperature measurements of the half-width $\Delta E(0)$ of the absorption line.

As can be seen from Fig. 4, $\Delta E(0) = 0.10$ eV for neutral divacancies at $T = 77$ K. In accordance with (14), the divacancy concentration of about $4 \times 10^{19} \text{ cm}^{-3}$ corresponds to this value of $\Delta E(0)$. This is consistent with

the results of the spectroscopic measurements reported in [12].

Bourgoin and Lannoo [17] obtained an expression that makes it possible to estimate approximately the impurity-band width:

$$\Delta E \approx \frac{2e^2}{\chi R}, \quad (15)$$

where $R \approx N_D^{-1/3}$ is the average distance between impurity atoms or defects. In accordance with formula (15), the width of the deep-level band of about 0.1 eV corresponds to the divacancy concentration of $4 \times 10^{19} \text{ cm}^{-3}$ (the result of our calculations using formula (14) on the basis of the experimental data). Thus, the model we developed is in good agreement with the known data [17] for low temperatures, in which case $\Delta E = \text{const}$. Our taking into consideration the degree of compensation and temperature results in an additional broadening of the impurity band (see formula (12)). When the degree of compensation is close to 0.5, the band width may increase several times in comparison with the situation where there is no compensation at low temperatures.

Divacancies introduce different levels (four in total) into the band gap, depending on the divacancy charge state. The levels $E_v + 0.21 \text{ eV}$ ($E_c - 0.94 \text{ eV}$) and $E_c - 0.39 \text{ eV}$ correspond to the positive and negative charge states, respectively; and the level $E_c - 0.22 \text{ eV}$ corresponds to the doubly negative charge state [13, 17].

The band of levels corresponding to the neutral charge state of divacancies is located between the levels of the positive and negative charge states. Depending on temperature, the band-peak location ranges from $E_c - 0.72 \text{ eV}$ at $T = 77 \text{ K}$ to $E_c - 0.67 \text{ eV}$ at $T = 400 \text{ K}$ (see Fig. 3). Notably, the half-width of the neutral-divacancy band (Fig. 4) is only a few times smaller than the energy intervals between the band peak and the levels of positive (for $\Delta E(0/+) = 0.18 \text{ eV}$) and negative (for $\Delta E(0/-) = 0.33 \text{ eV}$) charge states. This means that, for a Gaussian distribution of neutral-divacancy levels over energies (11), a certain portion of these levels is located above the negative-divacancy level and another portion is located below the positive-divacancy level. Thus, even at low temperatures, when the probability of hopping recharge is zero, a certain portion of neutral divacancies is in the positive and negative charge states due to the formation of the band of neutral-divacancy levels. In this case, the concentration of charged divacancies can be determined from the formula

$$N(\pm) = \sqrt{\frac{4 \ln 2}{\pi}} \frac{N_D}{\Delta E(T)} \int_{-\infty}^{c(\pm)} \exp\left(-\frac{\xi^2}{2}\right) d\xi, \quad (16)$$

where

$$c(+)= -\sqrt{8 \ln 2} \frac{\Delta E(0/+)}{\Delta E(T)} \quad (17)$$

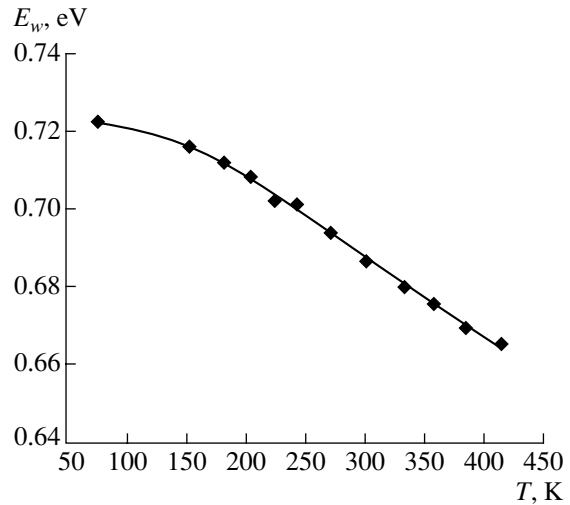


Fig. 3. Position of the peak of the divacancy-related absorption band in neutron-irradiated Si as a function of temperature.

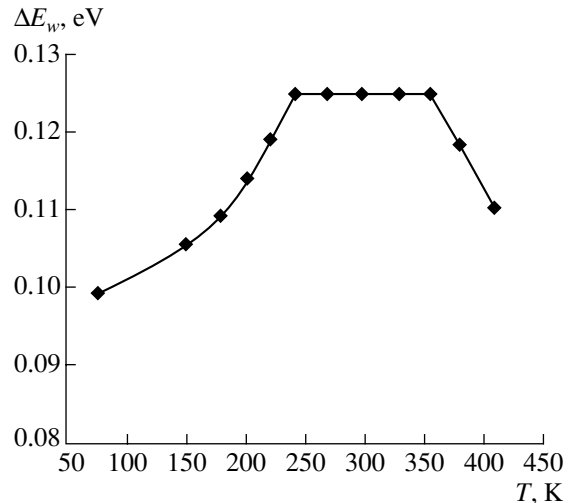


Fig. 4. Temperature dependence of the width of the absorption band related to divacancies in neutron-irradiated Si.

for positive divacancies and

$$c(-) = -\sqrt{8 \ln 2} \frac{\Delta E(0/-)}{\Delta E(T)} \quad (18)$$

for negative divacancies.

The calculations based on formulas (16)–(18) showed that, at $N_D = 4 \times 10^{19} \text{ cm}^{-3}$, $N(+)$ is about 10^{15} cm^{-3} at liquid-nitrogen and lower temperatures and becomes as high as approximately $1 \times 10^{16} \text{ cm}^{-3}$ at room temperature. The concentration of negative divacancies is about $2.5 \times 10^6 \text{ cm}^{-3}$ at low temperature and increases to $\sim 10^{11} \text{ cm}^{-3}$ at room temperature. Thus, in crystals containing a region with clusters of defects introduced by neutron irradiation, a small portion of divacancies may undergo transition to positive- and negative-charge states even at low temperatures. The degree of compen-

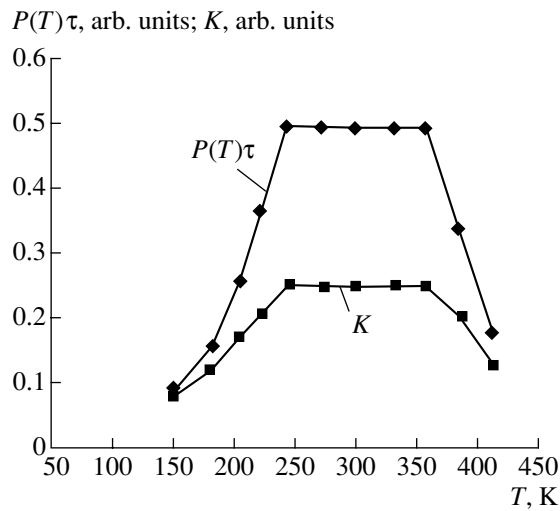


Fig. 5. Temperature dependences of the $P(T)\tau$ product (15) and the degree of compensation K_{ir} (5).

sation is about 2.5×10^{-5} in these conditions. At temperatures above the liquid-nitrogen temperature, hopping charge exchange between neutral divacancies occurs, which results in an additional broadening of the impurity band (Fig. 4).

When the degree of compensation differs from zero (which is typical of higher temperatures, for example, room temperature), formula (11) allows us to determine the product of the probability of hopping recharge $P(T)$ and the lifetime of a defect in a charge state τ

$$P(T)\tau = \frac{1}{2} \left[\left(\frac{\Delta E(T)}{\Delta E(0)} \right)^3 - 1 \right]. \quad (19)$$

The calculations of the $K_{ir}(T)$ and $P(T)\tau$ values performed on the basis of the experimental temperature dependence of ΔE_w using formulas (5) and (19) are shown in Fig. 5. As can be seen, the degree of compensation becomes as high as 0.23 at $T = 300$ K; i.e., the concentration of defects in charge states is about $0.46N_D$. A further increase in temperature to $T = 350$ K virtually does not affect the half-width of the absorption band and the degree of compensation. At $T > 350$ K, the values of $K_{ir}(T)$ and $P(T)\tau$ decrease with temperature.

The probability of hopping recharge $P(T)$ should increase with temperature. In our opinion, the observed decrease in $P(T)\tau$ and $K_{ir}(T)$ at $T > 350$ K is related to the heterogeneous structure of neutron-irradiated Si. It is known [6] that irradiation of this kind induces divacancies to agglomerate mainly in the regions containing clusters, where the divacancy concentration can be as high as 10^{20} cm^{-3} . The concentration of divacancies outside the cluster regions is much lower. As a result, the hopping exchange sets in exactly in cluster regions. When nearly all defects become charged in these regions, neutral divacancies remain only outside cluster regions. Since the concentration of divacancies in the

less damaged regions is much lower than that in cluster regions, in accordance with formulas (11) and (12), the half-width of the absorption band related to neutral divacancies should decrease at $T > 350$ K.

The formula for the static dielectric susceptibility related to the hopping exchange of electrons between neutral amphoteric defects contains the $P(T)\tau$ product [5]:

$$\chi_p = \frac{N_D P(T)\tau e^2 R^2}{\epsilon_0 k T}. \quad (20)$$

On the basis of measurements of the width of the optical-absorption line related to neutral divacancies (Fig. 4) and with the use of (19), we can determine the $P(T)\tau$ product in formula (20). This formula describes the temperature dependence of the additional polarization of semiconductors with high concentrations of defects. We carried out direct room-temperature measurements of the permittivity of an Si sample (similar to that which we used in the aforementioned optical measurements) at a frequency of 100 Hz to obtain the value of $\chi_p \approx 50$. Substitution of the N_D and $P(T)\tau$ values (formulas (14) and (19), respectively), which were calculated on the basis of the data derived from the absorption spectra recorded at $T = 300$ K (Fig. 3), into (20) yields $\chi_p \approx 70$, which is in good agreement with the value obtained from the direct measurements.

3. CONCLUSION

We have shown that hopping charge exchange results in the formation of dipoles in semiconductors compensated by amphoteric deep-level defects. These dipoles lead to an increase in fluctuations of the electrostatic potential and to broadening of the band formed by deep levels of the main (neutral) state of defects. These phenomena may manifest themselves in a variation in the width of the optical-absorption band related to neutral defects. The temperature dependence of the width of the infrared-absorption band related to neutral divacancies was studied for Si irradiated with fast reactor neutrons at a dose of 10^{19} cm^{-2} . The value of the band half-width was used to evaluate the divacancy concentration (it was found to be $4 \times 10^{19} \text{ cm}^{-3}$) and the dielectric susceptibility of the irradiated sample ($\chi_p \approx 70$). The obtained values are in agreement with the results of the direct measurements.

REFERENCES

1. B. I. Shklovskii and A. L. Efros, *Electronic Properties of Doped Semiconductors* (Nauka, Moscow, 1979; Springer-Verlag, New York, 1984).
2. P. W. Żukowski, S. B. Kantorow, K. Kiszczak, *et al.*, *Phys. Status Solidi A* **128**, K117 (1991).
3. P. W. Żukowski, S. B. Kantorow, D. Monchka, *et al.*, *Dokl. Akad. Nauk Belarusi* **37** (1), 41 (1993).

4. P. Żukowski, J. Partyka, P. Węgierek, and M. Kozak, *Nukleonika* **44**, 281 (1999).
5. P. Żukowski, J. Partyka, and P. Węgierek, *Phys. Status Solidi A* **159**, 509 (1997).
6. L. Cheng and I. Lori, *Phys. Rev.* **171**, 856 (1968).
7. P. W. Żukowski, A. Rodzik, and Yu. A. Shostak, *Fiz. Tekh. Poluprovodn. (St. Petersburg)* **31**, 714 (1997) [*Semiconductors* **31**, 610 (1997)].
8. S. Kirkpatrick, in *Proceedings of the 5th International Conference on Amorphous and Liquid Semiconductors, Garmisch-Partenkirchen, 1973*, Ed. by J. Stuke and W. Brenig (Taylor & Francis, London, 1974), p. 183.
9. B. I. Shklovskii and A. L. Éfros, *Zh. Éksp. Teor. Fiz.* **60**, 867 (1971) [*Sov. Phys. JETP* **33**, 468 (1971)].
10. M. A. Messerer, É. M. Omel'yanovskii, A. N. Pantyukhov, *et al.*, *Fiz. Tekh. Poluprovodn. (Leningrad)* **8**, 2279 (1974) [*Sov. Phys. Semicond.* **8**, 1491 (1974)].
11. R. S. Newman and D. M. J. Totterdell, *J. Phys. C* **8**, 3944 (1975).
12. P. V. Zhukovskii, S. B. Kantorov, V. F. Stel'makh, *et al.*, *Fiz. Tekh. Poluprovodn. (Leningrad)* **24**, 1473 (1990) [*Sov. Phys. Semicond.* **24**, 922 (1990)].
13. V. S. Vavilov, V. F. Kiselev, and B. N. Mukashev, *Defects in the Bulk and at the Surface of Silicon* (Nauka, Moscow, 1990).
14. J. I. Pankove, *Optical Processes in Semiconductors* (Prentice-Hall, Englewood Cliffs, 1971).
15. V. I. Gavrilenko, A. M. Grekhov, D. V. Korbutyak, and V. G. Litovchenko, *Optical Properties of Semiconductors: a Handbook* (Naukova Dumka, Kiev, 1987).
16. V. V. Pasynkov and V. S. Sorokin, *Materials for Electronic Engineering* (Vysshaya Shkola, Moscow, 1986).
17. J. Bourgoin and M. Lannoo, *Point Defects in Semiconductors* (Springer-Verlag, New York, 1983; Mir, Moscow, 1985).

Translated by Yu. Sin'kov

ELECTRONIC
AND OPTICAL PROPERTIES
OF SEMICONDUCTORS

The Mechanisms of Hole Scattering
in p -Hg_{0.8}Cd_{0.2}Te Crystals
at Low Temperatures

V. V. Bogoboyashchii

Kremenchug State Polytechnical University, Kremenchug, 39614 Ukraine

Submitted February 19, 2002; accepted for publication March 28, 2002

Abstract—The resistivity and Hall effect were investigated in p -Hg_{0.8}Cd_{0.2}Te crystals that contained from 1.5×10^{15} to 1.7×10^{18} cm⁻³ Cu atoms. The measurements were carried out in the temperature range of 4.2–100 K. It is demonstrated that, in order to correctly determine the Hall mobility of holes at low temperatures, one should exclude the contribution of hopping charge transfer. It was found that heavy holes are scattered at 77 K by each other, by impurity ions, by composition fluctuations, and by lattice vibrations. In compensated crystals, holes are scattered only by lattice vibrations at low temperatures. For uncompensated crystals, when calculating the mobility, it is necessary to make allowance for the hole scattering by positively charged centers formed due to trapping of excess holes by acceptors. © 2002 MAIK “Nauka/Interperiodica”.

1. INTRODUCTION

As many researchers believe, the mobility μ_h of free holes in p -Hg_{0.8}Cd_{0.2}Te crystals at low temperatures is substantially lower than expected for scattering by impurity ions [1–3]. Various explanations have been suggested for this phenomenon. However, none of them can be accepted as satisfactory. For example, low hole mobilities were explained by scattering at elastic fields of neutral defects [1] and by scattering at composition fluctuations [2]. At the same time, μ_h is proportional to $T^{3/2}$ at $T < 15$ K, which corresponds to scattering precisely by charged centers and is inconsistent with the mechanisms suggested in [1, 2]. Tsidil'kovskii *et al.* [3] believe that at low temperatures the holes that contribute to charge transport are in the tail of the density of states of the valence band. Because of this, the dynamic properties of holes can in no way be characterized by the band effective mass. It is also believed [3] that the energy of interaction between the holes and scattering centers is not low compared with their kinetic energy. As a result, the classical concepts of mobility are inapplicable in this case. The question of the angular dependence of overlapping intensity also remains open. This dependence is written as $I_{\alpha}(\mathbf{k}', \mathbf{k}) = \int d^3 r u_{\alpha\mathbf{k}'}^* u_{\alpha\mathbf{k}}$, where $u_{\alpha\mathbf{k}}$ is the periodic part of the Bloch wave function for the α th branch of the spectrum, and integration is carried out over the unit-cell volume. On the one hand, it is generally agreed that for holes $I_h^2(\mathbf{k}', \mathbf{k}) = (1 + 3 \cos^2 \theta_{\mathbf{k}})/4$, where $\theta_{\mathbf{k}}$ is the angle between the vectors \mathbf{k} and \mathbf{k}' (see [3, 4]). On the other hand, $u_{hh\mathbf{k}} = u_{hh0}$ in the Kane model; because of this, $I_h(\mathbf{k}', \mathbf{k}) = 1$.

For these reasons, the concentration and temperature dependences of the mobility of free holes in Cu-doped uncompensated and In-compensated p -Hg_{0.8}Cd_{0.2}Te at $T < 100$ K under the conditions of light and moderate doping were investigated.

2. EXPERIMENTAL

Single-crystal n -Hg_{1-x}Cd_xTe ($x = 0.21 \dots 0.22$) wafers with a thickness of $d \approx 0.1$ cm were used in the experiment. The wafers were cut from ingots grown by vertical planar crystallization with a solid-phase feeding in batch production. The wafers were annealed in saturated Hg vapors. The dislocation density in the wafers was lower than 3×10^5 cm⁻².

Most starting ingots were manufactured using components of 99.9999% and 99.99999% purity and contained background impurities only. For annealed wafers of this type, the extrinsic-electron density at low temperatures was no higher than 3×10^{14} cm⁻³. Several crystals were doped with In from the melt and contained from 10^{15} to 1.6×10^{17} cm⁻³ excess donors. The In concentration N_{In} in such samples was identified with the extrinsic-electron density at $T = 77$ K, which was determined from the Hall coefficient R_H in a magnetic field of $B = 1$ T.

The p -type samples were obtained from the starting wafers by diffusion doping with Cu. A Cu film of specified thickness was deposited onto the wafer surface by resistive evaporation in vacuum. The amount of evaporated Cu and the distance from the source to the sample were chosen such that the required concentration N_{Cu} of active Cu was attained after the film dissolved. The Cu

diffusion was carried out during the isothermal annealing of the wafers in saturated Hg vapors. The annealing time t was chosen from the condition $\sqrt{D_{\text{Cu}}t} > 5d$, where D_{Cu} is the Cu diffusivity. The values of D_{Cu} for Hg_{0.8}Cd_{0.2}Te determined in [5] were used. In this case, the Cu distribution in the crystals was fairly uniform.

In the case of relatively light doping ($N_{\text{Cu}} < 7 \times 10^{17} \text{ cm}^{-3}$), the Cu diffusion was carried out at 473 K for 72 h. According to [6], the Cu solution is quite stable at $T \approx 300 \text{ K}$ in this case. More concentrated Cu solutions in stoichiometric crystals are unstable and are prone to rapid decomposition. Because of this, heavily doped samples were annealed at higher temperatures (670–680 K). In this case, about 10^{16} cm^{-3} Hg vacancies were introduced into the samples. This stabilized the Cu solution due to a decrease in the Cu-migration rate [7]. At the same time, the number of vacancies in such samples is small compared with the number of Cu atoms, and the vacancies exert no effect on the hole mobility.

As a result, a series of uniformly doped p -Hg_{1-x}Cd_xTe crystals containing from 1.5×10^{15} to $1.7 \times 10^{18} \text{ cm}^{-3}$ dissolved active Cu atoms were obtained. The number of active Cu atoms in uncompensated crystals was identified with the number of free holes p at 77 K, since such defects are ionized completely under these conditions, while background donors and acceptors in the material under investigation were mutually compensated. The Cu concentration in In-compensated p -type samples was determined from the electroneutrality condition in the form $N_{\text{Cu}} = p + N_{\text{In}}$.

Several uncompensated samples that contained $3.5 \times 10^{16} \text{ cm}^{-3}$ active Cu atoms were additionally annealed at various temperatures and Hg-vapor pressures. The annealing conditions were chosen such that the equilibrium concentration of intrinsic acceptors (V_{Hg} vacancies) in these samples was about $1.8 \times 10^{16} \text{ cm}^{-3}$. The annealing conditions, the methods of determining the V_{Hg} concentration, and the temperature dependences of the conductivity and Hall effect were reported in detail in [8].

The mobility and density of electrons and holes were determined by the six-probe Hall method. Samples shaped as rectangular parallelepipeds of about $1.2 \times 0.3 \times 0.1 \text{ cm}^3$ in size were cut from the wafer, and their resistivity σ and Hall coefficient R_H were measured. The measurements were carried out either at a fixed temperature of 77 K in a magnetic field B ranging from 0.5 to 2 T or in the temperature range from 4.2 to 125 K in a fixed field of $B = 0.030 \text{ T}$.

In order to calculate the concentration p and the mobility μ_h of heavy holes in p -type samples at 77 K, the R_H values for magnetic fields that are strong with respect to light holes were used. The dependence $R_H(B)$, obtained for B in the range from 0.5 to 2 T, was

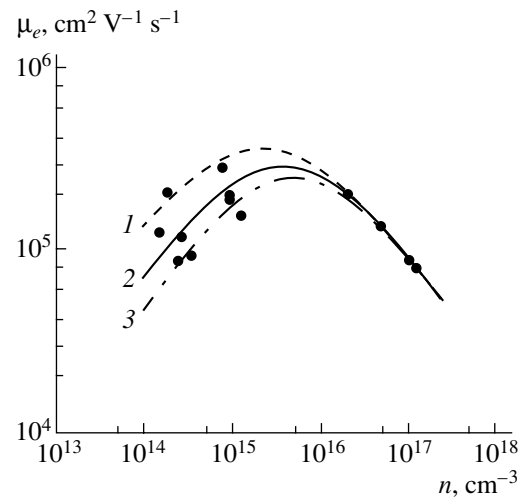


Fig. 1. Electron mobility in the n -Hg_{0.78}Cd_{0.22}Te:In crystals at 4.2 K. Circles and lines represent the results of measurements and calculations, respectively. $N_A = (1) 0.5 \times 10^{15}$, (2) 1×10^{15} , and (3) $1.5 \times 10^{15} \text{ cm}^{-3}$.

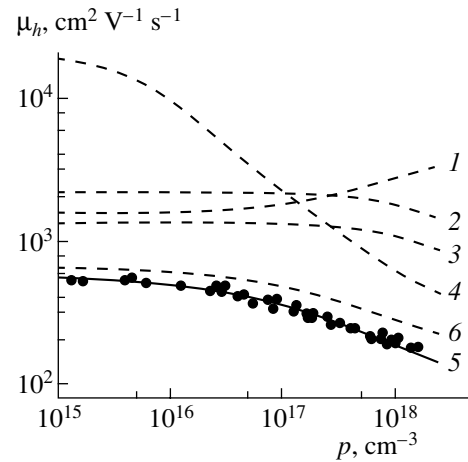


Fig. 2. Mobility of heavy holes in the p -Hg_{0.8}Cd_{0.2}Te:Cu crystals at 77 K. Circles correspond to experimental data. Lines represent the results of calculations for $I_h = (1-5) 1$ and (6) $1 - (3/4)\sin^2\theta_{\mathbf{k}}$. (1) Mobility limited by scattering at polar optical phonons; (2) mobility limited by scattering at composition fluctuations; (3) mobility limited by scattering at acoustic phonons; (4) mobility limited by scattering at charged centers; and (5), (6) total mobility.

extrapolated to the region of $B > 3 \text{ T}$. According to [9], the presence of light holes in such fields does not affect the value of R_H . For correct extrapolation, the $R_H(B)$ dependence was represented as a polynomial in degrees of B^{-2} . Relevant examples were reported in [9]. It was assumed that the Hall factor for heavy holes $r_H^{(hh)} \approx 1.02$ [9].

The concentration dependences of the electron mobility for n -type crystals at 4.2 K and the heavy-hole mobility for uncompensated p -type crystals at 77 K are shown in Figs. 1 and 2, respectively.

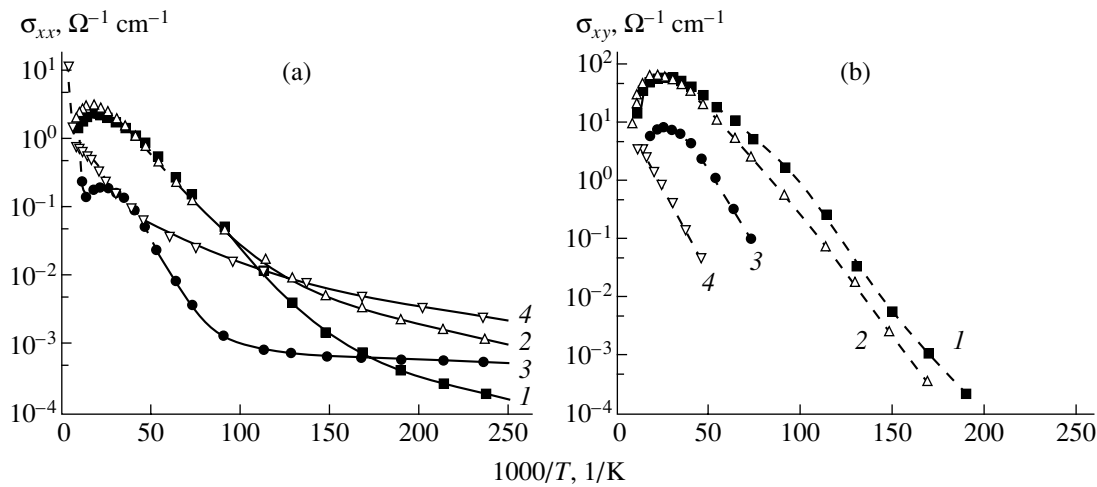


Fig. 3. Temperature dependences of (a) diagonal and (b) off-diagonal components of the electrical-conductivity tensor for $p\text{-Hg}_{0.78}\text{Cd}_{0.22}\text{Te}$ crystals. Circles, squares, and triangles correspond to experimental data; solid and dashed lines represented the results of fitting and interpolation, respectively. (1) $N_{\text{Cu}} = 3.5 \times 10^{16} \text{ cm}^{-3}$, $N_{\text{In}} < 10^{15} \text{ cm}^{-3}$, $[V_{\text{Hg}}] < 10^{14} \text{ cm}^{-3}$; (2) $N_{\text{Cu}} = 3.5 \times 10^{16} \text{ cm}^{-3}$, $N_{\text{In}} < 10^{15} \text{ cm}^{-3}$, $[V_{\text{Hg}}] = 1.8 \times 10^{16} \text{ cm}^{-3}$; (3) $N_{\text{Cu}} = 1.5 \times 10^{15} \text{ cm}^{-3}$, $N_{\text{In}} < 10^{15} \text{ cm}^{-3}$, $[V_{\text{Hg}}] < 10^{14} \text{ cm}^{-3}$; (4) $N_{\text{Cu}} = 1.14 \times 10^{17} \text{ cm}^{-3}$, $N_{\text{In}} = 9.2 \times 10^{16} \text{ cm}^{-3}$, $[V_{\text{Hg}}] < 10^{14} \text{ cm}^{-3}$.

The temperature dependences of σ and R_H for several p -type samples were studied using a system described previously [10]. The sample temperature was determined from the reading of a calibrated resistance thermometer with an error of a few tenths of a percent. To reduce the degree of surface oxidation, the contacts were soldered in cooled N ambient onto the freshly etched samples and rinsed in warm deionized water. Then, the samples were immediately placed in a cryostat filled with He so as to perform σ and R_H measurements. During such treatment, the crystals had no time to oxidize noticeably, and no effect of surface electrons was observed. Indium contacts were used. According to [11], it is quite possible to regard such contacts as non-rectifying.

On the basis of the measurements of σ and R_H , the σ_{xx} and σ_{xy} components of the electrical-conductivity tensor were calculated. This form of representing the results is more convenient in the case of mixed conductivity. Since the magnetic field was extremely weak, it was assumed that $\sigma_{xx} = \sigma$ and $\sigma_{xy} = BR_H\sigma^2$.

Typical results obtained for various types of investigated $p\text{-Hg}_{0.8}\text{Cd}_{0.2}\text{Te}:\text{Cu}$ samples are shown in Fig. 3. It can be seen that ϵ_1 conduction is dominant at relatively high temperatures (above 10–15 K in slightly compensated crystals and above 20–30 K in the nearly completely compensated crystal). The conduction of this type is governed by the valence-band holes. In all cases, considerable hopping conductivity over the acceptor band is observed at lower temperatures. The magnitude and the type of hopping conductivity depend on the presence of Hg vacancies and compensating donors.

Specifically, in slightly compensated crystals (Fig. 3a, curve 1), hopping conductivity whose activation energy is independent of T is observed (ϵ_3 conduction):

$$\sigma_3 = \sigma_{30} \exp[-\epsilon_3/k_B T]. \quad (1)$$

In compensated samples (curves 3, 4), as well as in the sample with an appreciable concentration of Hg vacancies (curve 2), the hopping conductivity with a variable hop range (the Mott conductivity [12]) is observed:

$$\sigma_M = \sigma_{M0} \exp[-(T_0/T)^{1/4}]. \quad (2)$$

The sign of the Hall effect in the region of ϵ_1 conduction below the inversion point that is caused by freezing of intrinsic electrons is positive. At the same time, the temperature dependence of the off-diagonal component σ_{xy} of the conductivity tensor below 20–30 K, in contrast with $\sigma_{xx}(T)$, follows the activation law with a single activation energy. This is in good agreement with the theory of the hopping Hall effect [13, 14]. According to this theory, localized holes cannot generate a noticeable Hall voltage. For the same reason, the Hall effect was not detected in the region of pure hopping conductivity.

The Hall voltage in the $p\text{-Hg}_{0.8}\text{Cd}_{0.2}\text{Te}$ crystals is caused by light and heavy valence-band holes at low temperatures, whereas the conduction is caused by charge carriers localized at acceptors. Because of this, in order to determine the mobility of heavy holes μ_h

correctly, one should exclude the contributions of other charge carriers to σ_{xx} and σ_{xy} .

The effect of the hopping mechanism can be excluded relatively easily. Taking into account the additivity of the components of the electrical conductivity tensor, we assumed that $\sigma_{xx} = \sigma_1 + \sigma_3$ or $\sigma_{xx} = \sigma_1 + \sigma_M$. Here, σ_1 is the conductivity caused by free holes. The choice depends on whether the hopping conduction of type (1) or type (2) is dominant. Then, the high- and low-temperature portions of the $\sigma_{xx}(T)$ dependence were mutually extrapolated, and the parameters of the relevant activation laws were matched. It was considered that, for the region of mixed conductivity, the $\sigma_1(T)$ dependence has an activation character with a constant activation energy. The results of fitting are shown in Fig. 3a (solid lines). It can be seen that this method of fitting is quite acceptable. Specifically, since the ϵ_1 conductivity is negligible below 7–10 K, the parameters of hopping conductivity were rather reliably determined by this method. In this case, the σ_1 summand can be separated successfully by subtracting the hopping component from the total conductivity σ_{xx} . As indicated above, the contribution of the hopping charge transfer to the σ_{xy} component was negligibly small.

The effect of light holes was taken into account as follows. It is well known that the presence of mobile light holes causes an additional field dependence of the Hall coefficient in $p\text{-Hg}_{0.8}\text{Cd}_{0.2}\text{Te}$ crystals. Specifically, the ratio $R_H(B)/R_H(\infty)$ at 77 K decreases from 1.35 ± 0.05 to 1 when B increases from 0 to 3 T [9]. The effective mass of light holes varies only slightly below 77 K. At the same time, the relaxation time of light holes is nearly independent on their mass because they transform into heavy holes due to scattering [15]. Therefore, it was assumed that the contribution of light holes to the Hall effect at $T < 77$ K is independent of T . Let us use the definition of the σ_{xx} and σ_{xy} quantities and neglect the contribution of light holes to the σ_1 quantity. In this case, the Hall mobility and the density of heavy holes are equal to

$$\mu_{hH} \equiv r_H^{(hh)} \mu_h = \frac{\sigma_{xy}}{1.35 B \sigma_1}, \quad p = \frac{1.35 r_H^{(hh)} \sigma_1^2}{e R_H \sigma_{xx}}. \quad (3)$$

It is noteworthy that the effect of hopping conduction leads to a substantial decrease in the effective Hall mobility $R_H \sigma$. Thus, at the lowest temperatures in the investigated range, the mobility derived from formula (3) exceeds the $R_H \sigma$ quantity by more than an order of magnitude. It is probable that this is precisely the main cause of the low hole mobility found in [1–3], where no allowance was made for the effects of the hopping conduction.

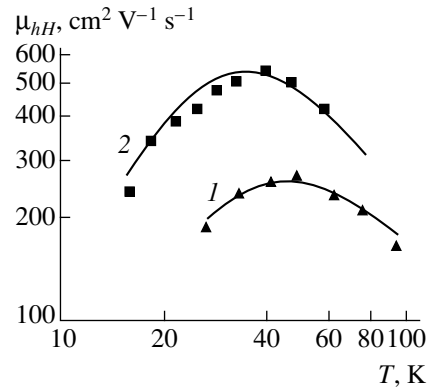


Fig. 4. Temperature dependence of mobility of heavy holes in Cu-doped and In-compensated $p\text{-Hg}_{0.8}\text{Cd}_{0.2}\text{Te}$ crystals. Squares and triangles correspond to the results of measurement; lines represent the results of calculations. (1) $N_A = 1.14 \times 10^{17} \text{ cm}^{-3}$, $N_D = 9.2 \times 10^{16} \text{ cm}^{-3}$; (2) $N_A = 2.6 \times 10^{16} \text{ cm}^{-3}$, $N_D = 2.2 \times 10^{16} \text{ cm}^{-3}$.

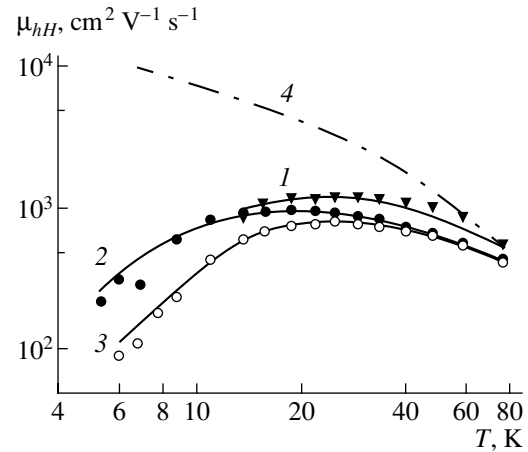


Fig. 5. Temperature dependence of mobility of heavy holes in uncompensated $p\text{-Hg}_{0.8}\text{Cd}_{0.2}\text{Te}:\text{Cu}$ crystals. Circles and triangles correspond to results of measurement; lines represent the results of calculations. (1) $N_{\text{Cu}} = 1.5 \times 10^{15} \text{ cm}^{-3}$, $N_D = 4 \times 10^{15} \text{ cm}^{-3}$, $[V_{\text{Hg}}] < 10^{14} \text{ cm}^{-3}$; (2) $N_{\text{Cu}} = 3.5 \times 10^{16} \text{ cm}^{-3}$, $N_D = 4 \times 10^{15} \text{ cm}^{-3}$, $[V_{\text{Hg}}] < 10^{14} \text{ cm}^{-3}$; (3) $N_{\text{Cu}} = 3.5 \times 10^{16} \text{ cm}^{-3}$, $N_D = 4 \times 10^{15} \text{ cm}^{-3}$, $[V_{\text{Hg}}] = 1.8 \times 10^{16} \text{ cm}^{-3}$; (4) $N_A = N_D = 0$.

Summary results of the measurements of μ_{hH} are shown in Figs. 4 and 5. It can be seen that the low-temperature hole mobility in the compensated crystals is relatively low and decreases with an increase in the doping level. In contrast to this, in the slightly compensated crystals at $T < 20$ K, the mobility is virtually independent of the Cu concentration. It should be noted that, in the presence of Hg vacancies, the holes are scattered noticeably more strongly in such crystals,

although the intrinsic acceptors exert no effect on the density of free holes in p -Hg_{0.8}Cd_{0.2}Te:Cu crystals below 30 K (see curves 1, 2 in Fig. 3a).

3. MODEL

The mobility of free holes was calculated by numerical integration in the context of the long-wavelength approximation of the general theory of scattering (see, for example, [4, 16]). Computational formulas were written for the case of an arbitrary isotropic dispersion law, since the nonparabolicity of the heavy-hole band is quite noticeable even at low energies [9]. The degree of degeneracy of electrons and holes was assumed to be arbitrary.

Two approximations were considered for the overlapping integral $I_h(\mathbf{k}', \mathbf{k})$. It was assumed that, in one case, $I_h(\mathbf{k}', \mathbf{k}) = 1$ and, in the other case, according to [4],

$$|I_h(\mathbf{k}', \mathbf{k})|^2 = \frac{1 + 3 \cos^2 \theta_{\mathbf{k}}}{4} \equiv 1 - \frac{3}{4} \sin^2 \theta_{\mathbf{k}}. \quad (4)$$

The hole scattering by polarization optical vibrations (*pol*), acoustic phonons (*ac*), charged centers (*I*), and composition fluctuations (*fl*), as well as hole-hole scattering were taken into account. According to estimations, the effect of other types of scattering is small. The matrix elements of the interaction Hamiltonian for the first three mechanisms were written according to [4, 17]:

$$\begin{aligned} & |\langle \mathbf{k} \pm \mathbf{q} | H_{pol} | \mathbf{k} \rangle|^2 \\ &= \frac{2\pi e^2 \hbar \omega_{LO} q^2 (n_{\mathbf{q}} + 1/2 \mp 1/2)}{V \varepsilon_p (q^2 + r_0^{-2})^2} |I_h(\mathbf{k} \pm \mathbf{q}, \mathbf{k})|^2, \end{aligned} \quad (5)$$

$$|\langle \mathbf{k} \pm \mathbf{q} | H_{ac} | \mathbf{k} \rangle|^2 = \frac{\Xi_{\Gamma}^2 k_B T}{2VC_{11}} |I_h(\mathbf{k} \pm \mathbf{q}, \mathbf{k})|^2, \quad (6)$$

$$\begin{aligned} & |\langle \mathbf{k} \pm \mathbf{q} | H_I | \mathbf{k} \rangle|^2 \\ &= \frac{16\pi^2 e^4 N_I}{V \varepsilon_S^2 (q^2 + r_0^{-2})^2} |I_h(\mathbf{k} \pm \mathbf{q}, \mathbf{k})|^2. \end{aligned} \quad (7)$$

Here, r_0 is the screening radius; $n_{\mathbf{q}}$ is the distribution function for LO phonons; $\varepsilon_p = \varepsilon_S \varepsilon_{\infty} / (\varepsilon_S - \varepsilon_{\infty})$, where ε_S and ε_{∞} are the static and high-frequency permittivities, respectively; $N_I = \sum V_v N_v$, where Z_v and N_v are the charge multiplicity and the concentration of charged centers of the v th type, respectively; Ξ_{Γ} is the deformation potential; and C_{ik} is the tensor of the elasticity moduli.

The contribution of the scattering by composition fluctuations was evaluated in the context of the theory developed in [18]. In the case of an ideal solution and arbitrary x , the relevant term can be written as

$$|\langle \mathbf{k} \pm \mathbf{q} | H_{fl} | \mathbf{k} \rangle|^2 = \frac{x(1-x)}{N_0 V} \left(\frac{\partial E_V}{\partial x} \right)^2 |I_h(\mathbf{k} \pm \mathbf{q}, \mathbf{k})|^2, \quad (8)$$

where N_0 is the atomic concentration in the metal sublattice.

The scattering by acoustical phonons, charged centers, composition fluctuations, and polarization vibrations was taken into account in the relaxation-time approximation. In the latter case, this approximation is quite acceptable when $T < 80$ K, since in this temperature range $\exp(-\hbar \omega_{LO} / k_B T) < 0.1$, where ω_{LO} is the frequency of long-wavelength LO phonons. The relevant formulas for the inverse relaxation time in the case of an arbitrary isotropic dispersion law can be written as

$$\frac{1}{\tau_{fl}(\varepsilon)} = \frac{\pi x(1-x)}{\hbar N_0} \left(\frac{\partial E_V}{\partial x} \right)^2 N_{hh}(\varepsilon) L_{fl}, \quad (9)$$

$$\frac{1}{\tau_{ac}(\varepsilon)} = \frac{\pi \Xi_{\Gamma}^2 k_B T}{\hbar C_{11}} N_{hh}(\varepsilon) L_{ac}, \quad (10)$$

$$\begin{aligned} \frac{1}{\tau_{pol}(\varepsilon)} &= \frac{\pi^2 e^2 \omega_{LO}}{\varepsilon_p} N_{hh}(\varepsilon + \hbar \omega_{LO}) L_{pol} \exp(-\hbar \omega_{LO} / k_B T) \\ &\times \{ (1 + [\exp(\hbar \omega_{LO} / k_B T) - 1]) f_0(\varepsilon + \hbar \omega_{LO}) \}, \end{aligned} \quad (11)$$

$$\frac{1}{\tau_I(\varepsilon)} = \frac{2\pi^3 \hbar^3 Z^2 N_I e^4 N_{hh}(\varepsilon)}{\varepsilon_S^2 p_{hh}^4(\varepsilon)} L_I. \quad (12)$$

Here, L_{fl} , L_{ac} , L_{pol} , and L_I are multipliers, whose form depends on the form of the overlap integral $I_h(\mathbf{k}', \mathbf{k})$; and $f_0(\varepsilon)$ is the equilibrium distribution function of holes.

If $I_h(\mathbf{k}', \mathbf{k}) = 1$, the multipliers corresponding to the scattering by acoustical phonons, by polar optical phonons, and by charged centers can be written, respectively, as

$$L_{fl} = L_{ac} = 1, \quad (13)$$

$$L_{pol} = \frac{1}{2kk'} \ln \frac{z_k + 2kk'}{z_k - 2kk'} - \frac{2r_0^{-2}}{z_k^2 - 4k^2 k'^2}, \quad (14)$$

$$L_I = \ln(1+b) - b/(1+b), \quad (15)$$

where $z_k = k^2 + k'^2 + r_0^{-2}$; $k = p_{hh}(\epsilon)/\hbar$; $k' = p_{hh}(\epsilon + \hbar\omega_{LO})/\hbar$; and $b = 4r_0^2 k^2$.

Let us assume that $I_h^2(\mathbf{k}', \mathbf{k}) = (1 + 3\cos^2\theta_{\mathbf{k}})/4$. In this case,

$$L_{fl} = L_{ac} = 1/2, \quad (16)$$

$$L_{pol} = \frac{1}{8kk'} \left[1 + \frac{3z_k}{4k^2k'^2} (z_k + 2r_0^{-2}) \right] \ln \frac{z_k + 2kk'}{z_k - 2kk'} - \frac{3}{8k^2k'^2} - \frac{1}{2r_0^2} \frac{1 + 3z_k/(2kk')^2}{z_k^2 - 4k^2k'^2}, \quad (17)$$

$$L_I = \left(1 + \frac{3}{b} \right)^2 \ln(1 + b) - \frac{5b^2 + 21b + 18}{2b(1 + b)}. \quad (18)$$

The hole-hole scattering that cannot be described in terms of the relaxation time [15, 16] was taken into account using the variational method (see monograph [16]). According to [16], in the case of the simultaneous effect of the above-mentioned scattering mechanisms, the average drift mobility of nondegenerate holes in the second-order approximation is equal to

$$\mu_h \approx \frac{3\pi}{32} \mu_0 \left\{ 1 + \frac{[\mu_0/\mu_1 - 5/2]^2}{\sqrt{2} p \mu_0 / (N_I \mu_I) + 2\mu_0/\mu_2 - (\mu_0/\mu_1)^2} \right\}, \quad (19)$$

where

$$\frac{1}{\mu_0} = \frac{1}{\mu_I} + \frac{1}{3\mu_{fl}} + \frac{1}{3\mu_{ac}} + \frac{3\pi}{32\mu_{pol}},$$

$$\frac{1}{\mu_1} = \frac{1}{\mu_I} + \frac{1}{\mu_{fl}} + \frac{1}{\mu_{ac}} + \frac{15\pi}{64\mu_{pol}},$$

$$\frac{1}{\mu_2} = \frac{1}{\mu_I} + \frac{2}{\mu_{fl}} + \frac{2}{\mu_{ac}} + \frac{105\pi}{128\mu_{pol}}.$$

The partial mobility of heavy holes μ_β (β is for I , ac , pol , or fl) can be written as

$$\mu_\beta = \frac{\int_0^\infty d\epsilon p_{hh}^3(\epsilon) f_0'(\epsilon) \tau_\beta(\epsilon) / m_{hh}(\epsilon)}{\int_0^\infty d\epsilon p_{hh}^3(\epsilon) f_0'(\epsilon)}, \quad (20)$$

where $p_{hh}(\epsilon)$ represents the inverse dispersion law for heavy holes, and $m_{hh}(\epsilon) = 0.5 p_{hh}^2 / \partial \epsilon$ is the effective mass.

The Hall factor for heavy holes in the absence of hole-hole scattering was calculated from the formula

$$r_H^{(hh)} = \frac{\int_0^\infty d\epsilon p_{hh}^2(\epsilon) f_0'(\epsilon) [\tau(\epsilon) / m_{hh}(\epsilon)]^2}{\left[\int_0^\infty d\epsilon p_{hh}^3(\epsilon) f_0'(\epsilon) \tau(\epsilon) / m_{hh}(\epsilon) \right]^2} \times \int_0^\infty d\epsilon p_{hh}^3(\epsilon) f_0'(\epsilon), \quad (21)$$

which can be obtained easily by generalizing the known definition [19] to the case of the nonparabolic dispersion law. Here, $\tau = 1 / \sum \tau_\beta^{-1}$.

4. RESULTS OF CALCULATIONS AND DISCUSSION

The results of calculating the electron mobility μ_e at 4.2 K for n -type crystals for the case of scattering by impurity ions are shown in Fig. 1. The calculations were carried out using formulas (12), (15), and (20), in which the dispersion law and the density of states for heavy holes were replaced by relevant characteristics of the conduction band, taken from [9]. It was assumed that $I_e(\mathbf{k}', \mathbf{k}) = 1$. According to [15, 16], no allowance was made for electron-electron scattering, since the electrons were degenerate under these conditions.

It can be seen that the measured and calculated data coincide in the region of high electron densities. In the region $n < 10^{15} \text{ cm}^{-3}$, a noticeable variance of mobility is observed due to variation in the impurity composition of the sample. However, all experimental points lie between the curves calculated for $N_A = 5 \times 10^{14}$ and $1.5 \times 10^{15} \text{ cm}^{-3}$. Thus, all crystals investigated in this study contained about $(1 \pm 0.5) \times 10^{15} \text{ cm}^{-3}$ background donors on average.

The results of calculating the hole mobility at 77 K, which were performed assuming that $I_h(\mathbf{k}', \mathbf{k}) = 1$, are shown in Fig. 2 (curves 1–5). The calculations were carried out without fitting, and the numerical values of the model parameters were taken from independent reports. Specifically, it was assumed that $\epsilon_S = 20.5 - 15.6x + 5.7x^2$ and $\epsilon_\infty = 15.2 - 15.6x + 8.2x^2$ [20], $|\partial E_V / \partial x| = 0.35 \text{ eV}$ [21], and $C_{11} = 5.35 \times 10^{11} \text{ erg/cm}^3$ [22]. For the acoustic potential Ξ_F , we used the value derived from the data on the spectra of absorption by free holes (see [11]). With allowance made for the correction to the hole scattering by composition fluctuations, $\Xi_F = 10.5 \text{ eV}$. It was assumed that the concentration of background donors $N_D = 1 \times 10^{15} \text{ cm}^{-3}$ and $Z = 1$ for all charged centers. The density of states and the

dispersion law for the heavy-hole band in $\text{Hg}_{1-x}\text{Cd}_x\text{Te}$ were taken in the form derived recently [23] from the results of precision measurements of the intrinsic-electron density as a function of temperature:

$$N_{hh}(\varepsilon) = \frac{\sqrt{2m_{hh}^3(0)}}{\pi^2\hbar^3} \sqrt{\varepsilon(1+\varepsilon/\varepsilon_0)}(1+2\varepsilon/\varepsilon_0), \quad (22)$$

$$p_{hh}(\varepsilon) = \sqrt{2m_{hh}(0)\varepsilon(1+\varepsilon/\varepsilon_0)}, \quad (23)$$

where $m_{hh}(0) = 0.39m_0$, and $\varepsilon_0 = 0.096$ eV.

As follows from Fig. 2, the results of calculations in this approximation nearly coincide with the averaged results of measurements. Alternatively, if one assumed that $I_h^2(\mathbf{k}', \mathbf{k}) = (1 + 3\cos^2\theta_{\mathbf{k}})/4$ [3, 4], the discrepancy between the results of calculations and the averaged experimental data becomes rather considerable (see Fig. 2, curve 6).

The result obtained in this study somewhat contradicts the conclusions made previously in [24], where the hole mobility in $p\text{-Hg}_{0.8}\text{Cd}_{0.2}\text{Te} : \text{Cu}$ at 77 K was also investigated. However, hole-hole scattering was not observed in [24]. This discrepancy is explained by the fact that the degenerate crystals with $p > 10^{18} \text{ cm}^{-3}$ were investigated in [24]. In degenerate crystals, scattering of this type should not manifest itself [15].

It is worth noting that the $r_H^{(hh)}$ values calculated using formula (21) for moderately doped $p\text{-Hg}_{0.8}\text{Cd}_{0.2}\text{Te}$ crystals vary in a narrow range from 1.03 to 1.1. This is in rather good agreement with the experimental data reported in [9], according to which $r_H^{(hh)} \approx 1.02$. This agreement is attributed to the fact that, in the region $\varepsilon \approx k_B T$, the relaxation time of the hole momentum is almost independent of the hole energy due to the simultaneous effect of five different tantamount mechanisms of scattering.

The results of calculations of the heavy-hole mobility $\mu_{hH} = r_H^{(hh)} \mu_h$ in the temperature range of 15–100 K for the Cu-doped and In-compensated $p\text{-Hg}_{0.79}\text{Cd}_{0.21}\text{Te}$ crystals are shown in Fig. 4. The calculations were performed using relationships (4)–(14) and (19)–(23). In the case under consideration, the dopant concentration was rather high, whereas the Fermi level was located above the isolated-acceptor level. Due to this, the electroneutrality condition can be written as $p = N_{\text{Cu}}^- - N_{\text{In}}^-$. It follows from this condition that $N_I = p + 2N_{\text{In}}^-$. It can be seen (Fig. 4) that the values of hole mobilities calculated for such crystals coincide with the relevant experimental values in the entire temperature range under investigation. It should be noted that the hole-hole scattering is weak in nearly completely compensated crys-

tals [16]. In this case, the Hall factor can be calculated from formula (21) quite accurately.

In slightly compensated crystals and at low temperatures, the Fermi level is located approximately at the middle of the gap between the valence band and the isolated-acceptor level. Under these conditions, it is necessary to make allowance for the capability of acceptors to attach holes to form positively charged centers (A^+ centers) [25]. The population of the A^+ states of singly charged acceptors is determined by the Gibbs distribution

$$f_{A1}^+(F) = \frac{6 \exp\left(\frac{\Delta E_1 - F}{k_B T}\right)}{4 + \exp\left(\frac{F - E_{A1}}{k_B T}\right) + 6 \exp\left(\frac{\Delta E_1 - F}{k_B T}\right)}. \quad (24)$$

Here, ΔE_1 is the attachment energy for an excess hole, E_{A1} is the ionization energy of an acceptor, and the Fermi energy F is reckoned from the valence-band top E_v . It was demonstrated in [26] that, for $\text{Hg}_{0.8}\text{Cd}_{0.2}\text{Te}$ crystals, $E_{A1} \approx 8$ meV, whereas the ΔE_1 energy amounts to about 10% of E_{A1} . Since a single acceptor in the A^+ state binds two holes, whereas the single-particle states are fourfold degenerate [18], the A^+ state was considered as sixfold degenerate.

It follows from expression (24) that, at moderately low temperatures and moderate levels of doping, the number of A^+ centers in slightly compensated crystals is comparable with the number of A^- centers and the number of donors. Because of this, an A^+ center should noticeably affect both the hole statistics and hole scattering. In this context, the electroneutrality condition for slightly compensated crystals was written as $N_A^- = p + N_D + N_{\text{Cu}} f_{A1}^+(F)$. Taking into account that the charge of each charged center is $\pm e$, the effective concentration of scattering centers equals $N_I = p + [N_{\text{Cu}} f_{A1}^+(F) + N_D]$.

Figure 5 (curves 1, 2) demonstrates the results of calculations of the Hall mobility μ_{hH} for heavy holes; formulas (4)–(14) and (19)–(22) were used. The Hall factor $r_H^{(hh)}$ at $T > 15$ K was calculated from formula (23). Under these conditions, the magnitude of this factor ranged from 1.05 to 1.15. Below 15 K, the Born approximation is not fulfilled for heavy holes [15]. Because of this, I used the value of $r_H^{(hh)} \approx 1.1$ calculated by the method of partial waves (see [15]). It can be seen that the calculated dependence $\mu_{hH}(T)$ is in rather good agreement with the results of measurements if we assume that $N_D = 4 \times 10^{15} \text{ cm}^{-3}$. The results of calculations of the hole mobility in the absence of donors and acceptors are also shown in Fig. 5 for com-

parison (curve 4). It can be seen that the scattering by charged centers becomes dominant below 30–40 K. Among other scattering mechanisms, the scattering by composition fluctuations is dominant in these conditions.

The estimated value obtained for N_D is independent of the Cu concentration. However, this value is several times larger than that determined above from the measurements of the electron mobility. Apparently, the cause of this discrepancy is that, along with shallow-level donors, deep-level donors and hole-trapping centers exist in the investigated $\text{Hg}_{0.8}\text{Cd}_{0.2}\text{Te}$ crystals. Such centers are observed in the measurements of the electron and hole lifetimes in p -type crystals (see, for example, [27, 28]). These centers are neutral in

$n\text{-Hg}_{0.8}\text{Cd}_{0.2}\text{Te}$, where the Fermi level lies close to the conduction band, but are activated in p -type crystals.

The existence of A^+ centers well explains the low hole mobility in the $p\text{-Hg}_{0.8}\text{Cd}_{0.2}\text{Te}:\text{Cu}$ crystals that contain Hg vacancies. These intrinsic defects are doubly charged acceptors. Because of this, their ionization energy is noticeably higher than that of Cu atoms. The energies of various levels of V_{Hg} were calculated in [26]. According to [26], a vacancy forms two acceptor levels with the energies $E_{A2}^{(1)} \approx 16$ meV and $E_{A2}^{(2)} \approx 32$ meV as well as the A^+ level with the energy $\Delta E_2 \approx 3.7$ meV. Therefore, the Gibbs distribution of V_{Hg} takes the following form:

$$f_{A2}^+(F) = \frac{4 \exp\left(\frac{\Delta E_2 - F}{k_B T}\right)}{6 + 4 \exp\left(\frac{F - E_{A1}^{(1)}}{k_B T}\right) + \exp\left(\frac{2F - E_{A1}^{(1)} - E_{A2}^{(2)}}{k_B T}\right) + 4 \exp\left(\frac{\Delta E_1 - F}{k_B T}\right)}. \quad (25)$$

It is easy to verify that the position of the A^+ levels of vacancies in the band gap of Cu-doped crystals is close to the Fermi level at low temperatures. Therefore, the probability of their occupation is high. Figure 5 (curve 3) shows the results of calculations of the hole mobility in the uncompensated crystal that contained $3.5 \times 10^{16} \text{ cm}^{-3}$ Cu atoms and 1.8×10^{16} Hg vacancies.

In this case, $N_I = p + 2\{[V_{\text{Hg}}]f_{A2}^+(F) + N_{\text{Cu}}f_{A1}^+(F) + N_D\}$, where $[V_{\text{Hg}}]$ is the vacancy concentration. It can be seen that the results of calculations performed using relationships (4)–(14) and (19)–(25) are quite consistent with the experimental data if additional scattering by positively charged vacancies is allowed for.

5. CONCLUSIONS

(i) The low Hall mobility in $p\text{-Hg}_{0.8}\text{Cd}_{0.2}\text{Te}$ crystals at low temperatures is a consequence of the influence of the hopping charge transport on the diagonal component of the electrical-conductivity tensor.

(ii) The mobility of heavy holes in $p\text{-Hg}_{0.8}\text{Cd}_{0.2}\text{Te}$ crystals at $T < 20$ K is limited by the scattering at charged centers. Among these centers, in the case of uncompensated crystals, the positively charged acceptors and deep-level donors play an important role. The other scattering mechanisms exert virtually no effect on the μ_{hH} quantity.

(iii) The mobility of heavy holes in $p\text{-Hg}_{0.8}\text{Cd}_{0.2}\text{Te}$ crystals at higher temperatures is limited by the hole–hole scattering as well as by the hole scattering at composition fluctuations, at lattice vibrations, and at charged centers.

(iv) The overlap integral of the Bloch functions for electrons and holes in the $\text{Hg}_{0.8}\text{Cd}_{0.2}\text{Te}$ crystals is equal to unity.

REFERENCES

1. M. A. Berding, S. Krishnamurthy, A. Sher, and A.-B. Chen, *J. Vac. Sci. Technol. A* **5** (5), 3014 (1987).
2. J. R. Mayer, F. J. Bartoli, and C. A. Hoffman, *J. Vac. Sci. Technol. A* **5** (5), 3035 (1987).
3. I. M. Tsidil'kovskii, G. I. Kharus, and N. G. Shelushinina, *Impurity States and Transport Phenomena in Zero-Gap Semiconductors* (Ural. Nauchn. Tsentr Akad. Nauk SSSR, Sverdlovsk, 1987).
4. B. Ridley, *Quantum Processes in Semiconductors* (Clarendon, Oxford, 1982; Mir, Moscow, 1986).
5. V. V. Bogoboyashchii, A. I. Elizarov, V. A. Petryakov, *et al.*, *Fiz. Tekh. Poluprovodn. (Leningrad)* **21**, 1469 (1987) [*Sov. Phys. Semicond.* **21**, 893 (1987)].
6. V. A. Bazakutsa, V. I. Belozertseva, V. V. Bogoboyashchii, *et al.*, in *Impurities and Defects in Narrow-Gap Semiconductors* (Pavlodar, 1987), p. 148.
7. N. N. Berchenko, V. V. Bogoboyashchii, A. I. Elizarov, *et al.*, in *Impurities and Defects in Narrow-Gap Semiconductors* (Pavlodar, 1987), p. 129.
8. V. V. Bogoboyashchyy, *Semicond. Phys., Quantum Optoelectron.* **2** (1), 62 (1999).
9. V. V. Bogoboyashchii, *Proc. SPIE* **3486**, 325 (1997).
10. A. I. Elizarov, *Zavod. Lab.*, No. 10, 82 (1981).
11. C. T. Elliot, I. Melngailis, and T. C. Harman, *J. Phys. Chem. Solids* **33** (2), 1527 (1972).
12. N. F. Mott, *J. Non-Cryst. Solids* **1** (1), 1 (1968).

13. A. V. Vedyayev and A. B. Granovskii, *Fiz. Tverd. Tela (Leningrad)* **28** (8), 2310 (1986) [*Sov. Phys. Solid State* **28**, 1293 (1986)].
14. H. Böttger and V. V. Bryksin, *Phys. Status Solidi B* **113** (1), 9 (1982).
15. F. J. Blatt, *Solid State Phys.* **4**, 1999 (1957).
16. I. M. Dykman and P. M. Tomchuk, *Transport Phenomena and Fluctuations in Semiconductors* (Naukova Dumka, Kiev, 1981).
17. O. Madelung, *Introduction to Solid-State Theory* (Springer-Verlag, Berlin, 1978; Nauka, Moscow, 1980).
18. I. S. Shlimak, A. L. Éfros, and I. Ya. Yanchev, *Fiz. Tekh. Poluprovodn. (Leningrad)* **11** (2), 257 (1977) [*Sov. Phys. Semicond.* **11**, 149 (1977)].
19. V. L. Bonch-Bruevich and S. G. Kalashnikov, *Physics of Semiconductors* (Nauka, Moscow, 1990).
20. A. V. Lyubchenko, E. F. Sal'kov, and F. F. Sizov, *Physical Foundations of Semiconductor Infrared Photoelectronics* (Naukova Dumka, Kiev, 1984).
21. L. S. Kim, S. Perkowicz, O. K. Wu, and J. N. Schulman, *Semicond. Sci. Technol.* **5** (3S), S107 (1990).
22. Yu. Kh. Vekilov and A. P. Rusakov, *Fiz. Tverd. Tela (Leningrad)* **13** (4), 1157 (1971) [*Sov. Phys. Solid State* **13**, 956 (1971)].
23. V. V. Bogoboyashchyy, *Semicond. Phys., Quantum Optoelectron.* **4** (4), 442 (2001).
24. H. R. Vydyanath, *J. Electrochem. Soc.* **128** (12), 2609 (1981).
25. B. I. Shklovskii and A. L. Efros, *Electronic Properties of Doped Semiconductors* (Nauka, Moscow, 1979; Springer-Verlag, New York, 1984).
26. V. V. Bogoboyashchii, *Fiz. Tekh. Poluprovodn. (St. Petersburg)* **36** (1), 29 (2002) [*Semiconductors* **36**, 26 (2002)].
27. D. L. Polla and C. E. Jones, *J. Appl. Phys.* **52** (8), 5118 (1981).
28. D. L. Polla, M. B. Reine, and C. E. J. Jones, *J. Appl. Phys.* **52** (8), 5132 (1981).

Translated by N. Korovin

ELECTRONIC
AND OPTICAL PROPERTIES
OF SEMICONDUCTORS

A DLTS Study of Deep Levels in the Band Gap of Textured Stoichiometric *p*-CdTe Polycrystals

E. A. Bobrova*, Yu. V. Klevkov, S. A. Medvedev, and A. F. Plotnikov

Lebedev Physical Institute, Russian Academy of Sciences, Leninskiĭ pr. 53, Moscow, 117924 Russia

*e-mail: bobrova@mail1.lebedev.ru

Submitted February 27, 2002; accepted for publication April 25, 2002

Abstract—Deep-level transient spectroscopy (DLTS) was used to identify a set of deep electronic states in the band gap of textured *p*-CdTe polycrystals whose composition was almost stoichiometric. Four hole traps and two electron traps were observed. It is shown that the deepest hole trap with a level at $E_v + 0.86$ eV corresponds to a prevalent defect in this material. Special features of the line shape in the DLTS spectrum and the logarithmic dependence of population of this level on the duration of the filling pulse correspond to an extended defect related most probably to dislocations at the grain boundaries. © 2002 MAIK “Nauka/Interperiodica”.

1. INTRODUCTION

Control of the magnitude and type of electrical conductivity in growing CdTe crystals still remains a complicated problem. Depending on the degree of deviation from stoichiometry, on the concentration of uncontrolled impurities, and on the structural quality of the crystals, the resistivity may vary from 10^3 to 10^8 Ω cm. Irrespective of the methods for growing nominally undoped *p*-CdTe single crystals, a set of deep electronic states exists, as a rule, in the band gap of this compound; these states exert a pronounced effect on the resistivity. At present, the resistivity of undoped CdTe can be rendered as high as 10^{10} – 10^{11} Ω cm [1]. Since it is difficult to explain these experimental data on the basis of existing models of compensation, more and more attention is being given to the influence of structural defects (dislocations, grain boundaries, and such) on the optical and (especially) transport properties of CdTe. This is related to the fact that extended defects are electrically active, are involved in scattering the free charge carriers, represent the sites of build-up (i.e., sinks) of the point defects (both intrinsic and extrinsic) during crystal growth, and give rise to fields of elastic strains and internal electric fields; the latter induce a potential relief in the bulk of the crystals.

Deformation of samples is typically used in order to determine the role of extended defects in the formation of deep electronic states when these defects interact with point defects. Apparently, the use of this method is related to the fact that the background impurities in unstrained crystals obscure the extended growth defects and give rise to certain difficulties when interpreting the spectra of deep electronic states. In addition, the concentration of background impurities in nominally undoped crystals grown from the liquid phase at high temperatures is typically no lower than 10^{16} – 10^{17} cm^{-3} .

Deep-level transient spectroscopy (DLTS) is a widely used method for investigating deep band-gap states in semiconductors. However, it is quite difficult to ascertain the type and origin of these states using DLTS. The reason is that extended defects, which are typically present in actual crystals, can interact with impurities and form associations with a complex structure (closely associated pairs). As a result of such interaction, a number of deep electronic states are observed in the band gap even if the concentrations of uncontrolled impurities are low; an unconventional line shape in the DLTS spectrum and the logarithmic law for the capture of nonequilibrium charge carriers are characteristic of these states [2, 3].

The objective of this study was to identify a set of deep band-gap electronic states which are characteristic of *p*-CdTe polycrystals that are textured along the [111] direction and have an almost stoichiometric composition; we also attempted to elucidate the involvement of extended growth defects (dislocations, grain boundaries) in the formation of deep electronic states using DLTS.

2. EXPERIMENTAL

2.1. Preparation of the Samples

The polycrystals were obtained by free growth in dynamic vacuum at a temperature of 620°C; a purified CdTe charge was used. The average diameter of a grain in the texture was 1.5–2 mm. Misorientation of the grains in reference to the [111] direction was no larger than 3°–7°. The dislocation density in a single-crystal grain in the (111) plane was measured using the etch-pit method and was found to be no higher than 10^3 cm^{-2} . According to mass spectrometric analysis, the concentration of the main background impurities did not

exceed 10^{15} cm^{-3} . The charge-carrier concentration measured along the [111] direction at room temperature was equal to $(1-3) \times 10^{13} \text{ cm}^{-3}$, and the hole mobility was no lower than $80 \text{ cm}^2 \text{ V}^{-1} \text{ s}^{-1}$.

Samples with an area of $10 \times 10 \text{ mm}^2$ and a thickness of 2 mm were cut from polycrystalline ingots perpendicularly to the growth direction. After grinding and thorough polishing, the samples were treated in a bromine-ethanol etchant. The nonrectifying contact was formed by depositing Au from an AuCl_3 solution, whereas the Schottky barrier contact was obtained by plating the sample surface with In. The area of the barrier contact was 7.5 mm^2 .

In order to assess the quality of CdTe and the contacts and to interpret the DLTS spectra, we measured the current-voltage (I - V) and capacitance-voltage (C - V) characteristics in the temperature range from 80 to 380 K.

2.2. The Results of the I - V and C - V Measurements

The I - V characteristics of the structures with a Schottky barrier were measured at various temperatures. The Schottky barrier resistance (R) determined from the reverse portion of I - V characteristics varied from 200 k Ω at 380 K to 2 M Ω and higher at $T \leq 150$ K. The temperature dependence of current for low forward biases was not consistent with the theory based on thermal emission and diffusion, which gave no way of estimating the Schottky barrier height. In the temperature range of ~ 240 - 340 K, a portion with a rapid increase in current with a subsequent slower increase was observed at low forward-bias voltages (< 0.5 V); it is conceivable that this phenomenon is related to the existence of internal potential barriers at dislocations or grain boundaries. In addition, the I - V characteristics can be affected by the presence of a thin oxide, tunneling, and by such processes as recombination and capture by traps and freezing-out of the charge carriers. The series resistance (r) of the structure at a given reverse bias was determined from ac bridge-circuit measurements at a

frequency coinciding with that of DLTS measurements. A substantial increase in r (from ~ 700 to 6000 Ω) and a simultaneous decrease in the capacitance C (from ~ 50 to 25 pF at a bias of $V_b = 6$ V) were observed as the temperature was lowered from 150 to 110 K.

The dependences of $1/C^2$ on the reverse-bias voltage V were nonlinear at all temperatures (Fig. 1), which could be related to the formation of an inversion layer near the surface if there was a thin (penetrable by tunneling) oxide beneath the Schottky contact [4] and/or to the effect of the surface states [5]. As will be shown in what follows, our experimental data are consistent with the presence of an inversion layer in the vicinity of the surface. Determination of the Schottky barrier height from the dependence $1/C^2$ on V is difficult if there is a thin oxide layer because of the lack of important data on structure parameters such as the oxide-layer thickness, the density of surface states, and so on [4]. Variations in the C - V characteristics with temperature indicate that there is a tendency toward an increase in the barrier height; in addition, free charge carriers tend to freeze out as the temperature is lowered. The values of the free-carrier concentration determined from C - V characteristics in the case when there is a thin oxide layer are more accurate if the bias voltage is close to zero [4]. In particular, the room-temperature charge-carrier concentration determined from the C - V characteristic in the region of the zero bias voltage was found to be equal to $2 \times 10^{13} \text{ cm}^{-3}$, which is consistent with the results of Hall effect measurements. The charge-carrier concentration was equal to $4 \times 10^{13} \text{ cm}^{-3}$ at 370 K. An appreciable freezing-out of free charge carriers was observed at temperatures below 150 K. The carrier concentration calculated from the ac series resistance measured at room temperature is higher by a factor of 2-3 than the concentration determined from the C - V or dc Hall effect measurements. It is conceivable that this discrepancy is related to the effect of internal barriers in the polycrystal. At other temperatures, comparison is difficult since there is no data on the temperature dependence of mobility in polycrystals.

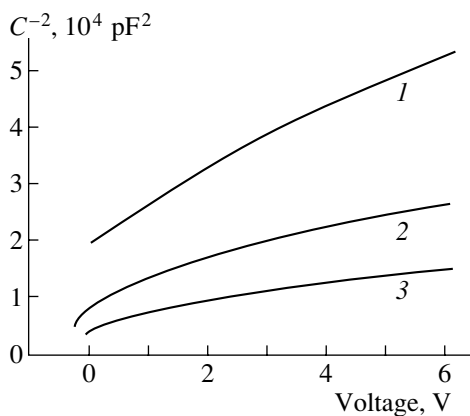


Fig. 1. Capacitance-voltage characteristics of a reverse-biased Schottky structure at temperatures of (1) 150, (2) 290, and (3) 370 K.

2.3. Measurements of the Deep-Level Spectra by DLTS

The spectra were recorded using an automated setup which incorporated a boxcar integrator; the data were stored in a computer. The setup made it possible to record the spectra for four emission-rate windows during a single temperature pass from 80 to 380 K. The relaxation times (τ) were measured in the range from 4 to 320 ms. The duration of a filling pulse (≥ 4 ms) was sufficient for attaining the highest occupancy of the deep levels.

Taking into account that the series resistance of a Schottky diode increases at low temperatures, we determined the temperature range where the DLTS measurements were feasible. It is well known that the series-connected capacitance and resistance of an actual structure are transformed into an equivalent parallel circuit

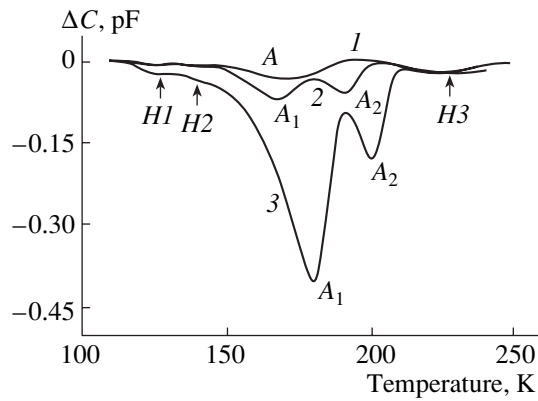


Fig. 2. DLTS spectra of a Schottky structure at a bias $V_b = +6$ V and the filling-pulse amplitudes $V_p = (1) -4$, $(2) -6.5$, and $(3) -7.5$ V. The delayed gate times were $t_1 = 4$ ms and $t_2 = 8$ ms.

if the capacitance is measured by the bridge-based method [6]. If the series resistance of the structure exceeds a certain value, the amplitude of the DLTS signal decreases and the measured capacitance becomes smaller than its true value. If the series resistance increases further, so that the condition

$$\omega rC < 1 + r/R \quad (1)$$

becomes invalid, the phase of the measured signal reverses. In condition (1), ω is the probing-signal frequency (in our experiments $\omega = 2\pi \times 840$ kHz); and R , r , and C are the structure parameters defined above.

As follows from the I - V characteristics, the ratio r/R can always be disregarded in expression (1). In order to reduce C in (1), we predominantly applied large biases to the structure during DLTS measurements. The value of ωrC varied from ~ 0.2 to 0.9 in the temperature range from 150 to 110 K; as a result, sensitivity of the measurements diminished. We also verified experimentally that the reversal of the signal phase did not occur at temperatures above 100 K under the chosen conditions of measurements.

Four peaks corresponding to the capture of the majority charge carriers (holes) (Figs. 2, 3) and two peaks corresponding to the capture of electrons (Fig. 4) were observed in the DLTS spectra. In the temperature range where the $H1$ and $H2$ peaks were detected, the sensitivity of the measuring bridge was about three times lower than that for peaks $H3$ and $H4$. The activation energies $E_t - E_v$ and $E_c - E_t$ and the capture cross sections σ for deep levels are listed in the table; the cross sections were determined on the assumption that they were independent of temperature. A field dependence of the most intense peaks was not observed.

The presence of peaks with positive polarity (Fig. 4) indicates that there is an inversion layer near the semiconductor surface beneath the Schottky contact. During

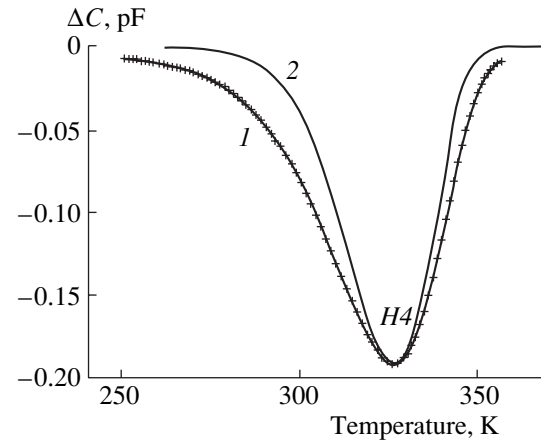


Fig. 3. DLTS spectra of a Schottky structure at a bias $V_b = +6$ V and the filling-pulse amplitude of $V_p = -1$ V (curve 1 represents the experimental data and curve 2 corresponds to the results of calculations). The delayed gate times were $t_1 = 320$ ms and $t_2 = 640$ ms.

the time the filling pulse is applied, injection of electrons from this layer into the p -type region of the structure is accompanied by their capture by deep electron traps.

The activation energies and the capture cross sections of the levels were determined either by plotting the Arrhenius law curve ($H3$), by adjusting the parameters of the calculated spectrum to fit its shape and position to the experimental spectrum ($H1$, $H2$, $E2$), or by using both methods ($E1$, $H4$). Variations in the bridge circuit sensitivity could be ignored in the temperature ranges that corresponded to the recording of separate peaks.

In addition to the aforementioned peaks, another peak (A) with anomalous properties was observed (Fig. 2); the

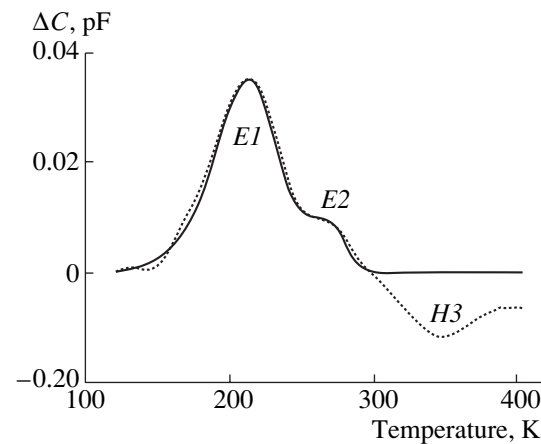


Fig. 4. DLTS spectra of a Schottky structure under the bias $V_b = +2$ V and the filling-pulse amplitude $V_p = -1$ V (the points are experimental and the solid line represents the results of calculations). The delayed gate times were $t_1 = 4$ ms and $t_2 = 8$ ms.

Parameters of deep levels

	$E_t - E_v$, eV	σ , cm ²		$E_c - E_t$, eV	σ , cm ²
<i>H1</i>	0.24 ± 0.02	2×10^{-14}	<i>E1</i>	0.17 ± 0.01	7×10^{-18}
<i>H2</i>	0.26 ± 0.02	1.5×10^{-14}	<i>E2</i>	0.34 ± 0.02	4×10^{-14}
<i>H3</i>	0.45 ± 0.01	3×10^{-14}			
<i>H4</i>	0.86 ± 0.03	2.4×10^{-13}			

position and height of this peak depended heavily on the conditions of measurements, primarily on the filling-pulse amplitude. As the latter increased, the peak shifted from ~ 140 to ~ 220 K, split into two peaks in a certain temperature range (peaks A_1 and A_2 in Figs. 2, 5), and increased markedly in height. For a pulse of forward bias exceeding the magnitude of reverse bias by several volts, the capacitance-relaxation amplitude was as high as approximately 20 pF, with the initial capacitance of the structure being approximately equal to 50 pF.

Such relaxation can be attributed to the existence of an inversion layer and the presence of a thin tunneling-penetrable oxide layer between the metal and semiconductor (it is well known that a detectable TeO_2 oxide at the CdTe surface is formed at room temperature when CdTe is exposed to air for a mere 2 h [7]). In addition, a potential barrier for the minority charge carriers is formed not only by oxide but also by the image forces [8]. As a result, the Schottky diode properties resemble those typical of metal–insulator–semiconductor structures for which large-amplitude capacitance relaxation is observed in the transition from the mode of profound depletion to the equilibrium state with the formation of an inversion layer. Furthermore, the relaxation curve usually has a complicated nonexponential shape; as a result, the recovery of the inversion layer in the case under consideration occurs with two time constants (peaks A_1 and A_2). As the filling-pulse amplitude

increases, these anomalous peaks completely obscure the peaks related to the electron capture. The observed shift of the peak A position along the temperature axis as the injecting-pulse amplitude increases is most probably related to the temperature-dependent tunneling of minority charge carriers from the metal into the semiconductor [9, 10], since the rate of bulk generation of charge carriers is very low at temperatures near 200 K.

The signal $\Delta C/C \approx 0.1$ was observed for peak $H4$ if the filling-pulse amplitude was equal to the applied reverse bias. Estimations of concentration N_T of centers $H4$ with allowance made for the probed depth showed that N_T is comparable with the majority-carrier concentration N . If the value of N_T/N is arbitrary and $\Delta C/C_0 \ll 1$ (when the amplitude of the filling pulse is low), the following expression can be used to estimate N_T :

$$N_T/N = 2(\Delta C/C_0)/[K - (2\Delta C/C_0)(1 - C_0/C_\lambda)]. \quad (2)$$

Here, $K = (1 - C_0/C_b)(1 + C_0/C_b - 2C_0/C_\lambda)$, C_0 is the capacitance when a reverse bias is applied to the structure, C_b is the capacitance at the instant of application of the filling-pulse, and C_λ is the capacitance of the layer from the point where the trap level intersects the Fermi level up to the electroneutrality region. It is also assumed in (2) that N_T and N are constant.

Estimations of concentrations of the $H4$ and $H3$ centers yield $2 \times 10^{13} \text{ cm}^{-3}$ in the probed-depth range of

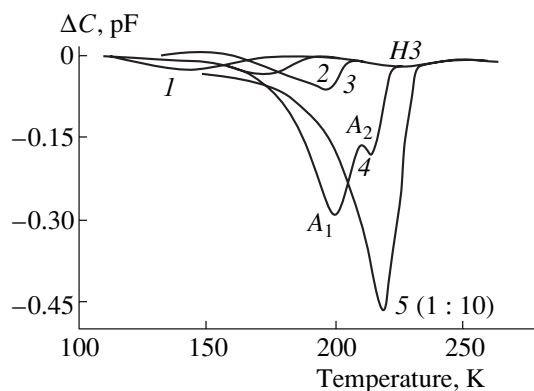


Fig. 5. DLTS spectra of a Schottky structure under a bias $V_b = +6$ V and the filling-pulse amplitudes $V_p = (1) -3$, (2) -4 , (3) -6 , and (4) -6.5 V; spectrum 5 corresponds to $V_b = +1$ V and $V_p = -5$ V. The delayed gate times were $t_1 = 4$ ms and $t_2 = 8$ ms.

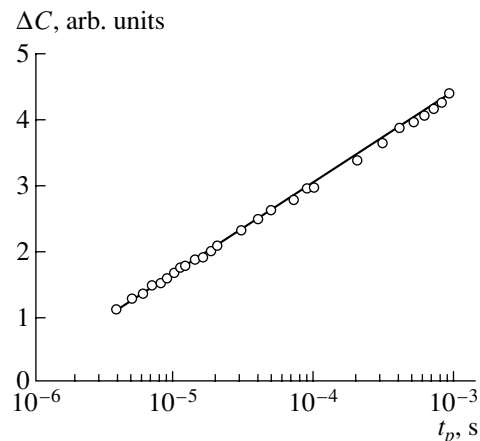


Fig. 6. The amplitude of the capacitance-relaxation signal as a function of the filling-pulse duration. The Schottky structure was biased with $V_b = +6$ V, and the filling-pulse amplitude was $V_p = -1$ V.

4.5–6.5 μm and $4 \times 10^{10} \text{ cm}^{-3}$ in the probed-depth range of 6–12 μm . These estimations are difficult for other centers because the estimates involve large errors. Measurements of the spectra under various conditions show that the distributions of the *H3* and *H4* centers within the aforementioned ranges are almost uniform.

The following expression can be used to describe the shape of the capacitance-relaxation curve if N_T is comparable to N and $\Delta C/C_0 \ll 1$:

$$\Delta C(t)/C_0 = 0.5K(N_T/N)\exp(-t/\tau) \times (1+B)\{1+B[1-\exp(-t/\tau)]\}. \quad (3)$$

Here, $B = (N_T/N)(1 - C_0/C_\lambda)$. Expression (3) transforms into the following formula for $t = 0$:

$$\Delta C(0)/C_0 = 0.5K(N_T/N)/(1+B). \quad (4)$$

In the case under consideration, the parameter $B \approx 0.3$ and the relaxation curve given by (3) is almost exponential when $\tau \sim 15\%$ is larger and the amplitude, $\sim 20\%$ smaller than the corresponding experimental values. The error in activation energy introduced by conventional analysis of relaxation is much less than the experimental error. The results of calculating the line shape for peak *H4* with the use of formula (3) are shown in Fig. 3. The experimental DLTS line is appreciably widened on the low-temperature side.

We measured the dependence of the capacitance-relaxation amplitude for peak *H4* on the filling-pulse duration t_p in the range of t_p from 4 μs to 1 ms. The results are shown in Fig. 6. It can be seen that the amplitude $\Delta C(0)$ depends linearly on $\ln(t_p)$. For short filling pulses, we have $N_T/N \ll 1$; as a result, $\Delta C(t)/C_0 \propto N_T/N$, so that N_T/N also depends linearly on $\ln(t_p)$.

3. DISCUSSION

When studying the deep levels and identifying them, one should primarily take into account the conditions of crystal growth, the concentrations of the donor or acceptor impurities in the lattice of the compound, and the presence of various types of extended defects (dislocations, grain boundaries, and so on) in the crystal bulk. As mentioned above, the textured polycrystals we studied had low concentrations of intrinsic point defects at the crystal-growth temperature ($\sim 10^{12} \text{ cm}^{-3}$) and of main background impurities ($\leq 10^{15} \text{ cm}^{-3}$), with the dislocation density being lower than 10^3 cm^{-2} ; the prevalent types of extended defects were grain boundaries and twins. Studies of the electrical properties of such crystals have shown that only a small fraction of background impurities occupy the lattice sites and are electrically active. Apparently, the major portion of background impurities are segregated in fields of elastic stresses induced by extended defects, where the complexes giving rise to deep levels are formed as a result of interaction between impurities and between extended defects and impurities. If the concentrations of background impurities and intrinsic point defects are

low, as in the case under consideration, extended defects can profoundly affect the electrical properties of *p*-CdTe.

A large number (from 25 to 30) of deep levels have previously been observed in the band gap of CdTe using different methods [11, 12]. Often, the identification of these levels with certain defects is either ambiguous or lacking.

The electron traps that we observed, E_1 and E_2 , with their levels at $E_c - 0.17 \text{ eV}$ and $E_c - 0.34 \text{ eV}$, have been detected in both high-resistivity [12] and low-resistivity [13, 14] *n*-CdTe crystals and have been identified with Cd_i and V_{Te} defects, respectively [14].

It is well known that the main background impurities in *p*-CdTe (Li, Na, and Cu) occupy the lattice sites and introduce relatively shallow levels into the band gap at a distance from its edges no larger than 0.15 eV. The levels we detected are deeper and, thus, are not directly related to substitutional background impurities.

It is rather difficult to compare (and draw an analogy with) the published DLTS spectra of nominally undoped *p*-CdTe samples obtained by different methods since there is a wide spread in the concentrations and types of background impurities and also in the degree of structural quality from crystal to crystal. In spite of sharp distinctions between the growth of textured polycrystals and nominally undoped *p*-CdTe single crystals, the DLTS spectra of both materials include a number of deep levels whose energy positions and capture cross sections are almost independent of crystallinity. In particular, hole traps with levels close to *H1* ($E_v + 0.24 \text{ eV}$) and *H2* ($E_v + 0.26 \text{ eV}$) [11, 13] and to *H3* ($E_v + 0.45 \text{ eV}$) [15–17] have been observed. A relation of the level at $E_v + 0.45 \text{ eV}$ to the generation of β -type dislocations in *p*-CdTe was ascertained [16]. The corresponding line in the DLTS spectrum featured Gaussian broadening, which was attributed to nonuniformity in the concentration of point defects produced by the generation of dislocations [16].

The DLTS peaks corresponding to the levels whose positions were near the midgap and close to that of the *H4* level ($E_v + 0.86 \text{ eV}$) have been observed in high-resistivity CdTe [11, 12] and, more rarely, in low-resistivity *p*-CdTe [15]. Often, the aforementioned levels were identified with native point defects, e.g., with V_{Cd} centers or with complexes formed from V_{Cd} and an impurity.

When considering a possible relation between the observed levels and extended defects (dislocations, grain boundaries), we should take into account that the main features of DLTS peaks for extended defects are the anomalous shape of these peaks, their broadening, and the logarithmic dependence of the signal amplitude on the filling-pulse duration [2, 3].

The shape of DLTS peaks for extended defects was investigated theoretically by Schröter *et al.* [3]. The corresponding theory [3] can be applied only to the peak *H4*, which has a high intensity and is not distorted

by the superposition of other closely spaced peaks in the spectrum. The peak *H4* (the level at $E_v + 0.86$ eV) has special features (asymmetry, broadening, and logarithmic dependence of the signal amplitude on the filling-pulse duration) that can be described using a model of localized states of an extended defect surrounded with clouds of point defects [3]. The concentration of centers *H4* is indicative of a high dislocation density (apparently, in the vicinity of grain boundaries). Theoretically, a logarithmic dependence of the amplitude of the capacitance-relaxation signal on the filling-pulse duration and the broadening of the DLTS line can be caused by variation in the potential-barrier height near the extended defect after the latter captured a free charge carrier and also by the existence of a band of levels in the band gap. In this case, the position of the peak in the spectrum does not change as the filling-pulse duration increases. The broadening of the DLTS line disappears if the cloud of point defects is spaced farther than 1 nm from the extended defect.

A center with almost the same properties as *H4* was observed by Gelsdorf and Schröter [2] in low-resistivity *n*-CdTe, in which dislocations were generated using plastic deformation. The line in the DLTS spectrum corresponded to the level at $E_c - 0.72$ eV and featured a gently sloping low-temperature wing. The peak amplitude varied with the filling-pulse duration t_p as $\ln(t_p/t_0)$. Taking into account the band gap of CdTe, we may assume that the levels at $E_c - 0.72$ eV and $E_v + 0.86$ eV nearly coincide within the experimental error and, possibly, are related to the same center. On the basis of theoretical concepts, it is assumed [2] that the defect under consideration is a cloud of point defects, which surrounds the dislocation.

It is noteworthy that the defect *H4* has a large cross section for capturing holes and is apparently an acceptor. The presence of this defect, whose concentration is comparable to the concentration of free charge carriers in the material under investigation, indicates that this defect (in addition to shallow acceptors) can play an important role in the compensation of donor impurities. Taking into account the low density of dislocations in a grain, we may assume that the origin of the defect under consideration is related to the grain boundaries. In addition, a level near the midgap typically affects quite profoundly the lifetime of nonequilibrium charge carriers, which is an important parameter of devices based on CdTe.

Thus, among the levels we observed, the level *H4* exhibits special features that can be described by the model of localized states of an extended defect surrounded by a cloud of point defects [3]; notably, the concentration of corresponding centers is indicative of the relatively high density of states most likely related to the grain boundaries. Taking into account the avail-

able published data, we may also assume that the level *H3* is related to dislocations. The shape of the lines E_1 and E_2 is consistent with the results of calculations for local levels that are characteristic of point defects (Fig. 4). It is impossible to relate the levels *H1*, *H2*, and *H3* to any specific types of defects on the basis of corresponding line shapes since the relevant DLTS signals have small amplitudes and are distorted by the superposition of the neighboring lines. In order to clarify the origin of these levels in the band gap of textured polycrystals, additional investigations are required.

ACKNOWLEDGMENTS

This study was supported by the Russian Foundation for Basic Research, project no. 01-02-16500.

REFERENCES

1. R. Rudolph, S. Kawasaki, S. Yamashita, *et al.*, *J. Cryst. Growth* **161**, 28 (1996).
2. F. Gelsdorf and W. Schröter, *Philos. Mag. A* **49**, L35 (1984).
3. W. Schröter, J. Kronewitz, U. Gnauert, *et al.*, *Phys. Rev. B* **52**, 13726 (1995).
4. P. Chattopadhyay, *Solid-State Electron.* **36**, 1641 (1993).
5. A. K. Datta, K. Ghosh, N. K. D. Chowdury, and A. N. Daw, *Solid-State Electron.* **23**, 905 (1980).
6. L. S. Berman and A. A. Lebedev, *Deep-Level Transient Spectroscopy of Deep-Level Centers in Semiconductors* (Nauka, Leningrad, 1981).
7. J.-P. Häring, J. G. Werthen, and R. H. Bube, *J. Vac. Sci. Technol. A* **1**, 1469 (1983).
8. V. I. Strikha, *Theoretical Foundations of Operation of Metal-Semiconductor Contacts* (Naukova Dumka, Kiev, 1974).
9. E. H. Roderick, *IEE Proc., Part I: Solid-State Electron Devices* **129**, 1 (1982).
10. M. A. Green, F. D. King, and J. Shewchun, *Solid-State Electron.* **17**, 551 (1974).
11. M. Samimi, B. Biglari, M. Hage-Ali, *et al.*, *Nucl. Instrum. Methods Phys. Res. A* **283**, 243 (1989).
12. S. G. Elkomoss, M. Samimi, M. Hage-Ali, and P. Siffert, *J. Appl. Phys.* **57**, 5313 (1985).
13. H. Sitter, D. Humenberger, and A. López-Otero, *J. Cryst. Growth* **59**, 229 (1982).
14. G. M. Khattak and C. G. Scott, *J. Phys.: Condens. Matter* **3**, 8619 (1991).
15. G. Zoth and W. Schröter, *Philos. Mag. B* **58**, 623 (1988).
16. I. A. Hummelgen and W. Schröter, *Appl. Phys. Lett.* **62**, 2703 (1993).
17. R. T. Collins and T. C. McGill, *J. Vac. Sci. Technol. A* **1**, 1633 (1983).

Translated by A. Spitsyn

ELECTRONIC
AND OPTICAL PROPERTIES
OF SEMICONDUCTORS

Electron Spin Resonance in $\text{Cd}_{1-x}\text{Mn}_x\text{Te}$
and $\text{Zn}_{1-x}\text{Mn}_x\text{Te}$ Compounds

J. Partyka*, P. W. Żukowski*, P. Węgierek*, A. Rodzik*,
Yu. V. Sidorenko**, and Yu. A. Shostak**

* Lublin Technological University, 20-618 Lublin, Poland

e-mail: pawel@elektron.pol.lublin.pl

** Belarussian State University, ul. Leningradskaya 14, Minsk, 220050 Belarus

Submitted May 14, 2002; accepted for publication June 3, 2002

Abstract—Electron spin resonance in semimagnetic $\text{Cd}_{1-x}\text{Mn}_x\text{Te}$ ($0 < x < 0.7$) and $\text{Zn}_{1-x}\text{Mn}_x\text{Te}$ ($0 < x < 0.53$) compounds was studied at temperatures of 77 and 300 K. It is found that two types of paramagnetic centers exist in $\text{Zn}_{1-x}\text{Mn}_x\text{Te}$, one of which is related to Mn^{2+} ions and the other is attributed to structural defects in the crystals. © 2002 MAIK “Nauka/Interperiodica”.

1. INTRODUCTION

The II–Mn–VI compounds fall in the class of diluted magnetic semiconductors, in which magnetic Mn^{2+} ions are randomly distributed in the II–VI semiconductor host and replace Group II ions [1]. The fact that the aforementioned compounds are ternary makes it possible to vary the structure parameters and, consequently, the relevant properties by varying the transition-metal content. Various applications of these compounds in microelectronics and optoelectronics are based on a number of interesting properties (especially, magnetic and optical) of these compounds.

A combined ionic and covalent bonding is characteristic of II–VI compounds [1]. Irrespective of the type of bonds, the electron spins effecting the bonding are paired and the resultant spin of electrons is equal to zero. Therefore, a perfect (defect-free) II–VI compound is diamagnetic. The introduction of a third (magnetic) component gives rise to paramagnetism in these materials. The presence of localized magnetic ions in these compounds gives rise to specific spin–spin interactions between the *sp* band electrons and the *d* electrons related to the Mn^{2+} ions and, consequently, to very large Zeeman splittings of intrinsic and impurity electron levels and also of intraionic levels (between the Mn *d* electrons). As a result, an appreciable broadening of the electron-spin resonance (ESR) line is observed with increasing Mn concentration.

The magnetic properties of the $\text{Cd}_{1-x}\text{Mn}_x\text{Te}$ and $\text{Zn}_{1-x}\text{Mn}_x\text{Te}$ compounds have already been studied by ESR. A single structureless line was observed for the $\text{Cd}_{1-x}\text{Mn}_x\text{Te}$ compound; this line broadened as the transition-metal concentration increased and as the temperature was lowered. This is caused by the spin–spin coupling and by an increase in the internal-field strength [2, 3]. In the ESR spectra of $\text{Zn}_{1-x}\text{Mn}_x\text{Te}$, a

single line was observed for low Mn concentrations [4], whereas two lines (a broad line and a superimposed narrow line) were observed for high Mn concentrations [5].

Various experimental methods indicate that there are anomalies in the properties of $\text{Zn}_{1-x}\text{Mn}_x\text{Te}$ compounds in the region of low Mn concentrations. For example, the shift of the cathodoluminescence line related to the transition between the conduction and valence bands sets in only at $x > 0.1$ [16].

Previous studies [7, 8] make it possible to establish that the defects present at a high concentration in the $\text{Cd}_{1-x}\text{Mn}_x\text{Te}$ and $\text{Zn}_{1-x}\text{Mn}_x\text{Te}$ compounds affect the crystal's macroscopic parameters such as the dielectric constant and the band gap.

The presence of defects in crystals gives rise to irregularities in the arrangement of neighboring atoms. This irregularity can affect the spin pairing of bonding electrons and, thus, give rise to paramagnetic properties in an imperfect crystal.

The objective of this study was to determine the influence of the defect subsystem on the paramagnetic properties of $\text{Cd}_{1-x}\text{Mn}_x\text{Te}$ and $\text{Zn}_{1-x}\text{Mn}_x\text{Te}$ compounds.

2. EXPERIMENTAL

The ESR spectra of $\text{Cd}_{1-x}\text{Mn}_x\text{Te}$ and $\text{Zn}_{1-x}\text{Mn}_x\text{Te}$ compounds were studied using a Varian spectrometer at a frequency of 9.3 GHz with a magnetic-field modulation frequency of 100 kHz. We measured the ESR spectra at temperatures of 77 and 300 K in single crystals of $\text{Cd}_{1-x}\text{Mn}_x\text{Te}$ ($0 < x < 0.7$) and $\text{Zn}_{1-x}\text{Mn}_x\text{Te}$ ($0 < x < 0.53$) grown by the Bridgman–Stockbarger method. We recorded the first derivative of the ESR absorption line. The absorbed energy is proportional to the total number of unpaired electrons in the sample under investigation.

Parameters of ESR lines for $\text{Cd}_{1-x}\text{Mn}_x\text{Te}$ compounds at temperatures of 77 and 300 K

Sample no.	x	ΔH , G (300 K)		ΔH , G (77 K)	
		Broad line	Narrow line	Broad line	Narrow line
1	0.15	240	Not observed	350	Not observed
2	0.2	310	Not observed	520	Not observed
3	0.30	660	Not observed	2100	215
4	0.50	1410	Not observed	4975	525
5	0.51	1320	160	4425	250
6	0.52	1320	Not observed	Measurements were not performed	
7	0.7	2150	180	Measurements were not performed	
8	0.7	2390	Not observed	6325	600
9	0.7	2275	165	Measurements were not performed	
10	0.7	2300	Not observed	Measurements were not performed	

The concentration of paramagnetic electrons was calculated by comparing the spectra of the investigated and reference samples.

The resonance-line width ΔH was determined as the spacing between the magnetic-field values for which the first derivative of absorption attains its minimum and maximum.

The value of the Lande g -factor was determined from a comparison of the magnetic-field induction H_0 that corresponded to the absorption line at its maximum with the spectrum of the MgO:Mn reference sample. The spectra of the semiconductor sample and the reference were recorded simultaneously.

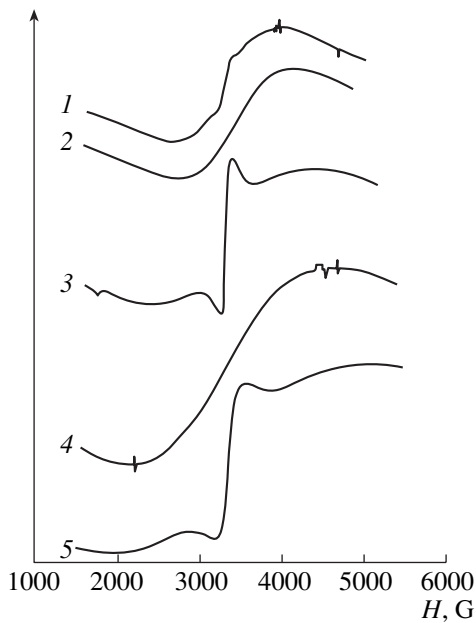


Fig. 1. ESR spectra of $\text{Cd}_{1-x}\text{Mn}_x\text{Te}$: (1) for sample 5 ($x = 0.51$), (2) sample 6 ($x = 0.52$), (3) sample 7 ($x = 0.7$), and (4) sample 8 ($x = 0.7$); spectrum 5 is for a $\text{Zn}_{1-x}\text{Mn}_x\text{Te}$ sample with $x = 0.7$.

3. RESULTS AND DISCUSSION

3.1. $\text{Cd}_{1-x}\text{Mn}_x\text{Te}$ Compounds

The measured ESR spectra of the $\text{Cd}_{1-x}\text{Mn}_x\text{Te}$ samples feature a broad line throughout the entire temperature and composition ranges; this line is related to spin interactions between Mn ions. In some samples with an Mn content of $x \geq 0.3$, a narrow spectral line is observed; this line is superimposed on the broad ESR absorption line (henceforth, we will use the terms “broad line” and “narrow line”; see Fig. 1). The narrow line appears at the position that corresponds to $g \approx 2$. This line is completely separated from the broad line in the spectra of the samples with a high Mn content ($x \geq 0.5$) and at low temperatures. It must be emphasized that the narrow line is irregularly observed in the ESR spectra of the samples with an equal or almost equal content of Mn (see table). As can be seen from the table, a narrow line is observed at room temperature in the ESR spectra of one out of three samples with an Mn content of about 0.50 and in the spectra of two out of four samples with an Mn content of 0.70. A narrow line is also observed in the spectra of samples 3 ($x = 0.30$), 4 ($x = 0.50$), and 8 ($x = 0.70$) at a temperature of 77 K, in which case the width of the line related to Mn^{2+} ions is much wider than that at room temperature. This means that the concentration of centers responsible for the narrow line in the ESR spectra of the aforementioned samples is much lower than in samples 5 ($x = 0.51$) and 7 and 9 ($x = 0.70$), the ESR spectra of which feature a narrow line even at room temperature.

By comparing the parameters ΔH (linewidth) and I (the signal amplitude) measured for the narrow and broad lines in the ESR spectrum of the $\text{Cd}_{1-x}\text{Mn}_x\text{Te}$ sample with $x = 0.30$, we can see that the concentration of paramagnetic centers responsible for the broad line of Mn^{2+} ions is much higher than the concentration of other centers giving rise to the narrow line. For example, in a sample with $x = 0.30$, the amplitudes of two lines almost coincide at 77 K, whereas the resonance-

line widths differ appreciably and amount to 2100 and 215 G. This means that the concentration of unpaired electrons of interacting Mn^{2+} ions is about two orders of magnitude higher than the concentration of the centers giving rise to the narrow absorption line; i.e., the content of these centers is about 0.003.

A cluster model has been suggested [5] in order to account for the second (narrow) ESR line in the $\text{Zn}_{1-x}\text{Mn}_x\text{Te}$ compounds. According to this model, fluctuations in the Mn content give rise to two types of clusters; these are large clusters with an Mn content close to x and small clusters with a lower Mn content. The broad ESR line is related to the former, whereas the narrow line is attributed to the latter. The same model can also be applied to the $\text{Cd}_{1-x}\text{Mn}_x\text{Te}$ compounds studied by us. In our opinion, the irregular appearance of the narrow line in ESR spectra and variation in the line intensity from sample to sample for $\text{Cd}_{1-x}\text{Mn}_x\text{Te}$ crystals with the same or almost the same Mn content suggest that small clusters are formed not only owing to statistical fluctuations in the Mn content; otherwise, a narrow line would be observed in the ESR spectra of all samples with $x = 0.20$. The absence of this line in the ESR spectra of some samples with $x = 0.5$ may be caused by leveling of statistical fluctuations in the Mn content in these crystals during their growth. Thus, the absence of a narrow line in the ESR spectra of some samples may indicate that these samples are more homogeneous.

3.2. $\text{Zn}_{1-x}\text{Mn}_x\text{Te}$ Compounds

The ESR spectra of $\text{Zn}_{1-x}\text{Mn}_x\text{Te}$ (as well as $\text{Cd}_{1-x}\text{Mn}_x\text{Te}$) samples feature a broad line throughout the entire range of temperatures and Mn concentrations under consideration. For $x > 0.20$, a second (narrow) line appears in the ESR spectrum of $\text{Zn}_{1-x}\text{Mn}_x\text{Te}$; this line is superimposed on the broad line (see Fig. 1).

Figures 2 and 3 display the following parameters, which we determined from the ESR spectra: a g -factor, a resonance-line width ΔH , and a relative concentration of paramagnetic electrons N in relation to the Mn content in the $\text{Zn}_{1-x}\text{Mn}_x\text{Te}$ samples under investigation. Results of studying the $\text{Zn}_{1-x}\text{Mn}_x\text{Te}$ ESR spectra have also been reported previously [4, 5]. This study differs from the previous investigations in three aspects. First, we studied a large number of samples, which differed in their Mn content; second, we determined the values of the g -factor with high accuracy; and third, we determined the relative concentrations of paramagnetic electrons in the studied samples. The values of ΔH were previously determined [4, 5] with almost the same accuracy as in this study. The published data on ΔH [4, 5] are shown in Fig. 3 together with the values determined by us. It can be seen that the values of ΔH for four Mn content parameters x [4] and two values of x in [5] are in good agreement with the dependence $\Delta H(x)$ observed in this study.

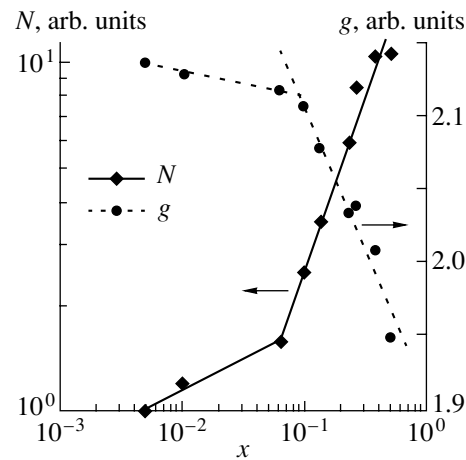


Fig. 2. The values of the g -factor for the broad ESR line and the relative concentration of paramagnetic centers N in $\text{Zn}_{1-x}\text{Mn}_x\text{Te}$ compounds in relation to the content of Mn x ; the ESR spectra were measured at a temperature of 300 K.

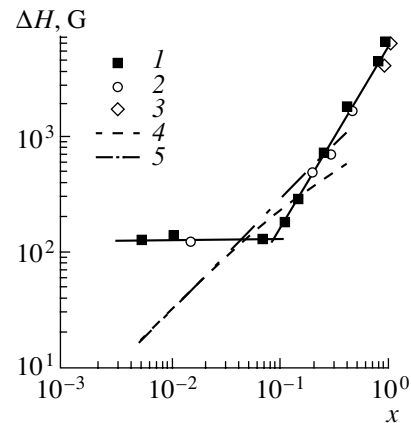


Fig. 3. The width of the ESR absorption line ΔH in $\text{Zn}_{1-x}\text{Mn}_x\text{Te}$ compounds as a function of the Mn content x ; the ESR spectra were measured at a temperature of 300 K. Squares 1 represent experimental results obtained in this study; and circles 2 and diamonds 3 represents the results reported in [4] and [5], respectively. Dashed line 4 corresponds to ΔH_∞ calculated using formula (5) and dash-and-dot line 5 corresponds to ΔH calculated using formula (6).

It follows from Figs. 2 and 3 that two different types of behavior of the ESR spectra in relation to the Mn content can be distinguished. The ESR spectra of samples with an Mn content $x < 0.1$ can be assigned to the first type. For this group of samples, the main parameters of the ESR signal are almost independent of x . For the samples with $x > 0.1$, the g -factor, ΔH , and the concentration of paramagnetic electrons N vary considerably as x increases. The key to gaining insight into the paramagnetism of $\text{Zn}_{1-x}\text{Mn}_x\text{Te}$ compounds is given by the fact that the main characteristics of this phenomenon, which were observed by us in the Mn content region of $x < 0.1$, are virtually independent of x . As can be seen from Fig. 2, the concentration of unpaired elec-

trons increases linearly with an increasing Mn content x for $x \geq 0.1$. This can be readily explained if we take into account that Mn is in the state of Mn^{2+} ions in the $Zn_{1-x}Mn_xTe$ compounds. Each Mn^{2+} ion contains a paramagnetic electron, which is involved in ESR absorption. If the Mn content $x < 0.1$ (Fig. 2), the concentration of paramagnetic electrons far exceeds that of Mn^{2+} ions. This means that, in $Zn_{1-x}Mn_xTe$ compounds with $x < 0.1$, there are paramagnetic centers (in addition to Mn^{2+} ions) unrelated to Mn ions.

The width of the resonance line related to the Mn^{2+} ions depends heavily on the sample temperature T and the Mn content in the sample. In this case, the temperature dependence of ΔH can be written as [4]

$$\Delta H = \Delta H_{\infty}(1 + \Theta/T). \quad (1)$$

Here, ΔH_{∞} is the linewidth at $T \rightarrow \infty$; and $\Theta = \Theta_p + \Theta_d$, where Θ_p is the Curie–Weiss temperature for a paramagnet and Θ_d is the spin temperature.

The quantity ΔH_{∞} is defined in terms of the following factors [4]:

$$\Delta H_{\infty} = \Delta H_{\infty}^{DM} + \Delta H_{\infty}^{dip} + \delta(\Delta H'_{\infty}) + \delta(\Delta H_{\infty}). \quad (2)$$

Here, ΔH_{∞}^{DM} and ΔH_{∞}^{dip} are the contributions of the Dzyaloshinski–Moriya (DM) and dipole interactions to the line broadening at $T \rightarrow \infty$; and $\delta(\Delta H'_{\infty})$ and $\delta(\Delta H_{\infty})$ are the corrections for the linewidth when the spin–orbit pairing of Mn ions and the anisotropy of separate ions are taken into account, respectively.

On the basis of the results of calculations reported previously [4], we ignore the components ΔH_{∞}^{dip} and $\delta(\Delta H_{\infty})$, since these components only slightly affect the final result (by less than 2% of the value of ΔH_{∞}). The remaining two components depend on the Mn content x in the following way [4]:

$$\Delta H_{\infty}^{DM} = f_1(D_1; J_1) \frac{x}{\sqrt{x+0.1}} \quad (3)$$

and

$$\delta(\Delta H'_{\infty}) = f_2(\chi; D_1; D'_1; J_1) \frac{x}{\sqrt{x+0.1}}. \quad (4)$$

Here, χ is the dielectric susceptibility, D_1 is the anisotropic exchange constant, D'_1 is an additional DM constant of the spin–orbit pairing, and J_1 is the isotropic exchange constant.

It can be concluded from (3) and (4) that

$$\Delta H_{\infty} \approx C \frac{x}{\sqrt{x+0.1}}, \quad (5)$$

where $C = f_1(D_1, J_1) + f_2(\chi, D_1, D'_1, J_1)$.

We then use (1) and (5) to derive the following formula, which should describe (to within 2%) the depen-

dence of the width of the ESR line related to Mn^{2+} ions on temperature and the Mn content:

$$\Delta H \approx C \frac{x}{\sqrt{x+0.1}} (1 + \Theta/T). \quad (6)$$

The results of calculations (based on the model [4]) of the quantities ΔH_{∞} and $\Delta H(300 \text{ K}, x)$ are shown in Fig. 3. As can be seen from Fig. 3, the calculated values of these quantities are close to the experimental values only for $x \geq 0.15$. In the region of low Mn concentrations, the experimentally determined value of $\Delta H(300 \text{ K}, x)$ is constant.

The discrepancy between the values obtained in our experiments and those calculated according to the model [4] can be explained in the following way. There are two types of paramagnetic centers in the $Zn_{1-x}Mn_xTe$ compounds under consideration. One of these is related to the paramagnetism of Mn^{2+} ions. The presence of Mn^{2+} ions gives rise to paramagnetic properties of $Zn_{1-x}Mn_xTe$ compounds for $x > 0.10$; i.e., we have a linear increase in the concentration of unpaired electrons, an increase in the width ΔH of the broad absorption band, and a decrease in the g -factor for this line (Figs. 2, 3). A model of two types of clusters (see [5]) can be used in this region of Mn concentrations: large clusters give rise to the broad ESR line of Mn^{2+} ions, whereas small clusters are responsible for the narrow line, which was observed both in this study and in [5].

In our opinion, paramagnetic centers of the second type are not directly related to the Mn^{2+} ions and govern the magnetic properties of the crystals in the region of $x < 0.1$. The most important evidence for the presence of paramagnetic centers of this type in the samples is provided by the fact that the concentration of unpaired electrons at $x < 0.1$ far exceeds the concentration of Mn^{2+} ions (Fig. 2) and the linewidth ΔH and the g -factor are independent of x (Figs. 2, 3).

4. CONCLUSION

A comparison of the results of studying the ESR spectra for the $Cd_{1-x}Mn_xTe$ and $Zn_{1-x}Mn_xTe$ samples has made it possible to infer that the paramagnetic properties of $Zn_{1-x}Mn_xTe$ compounds are determined by two types of paramagnetic centers. The centers of the first type are related to the presence of Mn^{2+} ions in the compounds under consideration; these ions give rise to broad and narrow lines in the ESR spectra at $x = 0.20$. The second type of paramagnetic centers gives rise to a narrow ESR line at $x < 0.10$. We assume that the centers of the second type are related to structural defects in the compounds under consideration. The presence of these defects also accounts for both the experimentally observed fluctuations in the band gap in $Zn_{1-x}Mn_xTe$ compounds and the constant energy position of the line that corresponds to a transition from the conduction band to the valence band and which is

observed in the cathodoluminescence spectra in the region of small values of x [6, 8].

REFERENCES

1. *Diluted Magnetic (Semimagnetic) Semiconductors*, Ed. by R. L. Aggarwal, J. K. Furdyna and S. von Molnar (Materials Research Society, Pittsburgh, 1987; Mir, Moscow, 1992).
2. S. B. Oseroff, Phys. Rev. B **25**, 6584 (1982).
3. N. Samarth and J. K. Furdyna, Phys. Rev. B **37**, 9227 (1988).
4. Z. Šoškić, B. Babić Stojić, and M. Stojić, J. Phys.: Condens. Matter **6**, 1261 (1994).
5. Z. Šoškić and B. Babić Stojić, J. Magn. Magn. Mater. **140–144**, 2071 (1995).
6. A. Hołda, A. Rodzik, A. A. Melnikov, and P. Żukowski, Acta Phys. Pol. A **88**, 739 (1995).
7. P. W. Żukowski, A. Rodzik, and Yu. A. Shostak, Fiz. Tekh. Poluprovodn. (St. Petersburg) **31**, 714 (1997) [Semiconductors **31**, 610 (1997)].
8. P. V. Zhukovskiĭ Ya. Partyka, P. Vengerek, *et al.*, Fiz. Tekh. Poluprovodn. (St. Petersburg) **35**, 937 (2001) [Semiconductors **35**, 900 (2001)].

Translated by A. Spitsyn

**SEMICONDUCTOR STRUCTURES,
INTERFACES, AND SURFACES**

Deep Levels in the Band Gap of GaN Layers Irradiated with Protons

**M. M. Sobolev*, N. A. Sobolev*[^], A. S. Usikov*, N. M. Shmidt*,
A. N. Yakimenko**, G. M. Gusinskii*, and V. O. Naidenov***

* *Ioffe Physicotechnical Institute, Russian Academy of Sciences,
Politekhnicheskaya ul. 26, St. Petersburg, 194021 Russia
^e-mail: nick@sobolev.ioffe.rssi.ru*

** *St. Petersburg State Polytechnical University,
Politekhnicheskaya ul. 29, St. Petersburg, 195251 Russia
Submitted April 16, 2002; accepted for publication May 15, 2002*

Abstract—Deep-level transient spectroscopy was used to study the parameters of deep levels in the band gap of epitaxial *n*-GaN layers after irradiation of the Schottky barriers with 1-MeV protons to a dose of 10^{12} cm⁻². A deep level *EP1* with an activation energy of 0.085 eV was introduced by irradiation into the upper half of the GaN band gap. The introduction rate of the corresponding defect was found to depend on the bias voltage applied to the Schottky barrier during irradiation. © 2002 MAIK “Nauka/Interperiodica”.

1. INTRODUCTION

Rapid progress in the development of blue, green, and ultraviolet (UV) light-emitting diodes; blue lasers; UV detectors; and high-temperature high-power electronic devices based on GaN and its solid solutions has aroused an active interest in the processes of defect formation in III-nitride systems [1, 2]. Studies of radiation effects in GaN contribute to the development of defect engineering; at the same time, such studies have already made it possible to improve the parameters of high-speed switches and detectors [3, 4]. The study of radiation defects by deep-level transient spectroscopy (DLTS) is still in its early stage. The results of several studies concerned with the effects of irradiation with protons, fast electrons, gamma-ray photons, and helium ions on the spectrum of deep levels in the band gap have been reported [5–8]. There exist several methods that make it possible to exert an additional effect on the spectrum of introduced radiation defects; these methods include varying the temperature of the irradiated sample, illuminating the sample, and passing an electric current through the sample. The objective of this study is to gain insight into the influence of the bias voltage applied to the Schottky barrier on the spectrum of deep levels formed as a result of proton irradiation.

2. EXPERIMENTAL

Films of *n*-GaN doped lightly with Si were grown on Al₂O₃ (0001) substrates using metal-organic chemical vapor deposition (MOCVD). A buffer GaN layer with a thickness of ~20 nm was first deposited at 500°C; an epitaxial GaN layer with a thickness of 3–4 μm was then grown at 1040°C. The electron concentration in

these layers was in the range from 6×10^{16} to 3×10^{17} cm⁻³. The Schottky barriers and ohmic contacts were formed by the sputter deposition of Ni/Au and Ti/Al/Ni/Au, respectively. The Schottky barrier area and height were 0.18 mm² and 0.8 V, respectively. The leakage currents were lower than 10 μA at a reverse bias voltage of up to 20 V. The samples were irradiated with 1-MeV protons using the cyclotron at the Ioffe Physicotechnical Institute; the dose was 1×10^{12} cm⁻². Two Schottky barriers that had been formed on the same substrate were irradiated simultaneously; one of these barriers was unbiased, whereas a forward or reverse bias voltage of ±13 V was applied to the other barrier. In the course of irradiation with protons, we did not observe an increase in the forward current; at the same time, the reverse current increased by almost three orders of magnitude.

Radiation defects were studied by DLTS using a DL 4600 spectrometer produced by BIO-RAD Polaron Equipment; the probing frequency was 1 MHz, and the emission-rate windows were 80, 200, 400, and 1000 s⁻¹. The samples were preliminarily heated to 450 K and were then cooled to 80 K with a reverse bias voltage applied; after that, the DLTS spectra were recorded in the course of heating the samples. The duration of the pulses that filled the levels with electrons during measurements was 4 μs. The level parameters (the activation energy *E* and the cross section of electron capture σ by the level) were determined from the Arrhenius equation on the assumption that σ is temperature-independent; i.e.,

$$e/T^2 = b\sigma \exp(-E/kT), \quad (1)$$

where e is the rate of thermal emission of electrons from the level to the conduction band, T is temperature, $b = 3.3 \times 10^{20} \text{ cm}^{-2} \text{ s}^{-1} \text{ K}^{-2}$ [6], and k is the Boltzmann constant.

3. RESULTS AND DISCUSSION

Typical DLTS spectra of the samples irradiated with protons for several bias voltages applied to the Schottky barriers are shown in Fig. 1. The spectra were measured with a reverse bias of -8 V applied to the Schottky barrier. The levels were filled when the reverse voltage was decreased to -0.5 V . Five deep levels $EP1-EP5$ are observed; the shallowest level $EP1$ is formed only in the Schottky barriers that were unbiased during the irradiation with protons (Fig. 1, spectrum c).

Dependences of the rates of electron thermal emission from the deep levels to the conduction band on the reciprocal temperature are shown in Fig. 2 (circles). The activation energies E of the levels and the cross sections of electron capture σ by these levels as calculated from the Arrhenius equation (1) were found to be equal to $E_1 = 0.085 \text{ eV}$, $E_2 = 0.16 \text{ eV}$, $E_3 = 0.48 \text{ eV}$, $E_4 = 0.56 \text{ eV}$, and $E_5 = 0.60 \text{ eV}$; and $\sigma_1 = 3.5 \times 10^{-19} \text{ cm}^2$, $\sigma_2 = 3.8 \times 10^{-18} \text{ cm}^2$, $\sigma_3 = 3.5 \times 10^{-16} \text{ cm}^2$, $\sigma_4 = 5.3 \times 10^{-16} \text{ cm}^2$, and $\sigma_5 = 4.3 \times 10^{-17} \text{ cm}^2$.

In order to identify the levels, we compared the temperature dependences of the rates of electron thermal emission from these levels with those for the levels in the band gap of n -GaN irradiated with 2-MeV protons to a dose of $3 \times 10^{11} \text{ cm}^{-2}$ [5], 5.4-MeV helium ions at doses of $(0.4-2.5) \times 10^{11} \text{ cm}^{-2}$ [8], 1-MeV electrons at doses of 5×10^{14} and $1 \times 10^{15} \text{ cm}^{-2}$ [6], and ^{60}Co gamma quanta at a dose of $1.2 \times 10^{19} \text{ cm}^{-2}$ [7]. The experimental dependences of emission rates on reciprocal temperature reported in publications [5-8] are shown in Fig. 2. The deep levels observed in the corresponding studies were denoted as $EO1-EO5$ and $ER1-ER4$ [5, 8]; $E1-E4$ [6]; and $B, C, D,$ and E [7]. The temperature dependences of emission rates for the levels $EP2, EP3, EP4,$ and $EP5$ in the band gap of our samples are almost equal to those for the group $(EO2, D, E1), (EO3, C), (EO5, B, E2),$ and $E3$ of the four levels observed in [5-8] after the Schottky barriers were formed before irradiation.

The $EP1$ level was observed in the DLTS spectra of our irradiated samples only if an external bias was not applied to the Schottky barrier in the course of irradiation. Typically, the formation of centers with deep levels in III-V semiconductors irradiated with protons with energies lower than several megaelectronvolts is controlled by quasi-chemical reactions between point intrinsic lattice defects and impurity atoms [9]. Notably, both neutral and charged point defects are involved in these reactions. Application of an external electric field affects the quasi-chemical reactions that proceed with the participation of charged point defects. Therefore, the absence of the $EP1$ level in the band gap of our

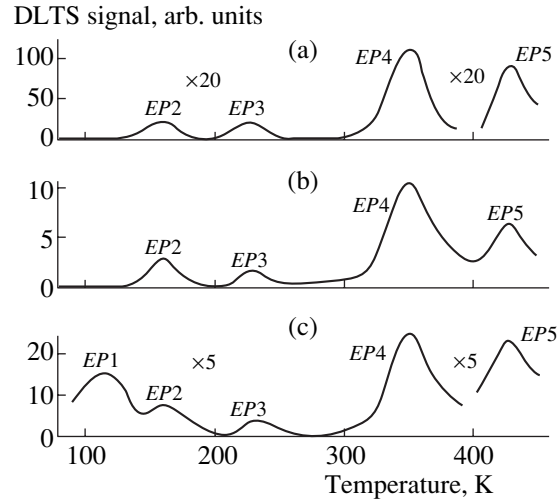


Fig. 1. DLTS spectra of proton-irradiated Schottky barriers; the bias voltages applied to the barriers during irradiation were (a) +13, (b) -13, and (c) 0 V.

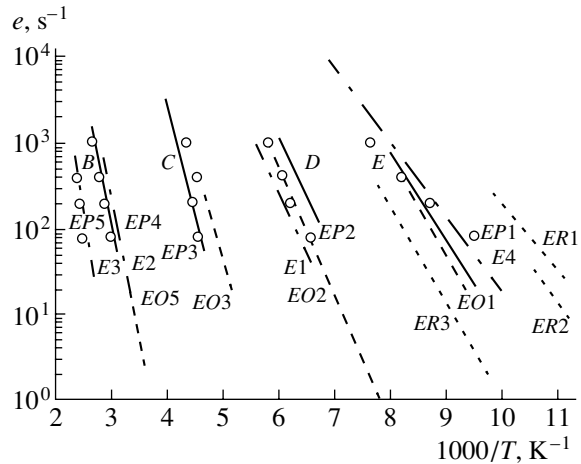


Fig. 2. Temperature dependences of the rates of electron emission from deep levels observed in this study (circles) and also reported in [5, 8] (dashed and dotted lines), [6] (the solid lines), and [7] (the dash-and-dot lines).

samples, to which an external bias was applied during irradiation, indicates that charged point defects play an important role in the formation of the corresponding center. In other words, the formation of the $EP1$ center is controlled by a charge-sensitive quasi-chemical reaction. It is highly probable that different physical mechanisms are responsible for suppression of the formation of the $EP1$ center when forward- and reverse-bias voltages are applied to the Schottky barrier [9].

In contrast to our samples, three deep levels ($ER1, ER2,$ and $ER3$) were observed by Auret *et al.* [5] in the band gap of GaN irradiated with protons; the rates of emission of electrons from these levels in the same temperature range differ from those from the $EP1$ center observed in this study by a factor of 2-10. At the same

time, a single level designated as either E [6] or $E4$ [7] was observed in the band gap of the samples irradiated with electrons [6] and gamma quanta [7]; these levels feature electron emission rates close to that of the $EP1$ level. Apparently, these results are related to the influence of extended growth defects and internal stresses in the samples under investigation on the processes of radiation-defect formation. It is well known that epitaxial GaN layers have a high concentration of defects including dislocations with a density of 10^7 – 10^{10} cm^{-2} , a developed mosaic structure, and a high concentration of impurity atoms (hydrogen, carbon, oxygen, and so on). In the samples we studied, the dislocation density was 10^8 – 10^9 cm^{-2} . Often, the most profound influence on the defect spectrum is exerted by the method of growing the layers. Auret *et al.* [5] studied samples grown using the gaseous-phase epitaxy from metal-organic compounds (OMVPE), whereas layers obtained by MOCVD were studied by us and in [6, 7]. Differences in the values of the activation energies and electron-capture cross sections calculated using the Arrhenius curves between the levels $EP1$ and E ($E_E = 0.18$ eV and $\sigma_E = 2.5 \times 10^{-15}$ cm^2) and $EP1$ and $E4$ ($E_{E4} = 0.15$ eV and $\sigma_{E4} = 2 \times 10^{-16}$ cm^2) are apparently caused by the influence of a number of technological factors (quality of the substrates, growth conditions, purity of starting materials, and so on) on the structural quality and internal local stresses in the MOCVD layers. The introduction rate for the $EP1$ defect detected after irradiation with 1-MeV protons is about 50 cm^{-1} . For comparison, the introduction rates of defects produced by 2-MeV protons were 30 cm^{-1} (for the $ER1$ defect), 400 cm^{-1} (for $ER2$), and 600 cm^{-1} (for $ER3$); notably, the introduction rate of defects E as a result of irradiation with 1-MeV electrons was no higher than 0.2 cm^{-1} . It is noteworthy that the DLTS lines for the $EP1$, E , and $E4$ defects are somewhat broadened and are possibly related to several levels. This possibility should be analyzed in further studies.

4. CONCLUSION

Five deep levels were observed in the band gap of epitaxial n -GaN layers whose Schottky barriers were irradiated with 1-MeV protons. The formation of a level characterized by the thermal electron-emission rate $e = 3.5 \times 10^{-19} b T^2 \exp(-0.085/kT)$ is caused by irradiation with protons and depends on the bias voltage applied to the Schottky barrier during irradiation. The introduction rate of this level is 50 cm^{-1} if the bias voltage is not applied in the course of irradiation.

ACKNOWLEDGMENTS

This study was supported in part by the Civil Research and Development Foundation, grant no. RP1-2258.

REFERENCES

1. S. Nakamura, S. Pearton, and G. Fasol, *The Blue Laser Diode* (Springer-Verlag, Berlin, 2000).
2. H. Markoc, Springer Ser. Mater. Sci. **32** (1999).
3. M. Lambsdorff, J. Kohl, J. Rosenzweig, *et al.*, Appl. Phys. Lett. **58**, 1881 (1991).
4. V. M. Rao, W.-P. Hong, C. Caneau, *et al.*, J. Appl. Phys. **70**, 3943 (1991).
5. F. D. Auret, S. A. Goodman, F. K. Koschnick, *et al.*, Appl. Phys. Lett. **74**, 407 (1999).
6. Z.-Q. Fang, J. W. Hemsley, D. C. Look, and M. P. Mack, Appl. Phys. Lett. **72**, 448 (1998).
7. D. V. Davydov, V. V. Emtsev, A. A. Lebedev, *et al.*, Mater. Sci. Forum **353–356**, 799 (2001).
8. F. D. Auret, S. A. Goodman, F. K. Koschnick, *et al.*, Appl. Phys. Lett. **73**, 3745 (1998).
9. D. Ponce and G. C. Bourgoin, J. Phys. C **18**, 3839 (1985).

Translated by A. Spitsyn

SEMICONDUCTOR STRUCTURES, INTERFACES, AND SURFACES

Band-Edge Line-up in GaAs/GaAsN/InGaAs Heterostructures

A. Yu. Egorov[^], V. A. Odnoblyudov, N. V. Krizhanovskaya,
V. V. Mamutin, and V. M. Ustinov

*Ioffe Physicotechnical Institute, Russian Academy of Sciences,
Politekhnicheskaya ul. 26, St. Petersburg, 194021 Russia*

[^] e-mail: anton@beam.ioffe.rssi.ru

Submitted May 21, 2002; accepted for publication May 22, 2002

Abstract—Triple GaAs/GaAsN/InGaAs heterostructures were grown by MBE on GaAs substrates, and their optical properties were studied. The band-edge line-up in GaAs/GaAsN and InGaAs/GaAsN heterostructures was analyzed by correlating the experimental photoluminescence spectra with the known parameters of the band diagram in (In,Ga)As compounds. It is shown that a GaAs/GaAsN heterojunction is type I, while an $\text{In}_x\text{Ga}_{1-x}\text{As}/\text{GaAsN}$ heterojunction can be type I or type II, depending on the In content x . © 2002 MAIK “Nauka/Interperiodica”.

1. INTRODUCTION

In recent years, (In,Ga)AsN compounds have been a subject of intensive theoretical and experimental studies. The interest in these semiconductors is due to their potential applicability in the design of near-IR (1.3–1.55 μm) lasers on GaAs substrates, and to the dependence of their band gap on the composition of a GaAsN solid solution, which is uncommon in III–V compounds. In spite of evident progress in the development of device structures with an InGaAsN active region, several issues concerning the fundamental properties of this material remain open. One of the unresolved questions is the line-up of band edges in GaAs/GaAsN and InGaAs/GaAsN heterojunctions. Several theories have been developed [1–3] to describe the behavior of the valence band edge in GaAsN compounds (Fig. 1). According to [1], a type-II heterojunction is formed at the GaAs/GaAsN interface, while the other mentioned models provide evidence in favor of a type-I heterojunction.

In this communication, we present experimental data indicating that GaAs/GaAsN is a type-I heterojunction and that an $\text{In}_x\text{Ga}_{1-x}\text{As}/\text{GaAsN}$ heterojunction can be either type I or type II, depending on x .

2. EXPERIMENTAL RESULTS

Triple heterostructures were grown on (001) GaAs substrates by MBE from solid-state sources. An RF plasma source Unibulb EPL was used as a source of nitrogen. The composition and thickness of the grown layers were determined with an error of $\pm 1\%$ from the photoluminescence (PL) and X-ray data. The sequence

of layers in the heterostructures under study is shown in Fig. 2.

The photoluminescence (PL) of the asymmetrical triple heterostructures was recorded at temperatures of 300, 77, and 18 K. The PL was excited by an Ar-ion laser with a 514-nm wavelength and with an excitation density of 100 W cm^{-2} . Two heterostructures were studied. Structure no. 1 was GaAs/GaAs_{0.98}N_{0.02}/In_{0.45}Ga_{0.55}As/GaAs. The thickness of the GaAs_{0.98}N_{0.02} and In_{0.45}Ga_{0.55}As layers was 20 and 1.8 nm, respectively. Structure no. 2 was GaAs/GaAs_{0.98}N_{0.02}/In_{0.64}Ga_{0.36}As/GaAs, with a GaAs_{0.98}N_{0.02} and In_{0.64}Ga_{0.36}As layer thickness of

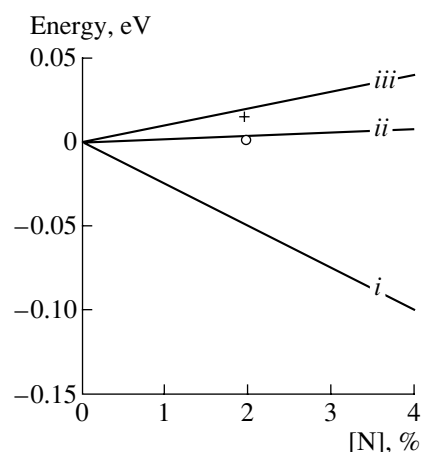


Fig. 1. The position of the valence band edge in GaAsN vs. the nitrogen content. Lines: calculated in terms of models: (i) dielectric [1]; (ii) tight-binding [2]; (iii) LDA [3]. Symbols: experimental data for a compound with 2% of nitrogen: (+) elastically strained GaAsN on GaAs; (o) unstrained GaAsN.

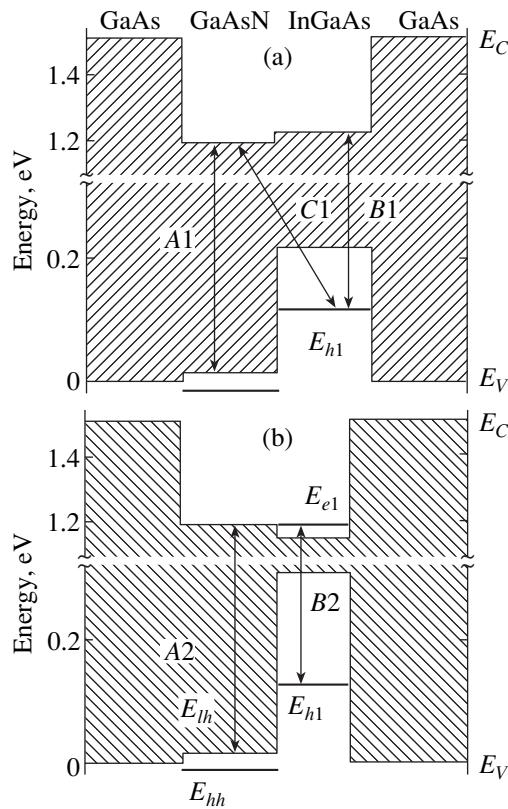


Fig. 2. Band diagram of GaAs/GaAsN/InGaAs heterostructures. (a) Heterostructure no. 1: GaAs/GaAs_{0.98}N_{0.02}/In_{0.45}Ga_{0.55}As/GaAs; the thickness of the GaAs_{0.98}N_{0.02} and In_{0.45}Ga_{0.55}As layers is 20 and 1.8 nm, respectively. (b) Structure no. 2: GaAs/GaAs_{0.98}N_{0.02}/In_{0.64}Ga_{0.36}As/GaAs; the thickness of the GaAs_{0.98}N_{0.02} and In_{0.64}Ga_{0.36}As layers is 20 and 1.4 nm, respectively. E_{e1} , E_{h1} are the quantum-well levels for electrons and holes. The position of the valence band edge in strained GaAsN is defined by the light hole energy, E_{lh} [5]. The split-off level E_{hh} is the heavy hole energy [5].

20 and 1.4 nm, respectively. The thicknesses of all the layers constituting the structures did not exceed the critical one.

Figure 3 presents the PL spectra of heterostructure no. 1. At room temperature, the dominating peak is A1; it arises from the transitions between the valence and conduction bands of the GaAsN layer (this correspondence was established based on the PL spectra of 0.2- μ m-thick GaAsN layers grown on GaAs). Another peak observed is B1 (it forms a shoulder at the low-energy edge of the spectrum), which can be related to the emission of the InGaAs layer. At the liquid nitrogen temperature, the B1 peak dominates. Thus, the PL emission peak shifts to lower energies as the temperature decreases, in contrast to standard PL behavior which is defined by an increase of the band gap as the temperature decreases. At an even lower temperature (18 K), the PL spectra exhibit two peaks (see upper part of Fig. 3): peak B1, which is related to the emission from InGaAs, and peak C1, which has a lower energy.

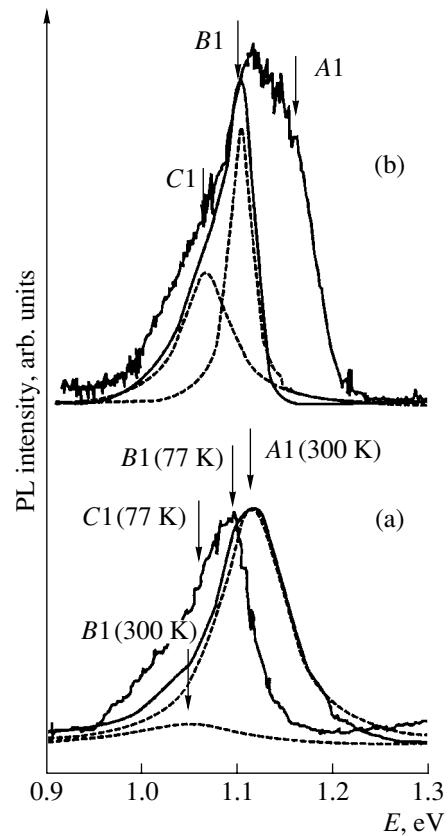


Fig. 3. PL spectra of heterostructure no. 1, GaAs/GaAs_{0.98}N_{0.02}/In_{0.45}Ga_{0.55}As/GaAs. Temperatures: (a) 300 and 77 K; (b) 18 K. The thickness of the GaAs_{0.98}N_{0.02} and In_{0.45}Ga_{0.55}As layers is 20 and 1.8 nm, respectively. Dashed lines demonstrate the decomposition of spectrum into components.

The energy difference between peaks B1 and C1 was 34 ± 2 meV. With the excitation density increasing, the PL spectrum at 18 K broadened and the peak shifted to higher energies. A shoulder appeared at the high-energy edge of the spectrum, with the energy corresponding to the emission of the GaAsN layer. We believe, therefore, that, at cryogenic temperatures, we observed the radiative recombination of carriers localized in the InGaAs layer, as well as radiative transitions whose energy was lower than the energy of radiative transitions in the InGaAs layer. At room temperature, the carriers are delocalized from the InGaAs layer and the recombination in the GaAsN layer dominates.

Figure 4 shows the PL spectra of heterostructure no. 2. At room temperature, two peaks of comparable intensity are clearly visible. A more prominent peak A2 corresponds to the emission of the GaAsN layer, we assign the other peak B2 to the emission from the InGaAs layer. A single symmetrical peak B2 is observed at 77 K, which is presumably related to the

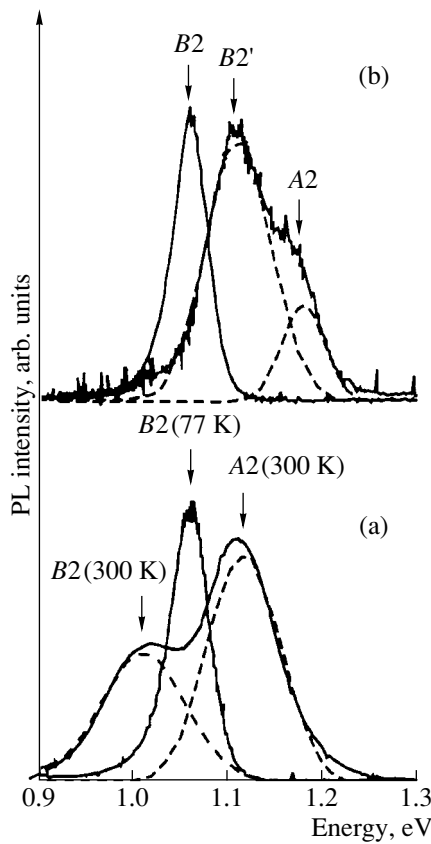


Fig. 4. PL spectra of heterostructure no. 2, GaAs/GaAs_{0.98}N_{0.02}/In_{0.64}Ga_{0.36}As/GaAs. Temperatures: (a) 300 and 77 K; (b) 18 K. The thickness of the GaAs_{0.98}N_{0.02} and In_{0.64}Ga_{0.36}As layers is 20 and 1.4 nm, respectively. Dashed lines demonstrate the decomposition of spectrum into components.

InGaAs layer. A single symmetrical peak *B2* is also observed at low temperature (18 K). When the excitation density is considerably enhanced, an *A2* shoulder is observed at 18 K on the high-energy edge of the PL spectrum; it corresponds to the emission of the GaAsN layer. With the exception of the steady shift of the PL peak to higher energies, no other modifications of the spectrum were observed under these conditions. Thus, at cryogenic temperatures, the carriers are completely localized in the layer with a smaller band gap, i.e., InGaAs. At room temperature, the thermal broadening

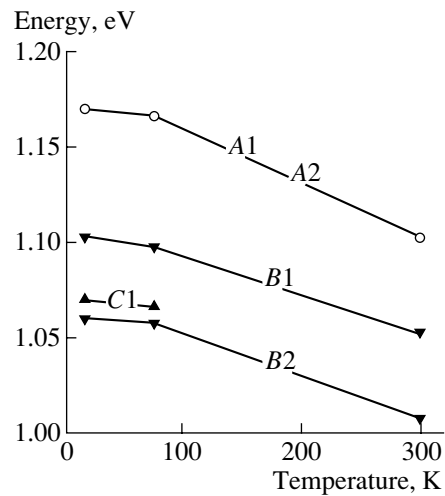


Fig. 5. Temperature dependences of the radiative transition energy for heterostructure nos. 1 and 2. *A1* and *A2*: spatially direct transitions between the valence and conduction bands of GaAsN layer in structure nos. 1 and 2, respectively. *B1*: spatially direct transition between holes localized at the quantum-well level of the InGaAs layer and electrons localized in the InGaAs conduction band, structure no. 1. *B2*: spatially direct transition between holes and electrons localized at the quantum-well level of the InGaAs layer, structure no. 2. *C1*: spatially indirect transition between holes localized at the quantum-well level of the InGaAs layer and electrons localized in the GaAsN conduction band, structure no. 1.

of the Fermi level leads to the population of states in GaAsN layer. An important difference between the PL spectra of heterostructures nos. 1 and 2 is as follows: only in heterostructure no. 1 do we observe a peak with an energy below the possible energy of spatially direct transitions in the constituent layers. The only significant difference in the design of the studied heterostructures is the composition of the InGaAs layer. The In content was 45% in one structure and 64% in the other.

Figure 5 demonstrates temperature dependences of the energy of peaks forming the PL spectra. The energy values of the radiative transitions are presented in the table. A detailed analysis of the PL spectra and their resolution into peaks related to specific radiative transitions reveals regular trends in the temperature dependences of the transition energies: these energies

Radiative transition energies in heterostructure nos. 1 and 2

Temperature of experiment, K	A1, eV	B1, eV	C1, eV	A2, eV	B2, eV
18	1.170	1.103	1.069	1.170	1.06
77	1.167	1.098	1.066	1.167	1.057
300	1.102	1.051		1.102	1.008

increase as the temperature decreases, following the increase of the band gaps in the compounds forming the heterostructure.

3. DISCUSSION

The obtained experimental data will be discussed on the basis of the band diagram of the heterostructures grown; this diagram is presented in Fig. 2, and it reflects the situation at the temperature of 18 K. The starting point of its construction is the GaAs band gap, 1.514 eV. The band gaps of InGaAs are determined as 1.008 and 0.838 eV for the compounds with 45 and 64% In content, respectively. The conduction band offsets are set as 58.2 and 54.5% of the difference between the band gap values for the compounds with an In content of 45 and 64%, respectively [4]. The spacings between the quantum-well levels in InGaAs layers and the band gap of GaAsN (1.170 eV) are determined from the PL spectra. The position of the conduction band edge in GaAsN is the most important feature of the diagram. For heterostructure no. 1, this position, with respect to the conduction band edge in InGaAs, is determined based on the following experimental data.

(i) The observed energy of the transition identified as the transition in the InGaAs layer of the heterostructures under study is substantially lower than that of GaAs/InGaAs/GaAs heterostructures. A correspondence can be established if we observe the transitions between the quantum-well level of holes and the InGaAs conduction band edge ($B1$). We believe that, in both heterostructures under study, the position of the quantum-well level of holes coincides with the level of holes in a GaAs/InGaAs/GaAs quantum well (QW), owing to an insignificant change of the potential barrier when the GaAs layer is replaced with GaAsN on one side of the structure (see Fig. 1).

(ii) The most probable reason for the appearance of the low-energy transition observed at cryogenic temperatures, with an energy lower than the band gap of GaAsN or InGaAs (defined as the distance between the conduction-band edge and the first quantum-well level for holes), is spatially indirect transitions involving electrons localized in the GaAsN layer and holes localized at the quantum-well level of holes in the InGaAs layer.

(iii) The shift of the PL peak to higher energies when the temperature is elevated to 300 K can be assigned to the dominating recombination of nonequilibrium carriers across the GaAsN layer, which is due to the existence of a type-II heterojunction on the GaAsN/InGaAs interface in heterostructure no. 1.

Thus, the energy difference between the spatially direct transitions ($B1$, between the quantum-well levels for holes and the conduction band edge in the InGaAs layer) and spatially indirect transitions (between the

quantum-well level for holes in the InGaAs layer and the conduction-band edge in the GaAsN layer) is 34 meV, and it defines the line-up of the conduction-band edges of both compounds.

The position of the valence band edge in GaAsN is now determined by subtracting its band gap value from the position of the conduction band edge. In heterostructure no. 2, the In content in the InGaAs layer was raised to 64%. Due to the higher In concentration, the band gap of the compound decreased and the conduction band edge lowered. In turn, this changed the type of the heterojunction at the GaAsN/InGaAs interface. Heterostructure no. 2 contains a type-I heterojunction with a low localization energy for electrons in the region of the InGaAs QW. This gives rise to distinct $B2$ peaks in the PL spectrum at room temperature (Fig. 4). For heterostructure no. 2, the lowest energy transitions are the spatially direct transitions between the quantum-well levels in the InGaAs QW. The position of the quantum-well level for electrons coincides with the conduction band edge of GaAsN, owing to the small depth and width of the formed QW. The quantum-well level for holes is the same as in the first case.

At cryogenic temperatures, when there is no temperature broadening of the Fermi level, all the carriers are localized at the InGaAs QW and the PL spectrum is symmetrical. No specific features pointing to the occurrence of spatially indirect transitions are observed.

It is necessary to note that the band diagrams presented in Fig. 2 are based on the entire body of experimental data observed in the study of heterostructures nos. 1 and 2. An exact correlation between the transition energies and the line-up of band edges of the compounds shown in Fig. 2 is observed only with the above-listed values of the conduction-band offset in an InGaAs/GaAs heterojunction, which is the second crucial point in the construction of the diagram. The unambiguous identification of all the energies cannot be achieved with other values of the conduction-band offset in an InGaAs/GaAs heterojunction.

4. CONCLUSION

A comparison of the experimentally observed PL spectra with the known parameters of the band diagram of (In,Ga)As compounds allowed us to determine the line-up of the band edges in GaAs/GaAsN and InGaAs/GaAsN heterostructures. It is shown that GaAs/GaAsN is a type-I heterojunction, while the $\text{In}_x\text{Ga}_{1-x}\text{As}/\text{GaAsN}$ heterojunction may be type I or type II, depending on the value of x . It is established from the experiment that the valence band edge of $\text{GaAs}_{0.98}\text{N}_{0.02}$ grown on GaAs lies at 15 ± 5 meV above the valence band edge of GaAs (see Fig. 1). Without

mechanical stress, the difference between the valence band edges of GaAs and GaAs_{0.98}N_{0.02} is almost zero (0 ± 5 meV) if the effect of stress on the position of the valence band edge in GaAsN is taken into consideration according to [5].

ACKNOWLEDGMENTS

This study was supported by the program NATO SFP, the Ministry of Science program "Physics of Solid-State Nanostructures," the Russian Foundation for Basic Research, and by the Civilian Research and Development Foundation (RE-2221).

REFERENCES

1. S. Sakai, Y. Ueta, and Y. Terauchi, *Jpn. J. Appl. Phys.* **32**, 4413 (1993).
2. A. Lindsay and E. P. O'Reilly, *Solid State Commun.* **112**, 443 (1999).
3. L. Bellaiche, S.-H. Wei, and A. Zunger, *Phys. Rev. B* **54**, 17568 (1996).
4. G. Ji, D. Huang, U. K. Reddy, *et al.*, *J. Appl. Phys.* **62**, 3366 (1987).
5. A. Yu. Egorov, E. S. Semenova, V. M. Ustinov, *et al.*, *Fiz. Tekh. Poluprovodn. (St. Petersburg)* **36** (9), 1056 (2002) [*Semiconductors* **36**, 981 (2002)].

Translated by D. Mashovets

**LOW-DIMENSIONAL
SYSTEMS**

Analysis of Inelastic Scattering of Quasi-Two-Dimensional Electrons of a Superlattice by Acoustic Phonons with Allowance Made for the Miniband Dispersion

S. I. Borisenko

Kuznetsov Siberian Physicotechnical Institute, pl. Revolyutsii 1, Tomsk, 634050 Russia

e-mail: sib@elefot.tsu.ru

Submitted April 15, 2002; accepted for publication April 16, 2002

Abstract—Formulas for the effective momentum-relaxation time and mobility of quasi-two-dimensional electrons of a superlattice with consideration of inelastic scattering by acoustic phonons and the dispersion of the miniband energy spectrum as a function of the longitudinal wave vector have been obtained. Numerical calculation was performed for a nondegenerate gas of quasi-2D electrons in a symmetrical GaAs/Al_{0.36}Ga_{0.64}As superlattice with a quantum well width of 5 nm at $T = 77$ K. It was shown that consideration of the elasticity of scattering and the dispersion of the miniband energy spectrum gives rise to a significant increase in the electron mobility. © 2002 MAIK “Nauka/Interperiodica”.

1. INTRODUCTION

As is well known, many specific properties of superlattices (SLs) manifest themselves at low temperatures at which the electron scattering by phonons is inelastic. Inelasticity of this scattering is especially important for a SL with quasi-two-dimensional (quasi-2D) electron gas as it is related to the large uncertainty of the longitudinal phonon wave vector parallel to the SL axis. In addition to the inelasticity of scattering, the nonequilibrium function of the electron distribution should significantly depend on the width of the miniband at low temperatures, which in this case becomes comparable with the energy k_0T .

There are only a few publications in which the problem of electron scattering by acoustic phonons in an SL have been considered. Notably, quasi-elastic deformation-potential scattering by acoustical phonons with regard to the dispersion of the energy spectrum of the miniband was considered by Fridman [1]. Only in one paper [2] was inelastic scattering by acoustical phonons for the transport of quasi-2D electron gas in the direction perpendicular to the SL symmetry axis considered. Studies which consider the simultaneous influence of the dispersion of the miniband energy spectrum and the inelasticity of scattering by acoustic phonons on the longitudinal and in-plane components of the electron mobility are not widely known.

In this study, the formulas for relaxation time for the transport perpendicular to the SL axis (in-plane transport) and an integral equation for the effective relaxation time for longitudinal transport (along the SL axis) have been calculated taking into account inelastic electron scattering by acoustical phonons and the dispersion of the electron energy as a function of the longitu-

dinal wave vector. Numerical analysis of the dependences of in-plane and longitudinal components of the effective momentum relaxation time on the energy dispersion in the plane of a layer (in-plane energy) and the longitudinal electron wave vector in a GaAs/Al_xGa_{1-x}As SL at $T = 77$ K was performed. A comparative analysis of longitudinal and in-plane components of the mobility, calculated using various approximations, has been carried out. It is shown that consideration of the finite width of the miniband for the acoustical phonon scattering results in a significant increase in the mobility of quasi-2D electrons in an SL at the liquid nitrogen temperature.

2. BASIC FORMULAS

It is well known that the probability of the intraminiband electron transition with the wave vector \mathbf{k} into the state with \mathbf{k}' due to the scattering by longitudinal acoustic phonons in III–V semiconductors can be expressed in a tight-binding approximation for the envelope of the electron wave function of an SL consisting of quantum wells (QWs) with infinitely high potential barriers and in an approximation of the phonon spectrum for bulk material as

$$w_{\mathbf{k}\mathbf{k}'}^{\pm} = \frac{\pi D^2}{\rho v_L V} \sum_n q_n S^2 \left(\frac{aq_{nz}}{2} \right) \times \left[N(q_n) + \frac{1}{2} \pm \frac{1}{2} \right] \delta(\varepsilon_{\mathbf{k}'} - \varepsilon_{\mathbf{k}} \pm \hbar v_L q_n), \quad (1)$$

where

$$\varepsilon_{\mathbf{k}} = \varepsilon = \varepsilon_{\perp} + \frac{\Delta}{2}(1 - \cos k_z d), \quad \varepsilon_{\perp} = \frac{\hbar^2 k_{\perp}^2}{2m_{\perp}},$$

$$\mathbf{q}_n = \mathbf{k}' - \mathbf{k} + \frac{2\pi n}{d} \mathbf{e}_z, \quad S(x) = \pi^2 x^{-1} (\pi^2 - x^2)^{-1} \sin x,$$

$$N(q) = \left[\exp\left(\frac{\hbar v_L q}{k_0 T}\right) - 1 \right]^{-1}, \quad -\frac{N_z}{2} < n < \frac{N_z}{2};$$

N_z is the number of SL periods, which is considered to be infinite; D is the deformation potential constant for longitudinal acoustical phonons; ρ is the mass density;

$v_L = \sqrt{\frac{c_L}{\rho}}$ is the velocity of longitudinal acoustic

phonons; $c_L = c_{11} + \frac{2}{5}(c_{12} + 2c_{44} - c_{11})$ is an angle-averaged elasticity modulus of longitudinal acoustical phonons; Δ is the width of the main (lower) miniband; a is the QW width; d is the SL period; and \mathbf{e}_z is the unit vector directed along the SL axis.

We write the nonequilibrium addition to the electron distribution function in the standard form; i.e.,

$$g(\mathbf{k}) = e \frac{\partial f_0}{\partial \varepsilon} \sum_i \tau_i(\mathbf{k}) E_i v_i(\mathbf{k}), \quad (2)$$

where E_i are components of the electric field strength, $\mathbf{v}(\mathbf{k}) = \nabla_{\mathbf{k}} \varepsilon / \hbar$ is the electron velocity, and $f_0(\varepsilon)$ is the equilibrium Fermi–Dirac function. We refer to $\tau_i(\mathbf{k})$ functions as the effective relaxation time by analogy with the solution of the linearized Boltzmann equation for elastic mechanisms of scattering in the approximation of the parabolic charge-carrier dispersion law.

As follows from formula (1), it is possible to ignore the transverse components of the phonon wave vector \mathbf{q}_n in comparison with the longitudinal component. In this case, the probability of scattering is an even function relative to the in-plane component of the wave vector of the final electron state \mathbf{k}'_{\perp} . This circumstance makes it possible to derive the following formula for the in-plane relaxation time as a function of both the in-plane electron energy ε_{\perp} and the component of the longitudinal wave vector k_z :

$$\tau_x^{-1} = \tau_y^{-1} = \tau_{\perp}^{-1}(\varepsilon_{\perp}, \varphi) = C_{AC} \sum_{l, m} \int_0^{\infty} x S^2(tx) \times \left[N(x) + \frac{1}{2}(1-l) + f_0(\varepsilon + lk_0 T x) \right] \theta(\varepsilon'_m) dx, \quad (3)$$

where

$$\varepsilon'_m = \varepsilon_{\perp} + \frac{\Delta}{2} [\cos \varphi_m - \cos \varphi] + lx k_0 T,$$

$$\varphi = k_z d, \quad \varphi_m = \varphi + m \frac{k_0 T d}{\hbar v_L} x, \quad t = \frac{k_0 T a}{\hbar v_L 2},$$

$$N(x) = (\exp x - 1)^{-1}, \quad C_{AC} = \frac{m_{\perp} D^2 (k_0 T)^2}{4\pi \rho \hbar^4 v_L^3},$$

$\theta(\varepsilon)$ is a theta function which is nonzero and equal to unity for a positive argument, and indices l and m take the values of +1 and -1.

According to formula (3), the transverse relaxation time is isotropic in the plane of a layer in a QW and anisotropic in the plane parallel to the SL axis. Formula (3) transforms into the formula obtained in [2] for $\Delta = 0$, in which case the electron distribution over the energy spectrum is taken into account:

$$\tau_{\perp}^{-1}(\varepsilon) = 2C_{AC} \int_0^{\infty} x S^2(tx) \{ [N(x) + f_0(\varepsilon + k_0 T x)] + [N(x) + 1 - f_0(\varepsilon - k_0 T x)] \theta(\varepsilon - k_0 T x) \} dx, \quad (4)$$

where $\varepsilon = \varepsilon_{\perp}$. The well-known expression for the isotropic and energy-independent relaxation time, which follows from formula (4) for nondegenerate electron gas, in the approximation of elastic scattering for

$$x = \frac{\hbar v_L q_z}{k_0 T} \rightarrow 0$$

is given by

$$\tau_{\perp} = \tau_{\parallel} = \tau = \frac{2}{3} \frac{a c_L \hbar^3}{m_{\perp} D^2 k_0 T}. \quad (5)$$

In the case of longitudinal electron transport, the effective relaxation time $\tau_{\parallel}(\varepsilon_{\perp}, \varphi)$ is the solution to the integral equation which follows from the linearized Boltzmann equation. Taking into account formulas (1) and (3), we can write

$$\frac{\tau_{\parallel}(\varepsilon_{\perp}, \varphi)}{\tau_{\perp}(\varepsilon_{\perp}, \varphi)} = \frac{C_{AC}}{f'_0(\varepsilon) \sin \varphi} \times \sum_{l, m} \int_0^{\infty} x S^2(tx) \left[N(x) + \frac{1}{2}(1+l) - l f_0(\varepsilon) \right] \times f'_0(\varepsilon + lk_0 T x) \tau_{\parallel}(\varepsilon'_m, \varphi_m) \theta(\varepsilon'_m) \sin \varphi_m dx + 1, \quad (6)$$

where $f'_0(\varepsilon)$ is the derivative of the equilibrium distribution function.

Taking into account formula (1) for the dispersion law of the electron energy spectrum and formula (2) for the nonequilibrium addition to the distribution func-

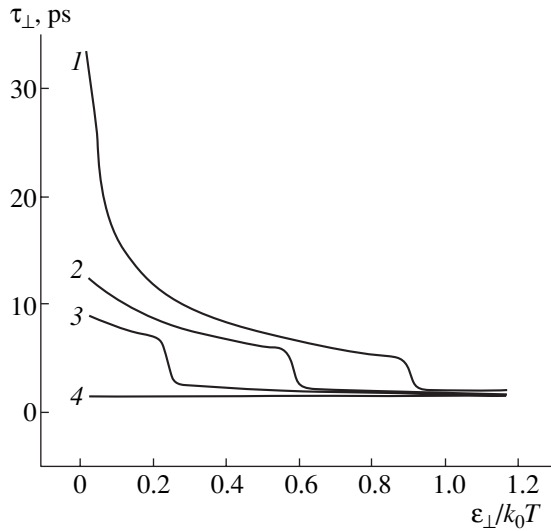


Fig. 1. The dependences of the electron-momentum relaxation time $\tau_{\perp}(\varepsilon_{\perp}, \varphi)$ on the in-plane electron energy ε_{\perp} and the angle φ : (1) 0, (2) $-\pi/4$, (3) $3\pi/8$, and (4) π .

tion, the longitudinal and in-plane electron mobilities can be expressed in a conventional way in terms of the average effective relaxation time:

$$\begin{aligned} \mu_{xx} = \mu_{yy} = \mu_{\perp} &= e \langle \tau_{\perp} \rangle / m_{\perp}, \\ \mu_{zz} = \mu_{\parallel} &= e \langle \tau_{\parallel} \rangle / \langle m_{\parallel} \rangle, \end{aligned} \quad (7)$$

where

$$\langle \tau_{\perp} \rangle = \frac{\int [-f'_0(\varepsilon)] \tau_{\perp}(\varepsilon_{\perp}, \varphi) \varepsilon_{\perp} d\varepsilon_{\perp} d\varphi}{\int f_0(\varepsilon) d\varepsilon_{\perp} d\varphi}; \quad (8)$$

$$\langle \tau_{\parallel} \rangle = \frac{\int [-f'_0(\varepsilon)] \tau_{\parallel}(\varepsilon_{\perp}, \varphi) \sin^2 \varphi d\varepsilon_{\perp} d\varphi}{\int [-f'_0(\varepsilon)] \sin^2 \varphi d\varepsilon_{\perp} d\varphi}; \quad (9)$$

$$\frac{1}{\langle m_{\parallel} \rangle} = \left(\frac{\Delta d}{2\hbar} \right)^2 \frac{\int [-f'_0(\varepsilon)] \sin^2 \varphi d\varepsilon_{\perp} d\varphi}{\int f_0(\varepsilon) d\varepsilon_{\perp} d\varphi} \quad (10)$$

is the average value of the longitudinal electron effective mass. The formulas (7)–(9) are simplified for nondegenerate electron gas. Considering that, in this case,

$$\langle \tau \rangle = \int_0^{\infty} e^{-x} \tau(x) dx \quad (11)$$

and

$$\frac{1}{\langle m_{\parallel} \rangle} = \frac{2}{k_0 T} \left(\frac{\Delta d}{2\hbar} \right)^2 \frac{\int_0^{\pi} e^{\delta \cos \varphi} \sin^2 \varphi d\varphi}{\int_0^{\pi} e^{\delta \cos \varphi} d\varphi}, \quad (12)$$

where

$$x = \varepsilon_{\perp} / k_0 T, \quad \delta = \Delta / 2k_0 T,$$

the relaxation times are given by

$$\tau_{\perp}(x) = \frac{\int_0^{\pi} e^{\delta \cos \varphi} \tau_{\perp}(x, \varphi) d\varphi}{\int_0^{\pi} e^{\delta \cos \varphi} d\varphi}, \quad (13)$$

$$\tau_{\parallel}(x) = \frac{\int_0^{\pi} e^{\delta \cos \varphi} \tau_{\parallel}(x, \varphi) \sin^2 \varphi d\varphi}{\int_0^{\pi} e^{\delta \cos \varphi} \sin^2 \varphi d\varphi}. \quad (14)$$

3. NUMERICAL ANALYSIS OF THE RESULTS OF CALCULATION

The effect of inelasticity of scattering by acoustical phonons, as well as the dispersion of the electron energy along the SL axis, on the effective momentum-relaxation time and electron mobility was studied in the GaAs/Al_{0.36}Ga_{0.64}As superlattice with nondegenerate electron gas at $T = 77$ K. A symmetrical SL with the parameters $a = 5$ nm and $d = 10$ nm was considered. The miniband width $\Delta = 7.2$ meV was calculated using the Kronig–Penney model [3]. The basic parameters of GaAs [4],

$$\begin{aligned} m_{\perp} &= 0.067 m_0, \quad \rho = 5.3 \text{ g/cm}^3, \\ c_L &= 14.4 \times 10^{10} \text{ H/m}^2, \quad D = 17.5 \text{ eV}, \end{aligned}$$

were used for the calculation of the QW parameters.

Numerical calculation of τ_{\perp} from formula (3) and τ_{\parallel} from Eq. (6), using the iteration method, showed that these functions are approximately equal at $T = 77$ K, i.e., $\tau_{\perp} \approx \tau_{\parallel}$. The dependences of $\tau_{\perp}(\varepsilon_{\perp}, \varphi)$ on the energy dispersion in the layer plane for different angles $\varphi = k_z d$ are shown in Fig. 1. According to the plots presented in Fig. 1, one can see a pronounced dispersion of the relaxation time in the region of small longitudinal wave vectors, which is caused by the dispersion of the miniband energy spectrum.

The dependences of the effective relaxation times, averaged over the angle φ , on the in-plane electron energy calculated taking the inelasticity of scattering and dispersion of the miniband energy spectrum into account are illustrated in Fig. 2. As one can see, there is a significant dispersion of $\tau_{\parallel}(x)$ and $\tau_{\perp}(x)$ for $\varepsilon_{\perp} < \Delta$, where $x = \varepsilon_{\perp} / k_0 T$, as a function of the in-plane energy. This fact is related to the difference in the averaging of these quantities according to formulas (13) and (14).

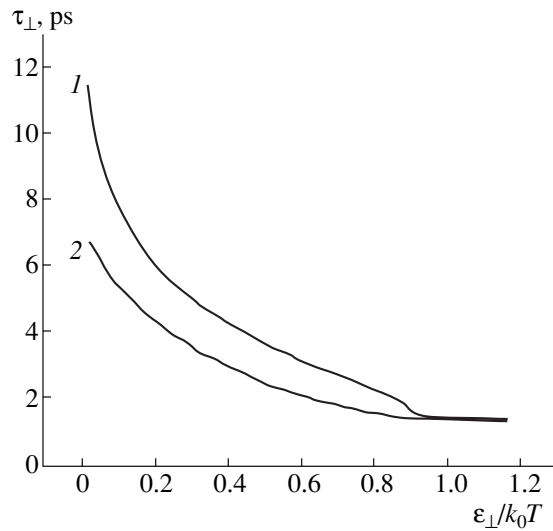


Fig. 2. The dependences of the effective electron momentum-relaxation times averaged over the angle φ on the in-plane electron energy: (1) τ_{\perp} , (2) τ_{\parallel} .

The functions $\tau_{\parallel}(x)$ and $\tau_{\perp}(x)$, which were calculated using various approximations for the angle of the inelasticity of scattering ($v_L \neq 0$) and the dispersion of the miniband energy spectrum ($\Delta \neq 0$), are shown in Fig. 3. According to these dependences, consideration of the dispersion of the miniband energy spectrum is far more important than that of the inelasticity of scattering in an SL with the above-mentioned parameters at the liquid-nitrogen temperature. The reason is that the average energy of the longitudinal acoustical phonon involved in the electron scattering $h\nu_L/d \approx 2$ meV is considerably less than the miniband width.

The values of the effective momentum-relaxation times (averaged over the wave vector) and the mobilities calculated by various approximations according to formulas (7)–(9) with the longitudinal effective mass averaged according to formula (12) $\langle m_{\parallel} \rangle = 0.81m_0$ are listed in the table. According to these data, consideration of the energy spectrum dispersion significantly

The electron mobilities and the effective momentum-relaxation times averaged over the wave vector for a GaAs/Al_{0.36}Ga_{0.64}As superlattice calculated for the acoustical phonon scattering at $T = 77$ K

Calculated quantities	Approximation			
	$\Delta = 0$ $v_L = 0$	$\Delta = 0$ $v_L \neq 0$	$\Delta \neq 0$ $v_L = 0$	$\Delta \neq 0$ $v_L \neq 0$
$\langle \tau_{\perp} \rangle$, ps	1.11	1.12	1.77	1.69
$\langle \tau_{\parallel} \rangle$, ps	1.11	1.36	2.87	2.72
μ_{\perp} , m ² /(V s)	2.93	2.95	4.64	4.45
μ_{\parallel} , m ² /(V s)	0.25	0.31	0.62	0.59

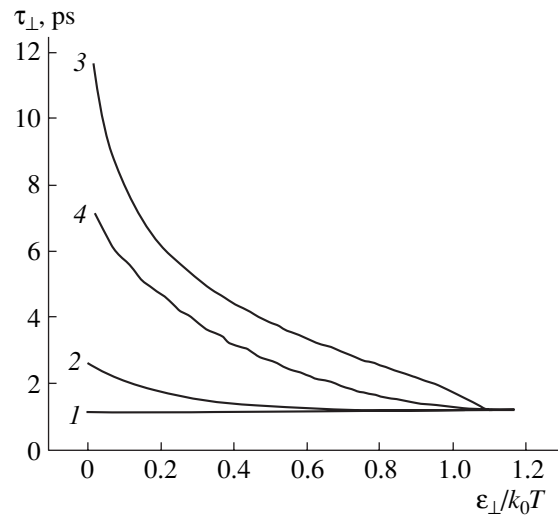


Fig. 3. The dependences of the effective electron momentum-relaxation times averaged over the angle φ on the in-plane electron energy (approximate calculations): (1) $\tau_{\perp} = \tau_{\parallel} = \text{const}$ ($\Delta = 0$, $v_L = 0$), (2) $\tau_{\perp} \approx \tau_{\parallel}$ ($\Delta = 0$, $v_L \neq 0$), (3) τ_{\perp} ($\Delta \neq 0$, $v_L = 0$), and (4) τ_{\parallel} ($\Delta \neq 0$, $v_L = 0$).

increases the mobility, whereas inelasticity of scattering can be neglected at the temperature under consideration. It should be noted that the relative increase in the longitudinal mobility due to consideration of the energy dispersion along the SL axis exceeds the increase in the in-plane mobility by a factor of 1.6.

From the preceding, one can expect that the inelasticity of the charge-carrier scattering by the acoustical phonons in a superlattice may be significant if

$$\Delta, k_0T \leq h\nu_L/d, \quad (15)$$

i. e., for quasi-2D electron gas at low temperatures. Condition (15) is satisfied in the SL under study at $T \leq 23$ K and $\Delta \leq 2$ meV.

REFERENCES

1. L. Fridman, Phys. Rev. B **32**, 955 (1985).
2. Yu. V. Ivanov, M. V. Vedernikov, and Yu. I. Ravich, Pis'ma Zh. Éksp. Teor. Fiz. **69**, 290 (1999) [JETP Lett. **69**, 317 (1999)].
3. S. I. Borisenko and G. F. Karavaev, Fiz. Tekh. Poluprovodn. (St. Petersburg) **32**, 607 (1998) [Semiconductors **32**, 544 (1998)].
4. Landolt-Börnstein: Numerical Data and Functional Relationships in Science and Technology, New Series, Ed. by O. Madelung (Springer-Verlag, Berlin, 1987), Group III, Vol. 22a.

Translated by I. Kucherenko

LOW-DIMENSIONAL
SYSTEMS

Damping of Bloch Oscillations in Quantum Dot Superlattices: A General Approach

I. A. Dmitriev and R. A. Suris

*Ioffe Physicotechnical Institute, Russian Academy of Sciences,
Politekhnikeskaya ul. 26, St. Petersburg, 194021 Russia
e-mail: dmitriev@theory.ioffe.rssi.ru Fax: 7-812-2471017
Submitted May 14, 2002; accepted for publication May 16, 2002*

Abstract—A quantum kinetic equation describing damping of the Bloch oscillations in ideal quantum-dot (QD) superlattices of various dimensionalities (1D, 2D, 3D) has been derived using the density matrix formalism. The possibility of suppressing completely single-phonon scattering by optical phonons and considerably suppressing the acoustic-phonon scattering in the QD superlattice by effectively controlling the spectrum by varying the DC electric field magnitude and orientation is demonstrated. Conditions ensuring that the only photon-scattering mechanism responsible for damping of the Bloch oscillations is scattering by acoustic phonons within transverse minibands of the Stark carrier-state ladder are obtained. © 2002 MAIK “Nauka/Interperiodica”.

1. INTRODUCTION

The experimental observation of Bloch oscillations (BO) is known to be extremely difficult because of the necessity to satisfy the very rigid conditions for the weakness of carrier scattering during the oscillation period:

$$\tau_{\text{eff}}^{-1} < f_{\text{BO}} \equiv eFa/h. \quad (1)$$

Here, τ_{eff} is the effective scattering time, and f_{BO} is the BO frequency proportional to the electric field value F and to the spatial period a in the field direction. The first observations of BO, theoretically predicted as early as 1928 in Bloch’s fundamental work [1], were made only in the early 1990s on perfect quantum well superlattices (QWSL) on the basis of III–V compounds [2, 3]. The superlattice period exceeds interatomic distances by tens, and condition (1) can be satisfied at electric field magnitudes of about a few tens of kV/cm; in this case, the BO frequency is about one terahertz [4, 5]. This explains the large practical interest of the BO phenomenon in superlattices in that it is related to the possibility of developing sources and detectors of radiation in the terahertz frequency band.

However, in both QWSL and bulk semiconductors, an unavoidable strong scattering of carriers by the lattice oscillations leading to fast damping of BOs is present at all magnitudes of the electric field. Even at very low temperatures of $T \approx 10$ K, the BO lifetime amounts to a few tens of oscillation periods [2, 3, 6–8].

In this paper, we theoretically analyze the processes leading to damping of the BO in the quantum dot superlattice (QDSL). The system under consideration is a spatially periodic array of weakly coupled identical quantum dots (QD) forming an ideal superlattice of QDs with arbitrary symmetry and dimensionalities

(1D, 2D, 3D). We show that, unlike the QWSL, the QDSL enables us to effectively suppress scattering of carriers through controlling the electronic spectrum by means of changing the direction and magnitude of the electric field.

Fast damping of BO in QWSLs based on III–V or II–VI compounds is known to be due mainly to optical phonon–assisted transitions between electronic states [7, 8]. Our study of the electron spectrum and the wave functions has indicated [10] that scattering by optical phonons in a QDSL can be completely suppressed by the proper choice of the electric field magnitude and orientation relative to the crystallographic axes. At the same time, the scattering by acoustic phonons in a QDSL must become stronger than in a QWSL, since electrons in QDs are localized in all of the three directions and the electronic density of states is enhanced considerably. In this work, we show that effective control of the QDSL spectrum by means of changing the magnitude and direction of the electric field allows us to effectively suppress scattering by acoustic phonons as well.

The conditions necessary for the intraminiband (the transverse carrier motion minibands are formed at any level of the Stark ladder of states in a QDSL placed in an electric field) scattering by acoustic phonons to be the principal scattering channel in an ideal QDSL are derived. It is far from obvious that such scattering necessarily leads to damping of BO. Therefore, in order to estimate the BO damping rate due to scattering within the transverse minibands, calculating the probabilities of transitions is not sufficient. A more rigorous and consistent theory is necessary.

The BOs in the Stark representation (a representation of carrier eigenfunctions for a QDSL at the electric

field) are, in fact, quantum beats between the Stark ladder states. BOs appear when a coherent superposition of the Stark states is created. Then BO damping results from decoherence between the Stark states due to carrier scattering; that is why the density matrix formalism is the most natural way to describe the BO damping.

A quantum kinetic equation describing BO damping has been derived in this work from a general equation for the density matrix. This theory is valid for any means of BO excitation in the isolated miniband of an ideal QDSL of any symmetry at the electric field of any given value and direction.

2. BLOCH OSCILLATIONS IN THE ABSENCE OF SCATTERING

As follows from the Bloch theorem, the superlattice (SL) electronic spectrum is a set of minibands formed due to an additional SL periodic potential modulating the conduction band bottom of the material used for growing the SL [4, 5]. Houston has shown [11] that a condition necessary in order for the miniband to be “isolated,” i.e., a condition for the absence of transitions between the minibands under the action of the dc electric field, can be written as

$$\frac{4eF\hbar^2}{mW^2a} \ll 1, \quad (2)$$

where m is the effective electron mass for the SL material, W is the energy gap between the minibands, and F is the electric field value. The electric field and the resonance integrals between the QDs are assumed to be so small that condition (2) is fulfilled and, therefore, the one-miniband approximation is valid. The miniband spectrum, being a periodic function, can always be presented in the form of a Fourier expansion over the QDSL vectors $\mathbf{R} = \sum n_i \mathbf{a}_i$, where \mathbf{a}_i are the crystallographic basis vectors of the QDSL:

$$\mathcal{E}(\mathbf{K}) = \sum_{\mathbf{R}} \frac{\Delta_{\mathbf{R}}}{4} \exp(i\mathbf{K} \cdot \mathbf{R}). \quad (3)$$

Here, \mathbf{K} is a wave vector located in the first Brillouin zone of the QDSL, and the values $\Delta_{\mathbf{R}}/4$ represent tight-binding approximation resonance integrals between the QDs separated by a QDSL lattice vector \mathbf{R} . The resonance integral magnitude $\Delta_{\mathbf{R}}/4$ exponentially decreases as the distance $|\mathbf{R}|$ between the QDs increases [10].

Bloch oscillations appear in such a system after an electric field is switched on instantaneously in the absence of scattering. Here, we present two equivalent ways of describing them, and these will be used below.

2.1. Bloch Oscillations in the Houston Representation

The Houston representation is the most natural way to describe Bloch oscillations that appear in a periodic

potential after the instantaneous switching on of the field in the absence of scattering and transitions between the allowed bands for carriers. Let us designate as $\Psi_{\mathbf{K}}(\mathbf{r})$ the Bloch functions of the chosen miniband described by the Hamiltonian $\hat{H}_0(\hbar\hat{\mathbf{K}}, \mathbf{r})$. It is convenient to expand the Bloch wave functions in the Fourier series

$$\Psi_{\mathbf{K}}(\mathbf{r}) = \sum_{\mathbf{R}} \phi(\mathbf{r} - \mathbf{R}) \exp(i\mathbf{K} \cdot \mathbf{R}), \quad (4)$$

where $\phi(\mathbf{r})$ is the Wannier function [12, 13], which is defined by the relation

$$\phi(\mathbf{r}) = \frac{1}{\sqrt{\mathcal{N}}} \sum_{\mathbf{K}} \Psi_{\mathbf{K}}(\mathbf{r}) \quad (5)$$

(\mathcal{N} is the number of QDSL sites in the normalization volume) and coincides with the electronic wave function in an isolated QD.

Let the electric field \mathbf{F} be switched on at the time $t = 0$; we introduce it into the Hamiltonian via the vector potential

$$\hat{H}_F \equiv \hat{H}_0\left(\hbar\hat{\mathbf{K}} - \frac{e}{c}\mathbf{A}, \mathbf{r}\right) = \hat{H}_0(\hbar\hat{\mathbf{K}} + e\mathbf{F}t, \mathbf{r}). \quad (6)$$

Houston has shown [11] that, for an isolated miniband (2), the following functions are the solutions to the time-dependent Schrödinger equation with the Hamiltonian \hat{H}_F :

$$\begin{aligned} \Phi_{\mathbf{K}}(\mathbf{r}, t) &= \Psi_{\mathbf{K}(t)}(\mathbf{r}) \exp\left\{-\frac{i}{\hbar} \int_0^t \mathcal{E}[\mathbf{K}(\tau)] d\tau\right\} \\ &= \sum_{\mathbf{R}} \phi(\mathbf{r} - \mathbf{R}) e^{i(\mathbf{K} \cdot \mathbf{R} + \Omega_{\mathbf{R}} t)} \\ &\times \exp\left\{-\frac{i}{\hbar} \int_0^t \sum_{\mathbf{R}'} \frac{\Delta_{\mathbf{R}'}}{4} e^{i(\mathbf{K} \cdot \mathbf{R}' + \Omega_{\mathbf{R}'} \tau)} d\tau\right\}. \end{aligned} \quad (7)$$

The electron moves in the \mathbf{K} space at a constant velocity which is determined by the electric field, $\hbar\mathbf{K}(t) = \hbar\mathbf{K} + e\mathbf{F}t$, and undergoes Bragg reflections at the Brillouin zone boundary of the QDSL. The electron motion is a superposition of oscillations with several fundamental frequencies $\Omega_{\mathbf{R}} \equiv (e/\hbar)(\mathbf{F} \cdot \mathbf{R}) = (e/\hbar) \sum n_i (\mathbf{F} \cdot \mathbf{a}_i) = \sum n_i \Omega_i$. Such motion is periodic if all ratios Ω_i/Ω_k are rational and is quasi-periodic if at least one of these ratios is irrational (since one can always approximate it by the nearest rational number).

The electronic oscillations are accompanied by oscillations of the current. In the case when the electric field is instantaneously switched on, the electrons are initially distributed over the Bloch states of a miniband

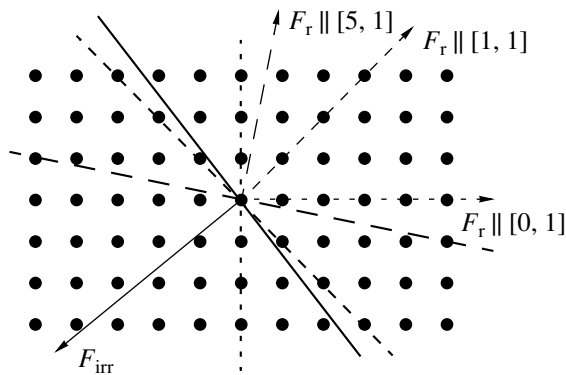


Fig. 1. Rational (F_r) and irrational (F_{irr}) field directions in a 2D QDSL.

in accordance with the equilibrium distribution function. In this case, the current $\mathbf{j}(t)$ is uniformly distributed and can be accurately described within a quasi-classical approximation. Applying the equations of classical dynamics

$$\hbar \mathbf{v}(\mathbf{K}) = \nabla_{\mathbf{K}} \mathcal{E}(\mathbf{K}), \quad \frac{\partial}{\partial t}(\hbar \mathbf{K}) = e\mathbf{F}, \quad (8)$$

and taking (3) into account, we obtain

$$\begin{aligned} \mathbf{j}(t) &= en_e \int d\mathbf{K} \mathbf{v}(\mathbf{K} + e\mathbf{F}t/\hbar) f(\mathbf{K}) \\ &= \sum_{\mathbf{R}} \frac{en_e \Delta_{\mathbf{R}} \mathbf{R}}{2\hbar} \langle \cos(\mathbf{K} \cdot \mathbf{R}) \rangle \sin(\Omega_{\mathbf{R}} t), \end{aligned} \quad (9)$$

where n_e is the electron density, $f(\mathbf{K})$ is the initial electron distribution function normalized to a single electron, and \mathbf{v} is the electron group velocity; the angle brackets denote averaging with the distribution function.

From (7) and (9), one can see the considerable advantage of using the Bloch oscillations over SLs formed from QWs for practical applications. Oscillations in a QWSL occur at one frequency $\Omega = eFa/\hbar$, where a is the SL period and F is the electric field component along the axis of the QWSL. The QDSL oscillation spectrum contains two (2D QDSL) or three (3D QDSL) fundamental frequencies Ω_i [14] (resonance integrals $\Delta_{\mathbf{R}}/4$ exponentially decrease as the distance between the QWs $|\mathbf{R}|$ increases; therefore, amplitudes of other harmonics are exponentially small in comparison with the basic ones). Changing the electric field direction relative to the QDSL basis vectors and its magnitude, we can change the fundamental frequencies independently.

2.2. Stark Electron States in QD Superlattices

Another way to describe the BOs is based on the Stark representation of the QDSL Hamiltonian \hat{H}_F eigenfunctions at the dc electric field [10]. Here, we

present the main results [10] necessary for further analysis. Let us seek the wave functions in the form of an expansion in Wannier functions (5):

$$\Psi(\mathbf{r}) = \sum_{\boldsymbol{\rho}} C_{\boldsymbol{\rho}} \phi(\mathbf{r} - \boldsymbol{\rho}), \quad (10)$$

where $\boldsymbol{\rho}$ are the QDSL vectors. Then, the equation for the coefficients $C_{\boldsymbol{\rho}}$ reads

$$(E + e\mathbf{F} \cdot \boldsymbol{\rho}) C_{\boldsymbol{\rho}} - \sum_{\boldsymbol{\rho}_1} \Delta_{\boldsymbol{\rho} - \boldsymbol{\rho}_1} C_{\boldsymbol{\rho}_1} = 0. \quad (11)$$

The solutions to (11) are different for the two classes of electric field orientations relative to the QDSL basis vectors.

If all ratios of the electric field components along the QDSL basis vectors $(\mathbf{F} \cdot \mathbf{a}_i)/(\mathbf{F} \cdot \mathbf{a}_k) = \Omega_i/\Omega_k$ are irrational numbers (irrational field directions), the electric potentials of all QDSL sites are different (Fig. 1). The spectrum is discrete and forms a 1D, 2D, or 3D Stark ladder, depending on the QDSL dimensionality:

$$E_{\mathbf{R}} = -e\mathbf{F} \cdot \mathbf{R} = -\sum_i n_i \hbar \Omega_i. \quad (12)$$

The electron in such states is localized in all directions.

If at least one of the ratios Ω_i/Ω_k becomes rational (rational field directions), chains (or planes) of QDs are formed in the direction perpendicular to the field whose electric potential is the same (Fig. 1). Lifting of the degeneracy given by (12) for such field orientations is shown in [10] to be possible only when resonance integrals that couple QDs in the transverse chains (planes) are taken into account. Then, a transverse miniband is formed at each step of the Stark ladder and the spectrum takes the form

$$E_{\mathbf{R}}(K_{\perp}) = -e\mathbf{F} \cdot \mathbf{R} + \sum_{\boldsymbol{\rho} \perp \mathbf{F}} \frac{\Delta_{\boldsymbol{\rho}}}{4} \cos(\mathbf{K} \cdot \boldsymbol{\rho}). \quad (13)$$

Since the distances between QDs in the transverse chains (planes) are different for different rational field directions (Fig. 1) and the resonance integrals exponentially decrease with increasing distance between QDs, the transverse miniband width in (13) exponentially depends on the field direction as well (Fig. 2). A general exact expression for the spectrum (13) that takes into consideration the exponential dependence of the resonance integral on the distance between QDs for every rational field direction can be presented in the form

$$\epsilon_N^k = -N\hbar\Omega + \frac{\Delta_{\perp}}{2} \cos(ka_{\perp}), \quad (14)$$

where a $\mathbf{k} \equiv \mathbf{K}_{\perp}$ notation, used in what follows, is introduced for the transverse motion wave vector; $\Omega = eFa_{\parallel}/\hbar$ is the minimum Stark frequency related to the electrostatic potential difference between the neighboring transverse chains of QDs (Fig. 1) (all other eigenfrequencies are whole multiples of Ω); a_{\parallel} is the distance between the transverse chains [it is noteworthy that it

does not coincide with the QDSL period in the electric field direction (Fig. 1)]; a_{\perp} is the distance between QDs in the transverse chains; and $\Delta_{\perp}/4$ are resonance integrals between the nearest QDs in the chain, so that Δ_{\perp} is the transverse miniband width.

In addition, the electronic wave functions in the states (13) were found in [10] for an arbitrary electric field orientation in the form of an expansion (10) in Wannier functions (5), $|\boldsymbol{\rho}\rangle = \phi(\mathbf{r} - \boldsymbol{\rho})$. In the case of rational field directions (14),

$$\hat{H}_F|N, k\rangle = \hat{H}_F \sum \exp(i\mathbf{k} \cdot \boldsymbol{\rho}) C_{\boldsymbol{\rho}}^{N, k} |\boldsymbol{\rho}\rangle = \hbar \varepsilon_N^k |N, k\rangle. \quad (15)$$

Here, we shall not present general expressions for the coefficients $C_{\boldsymbol{\rho}}^{N, k}$, which are rather complicated, but expressions will be given for the case where the electric field \mathbf{F} is directed along one of the principal axes of the rectangular 2D QDSL. The tight-binding approximation is valid for the description of a QDSL in this case; the spectrum and the eigenfunctions of \hat{H}_F read [10]

$$\hat{H}_F|N, k\rangle = \hat{H}_F \sum C_{n_{\parallel}, n_{\perp}}^{N, k} |n_{\parallel}, n_{\perp}\rangle = \hbar \varepsilon_N^k |N, k\rangle, \quad (16)$$

$$\hbar \varepsilon_N^k = -N\hbar\Omega + \Delta_{\perp}/2 \cos(ka_{\perp}),$$

$$C_{\boldsymbol{\rho}}^{N, k} = e^{ika_{\perp}n_{\perp}} J_{n_{\parallel}-N} \left(\frac{\Delta_{\parallel}}{2\hbar\Omega} \right).$$

Hereinafter, all values related to the electric field direction have the index \parallel , while the values related to the transverse motion direction have the index \perp ; $|n_{\parallel}, n_{\perp}\rangle = |\boldsymbol{\rho}\rangle = \phi(\mathbf{r} - \boldsymbol{\rho})$ are the Wannier functions of the miniband under consideration (5) and are centered at the QDSL sites with the coordinates $\boldsymbol{\rho} = n_{\parallel}a_{\parallel} + n_{\perp}a_{\perp}$, where a_{\parallel} and a_{\perp} are, respectively, the QDSL periods in the longitudinal and transverse directions relative to the electric field; k is the wave vector magnitude for the electron motion in the chain (perpendicular to the field direction) of QDs in the 2D QDSL; $\Omega = eFa_{\parallel}/\hbar$ is the Stark frequency; $\Delta_{\perp}/4$ is the resonance integral between neighboring QDs in transverse chains and determines the transverse miniband width; $\Delta_{\parallel}/4$ is the resonance integral between neighboring QDs in the field direction; and J_n is a Bessel function of the first kind.

The single essential distinction of (16) from the spectrum and wave functions of the Stark ladder in a QWSL is the narrowness of the transverse minibands, which are formed here due to the resonance tunneling of electrons in the transverse QD chains. Similarly to a QWSL, the electron localization length L_{loc} at the electric field is determined by the ratio of the resonance integral in the field direction and the electric potential difference between the nearest QDs, $\lambda = \Delta_{\parallel}/\hbar\Omega$: at $\lambda \gg 1$, $L_{\text{loc}} = \lambda a_{\parallel}$; if $\lambda \ll 1$, the electron is localized mainly within a single QD perpendicular to the electric field and the wave function amplitude at the neighboring chains is then proportional to λ .

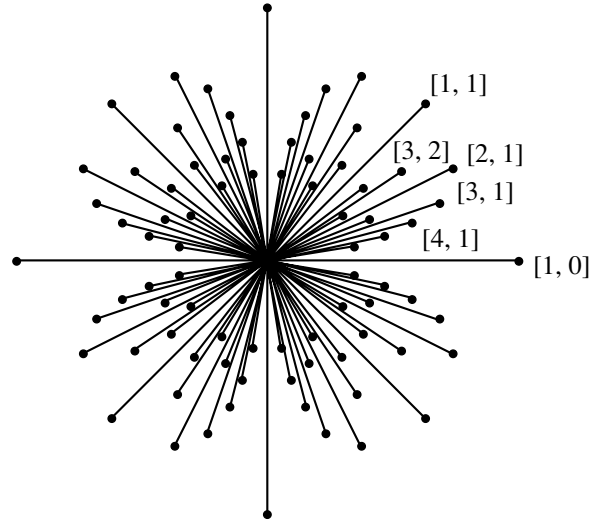


Fig. 2. Dependence of the transverse-miniband width on the electric field orientation relative to the 2D QDSL crystallographic axes (the ray lengths indicate the transverse miniband widths on the logarithmic scale for a given electric field direction).

2.3. Bloch Oscillations in the Stark Representation

Using the solution to the time-independent Schrödinger equation (16), we can easily consider the electron dynamics under various initial conditions in the absence of scattering. We shall demonstrate later on that, in this representation, the Bloch oscillations are quantum beats between the Stark ladder states.

Let the initial electron wave function form a coherent superposition of the Stark states (16):

$$\Psi(t=0) = \sum \chi_{N, k}^0 |N, k\rangle. \quad (17)$$

The time evolution of the Stark states (16) is known, and we can write a solution to the time-dependent Schrödinger equation in the form

$$\Psi(t) = \sum \chi_{N, k}^0 \exp\left(-\frac{i}{\hbar} \varepsilon_N^k t\right) |N, k\rangle = \sum_{\boldsymbol{\rho}} \xi_{\boldsymbol{\rho}}(t) |\boldsymbol{\rho}\rangle, \quad (18)$$

$$\xi_{\boldsymbol{\rho}}(t) = \sum_{N, k} \chi_{N, k}^0 \exp\left(-\frac{i}{\hbar} \varepsilon_N^k t\right) C_{\boldsymbol{\rho}}^{N, k}.$$

In particular, if the initial conditions can be factorized, $\chi_{N, k}^0 = \alpha_N \beta_k$, we can obtain

$$w_n = \sum_{n_{\perp}} |\xi_{n, n_{\perp}}|^2 = \sum_{N, N'} \alpha_N \alpha_{N'}^* J_{n-N} \left(\frac{\Delta_{\parallel}}{2\hbar\Omega} \right) \times J_{n-N'} \left(\frac{\Delta_{\parallel}}{2\hbar\Omega} \right) \exp[i(N-N')\Omega t] \quad (19)$$

for the probability of finding an electron in the layer with number n .

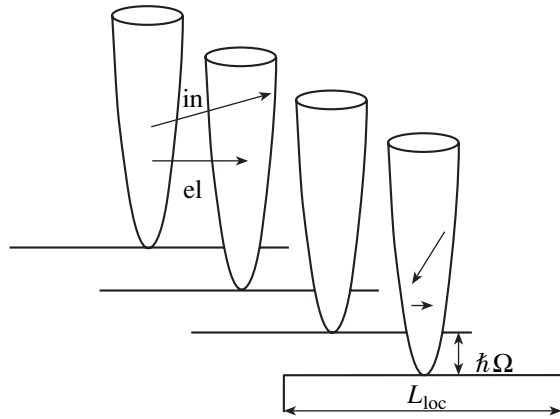


Fig. 3. QWSL spectrum in an electric field. Channels of inelastic (in) and elastic (el) scattering in the QWSL are indicated.

From this it is seen that the electron density oscillates in each QD with the Stark frequency as a result of the quantum beats. The electronic oscillations are accompanied by current oscillations in the field direction

$$j_n = \sum_{n_\perp} \frac{en_e \Delta_{\parallel} a_{\parallel}}{\hbar} \text{Im} \{ \xi_{n+1, n_\perp}^*(t) \xi_{n, n_\perp}(t) \}. \quad (20)$$

Let us consider a few of the ways in which the coherent superposition of the Stark states can be created.

2.3.1. Instantaneous switching-on of a field. When the electric field is instantaneously switched on, electrons are initially distributed in equilibrium over the Bloch states of the QDSL miniband. The function $\chi_N^0 = \exp(iN\mathbf{K}_{\parallel}^0 \mathbf{a}_{\parallel}) \delta_{\mathbf{k}, \mathbf{K}_{\perp}^0}$ corresponds in the Stark representation to the Bloch state with the wave vector \mathbf{K}^0 . Summing in expression (20) for the current with subsequent averaging over the initial wave vectors with the distribution function gives

$$j = \frac{en_e \Delta_{\parallel} a_{\parallel}}{2\hbar} \langle \cos K_{\parallel}^0 a_{\parallel} \rangle \sin(\Omega t), \quad (21)$$

which coincides with the earlier result obtained in (9) within the quasi-classical approximation for an arbitrary electric field.

2.3.2. Instantaneous drop of field. Let the electron be localized initially in the plane $\mathbf{p} \cdot \mathbf{F} = 0$, which may occur at a very high field $eFa_{\parallel} \gg \Delta_{\perp}$. Then $\chi_{N, k}^0 = J_N(\Delta_{\parallel}/2\hbar\Omega) \beta_k$ (as we determined in (19), the dependence on the transverse wave vector is not important in

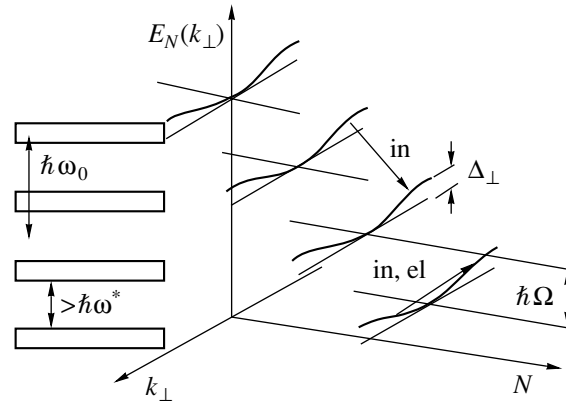


Fig. 4. Two-dimensional QDSL spectrum in an electric field. Channels of inelastic (in) and elastic (el) scattering in the 2D QDSL are indicated.

the case of factorized initial conditions) and the so-called “breathing” mode is formed:

$$j_n = \frac{en_e \Delta_{\parallel} a_{\parallel}}{\hbar} \cos(\Omega t/2) J_n \left[\frac{\Delta_{\parallel}}{\hbar\Omega} \sin(\Omega t/2) \right] \times J_{n+1} \left[\frac{\Delta_{\parallel}}{\hbar\Omega} \sin(\Omega t/2) \right]. \quad (22)$$

The current is antisymmetric in this case: $j_n = -j_{-n-1}$, the electron density centroid remains in the plane $\mathbf{p} \cdot \mathbf{F} = 0$, and a dipole moment is absent. After spreading over the localization region $L_{\text{loc}} = a_{\parallel}(\Delta_{\parallel}/\hbar\Omega)$, the electron becomes localized again after a time $T = 2\pi/\Omega$ in the plane $\mathbf{p} \cdot \mathbf{F} = 0$.

3. SCATTERING CHANNELS IN QD AND LAYERED SUPERLATTICES

Let us compare the possibility of suppressing scattering in layered SLs and QDSLs. It is seen from Fig. 3 that in the QD superlattices scattering remains strong at any electric field value owing to the wide transverse spectrum at any electric field magnitude. An energy overlap of states on different steps of the Stark ladder makes both elastic scattering and that assisted by optical and acoustic phonons possible.

The situation fundamentally changes in QD superlattices. Here, there exists a possibility of changing the transverse miniband width by varying the electric field orientation relative to the QDSL axes and, thus, of controlling the QDSL spectrum at the electric field and, therefore, the scattering.

In actuality, it is seen from Fig. 4 that single-phonon scattering processes involving the optical phonons within the transverse miniband are impossible if the transverse miniband width Δ_{\perp} becomes less than the optical phonon energy:

$$\Delta_{\perp} < \hbar\omega_0. \quad (23)$$

Let the transverse minibands now be energetically nonoverlapping and the condition

$$n\Omega + \frac{\Delta_{\perp}}{2\hbar} < \omega_0 < (n+1)\Omega - \frac{\Delta_{\perp}}{2\hbar} \quad (24)$$

be fulfilled for all natural numbers n . Here, $\hbar\Omega = eFa_{\parallel}$ is the distance between neighboring Stark ladder steps, and Δ_{\perp} is the transverse miniband width. Then, inter-miniband single-phonon scattering by optical phonons is completely suppressed as well (Fig. 4).

Moreover, inter-miniband scattering processes assisted by acoustic phonons can also be suppressed to any extent desired. Certain features of the interaction with acoustic phonons in a QDSL must be considered in order to ensure this.

3.1. Interaction with Acoustic Phonons in QD Superlattices

The Hamiltonian taking the deformation interaction with acoustic phonons into account reads

$$\begin{aligned} \hat{H} = & \hat{H}_0 - e\mathbf{F} \cdot \mathbf{r} + \sum_q \hbar\omega_q b_q^+ b_q \\ & + i \sum_q A_q (b_q e^{i\mathbf{q} \cdot \mathbf{r}} - b_q^+ e^{-i\mathbf{q} \cdot \mathbf{r}}), \end{aligned} \quad (25)$$

where b_q^+ and b_q are the creation and annihilation operators of a phonon with a wave vector \mathbf{q} ; $\mathbf{A}_q = \mathbf{q}G\sqrt{\hbar/2\omega_q v_0 \rho_a}$, where G is the deformation potential constant; and v_0 and ρ_a are the unit cell volume and the mass density of the SL material, respectively. For simplicity, we consider an interaction with the bulk longitudinal deformation oscillations of the QDSL material; i.e., we disregard the effect of differences in the materials inside and outside the QD on the phonon spectrum. That is why it is convenient to use the phonon wave vectors defined within the Brillouin zone of the QDSL material. Thus, $\omega_q = sq$, $q < 2\pi/a_0$ within the linear isotropic spectrum approximation (Debye model), where s and a_0 are the speed of sound and the lattice constant of the QDSL material, respectively.

Matrix elements of the electron-phonon interaction in the Stark representation $|N, k\rangle$ for the electrons (15) and the occupation number representation $\{|v_q\rangle\}$ for phonons read

$$\begin{aligned} \langle N, k; 0_q | \hat{V}_{e-ph} | N', k', 1_q \rangle &= V_{Nk, N'k'}^{01} \\ &= V_{N-N'}^q \exp\left[\frac{iq_{\parallel} a_{\parallel}}{2}(N+N')\right] \sum_l \delta_{k', k+q_{\perp}+2\pi l/a_{\perp}}, \quad (26) \\ V_{N-N'}^q &= i\mathbf{A}_q Q(q) \\ &\times \sum_{\rho} C_{\rho}^{N, k} \exp\left\{iq_{\parallel} \left(\rho_{\parallel} - a_{\parallel} \frac{N+N'}{2}\right)\right\} C_{\rho}^{N', k}, \end{aligned}$$

where summation over l takes the Umklapp processes in the transverse minibands into account, and

$$Q(q) \equiv \int d\mathbf{r} |\phi(\mathbf{r})|^2 e^{i\mathbf{q} \cdot \mathbf{r}} \quad (27)$$

is the form factor describing the fine structure of the wave functions (15) constructed from the Wannier functions of the QDSL miniband $|\rho\rangle = \phi(\mathbf{r} - \rho)$ (5). Calculation of $V_{N-N'}^q$ in the case where the electric field is directed along the 2D rectangular QDSL basis vector gives

$$V_{N-N'}^q = i\mathbf{A}_q Q(q) (-i)^{N'-N} J_{N'-N} \left(\frac{\Delta_{\parallel}}{\hbar\Omega} \sin \frac{q_{\parallel} q_{\parallel}}{2} \right). \quad (28)$$

Let us calculate the integral

$$\begin{aligned} \langle \rho | e^{i\mathbf{q} \cdot \mathbf{r}} | \rho' \rangle &= \int d\mathbf{r} \phi^*(\mathbf{r} - \rho) e^{i\mathbf{q} \cdot \mathbf{r}} \phi(\mathbf{r} - \rho') \\ &= e^{i\mathbf{q} \cdot \rho} \int d\mathbf{r}' \phi^*(\mathbf{r}') e^{i\mathbf{q} \cdot \mathbf{r}'} \phi(\mathbf{r} - \rho' - \rho), \end{aligned} \quad (29)$$

which is necessary in order to obtain the form factor $Q(q)$. The tight-binding Wannier functions related to different QDSL sites weakly overlap, and the diagonal elements (29) are essentially larger than the off-diagonal ones. In actuality, when there are small phonon wave vectors $q \ll q^* = \pi/R_D$, where R_D is the QD size, orthonormality yields $\langle \rho | e^{i\mathbf{q} \cdot \mathbf{r}} | \rho' \rangle \approx e^{e\mathbf{q} \cdot \rho} \delta_{\rho, \rho'}$ and the integral (29) rapidly decreases with q at $q \gg q^*$, while the off-diagonal elements $\rho \neq \rho'$ additionally contain the tunneling-small parameter. Thus,

$$\langle \rho | e^{i\mathbf{q} \cdot \mathbf{r}} | \rho' \rangle \approx e^{i\mathbf{q} \cdot \rho} \delta_{\rho, \rho'} Q(q), \quad (30)$$

$$Q(q) = \int d\mathbf{r} |\phi(\mathbf{r})|^2 e^{i\mathbf{q} \cdot \mathbf{r}} \approx \begin{cases} 1, & q \ll q^*, \\ (q/q^*)^{-\beta}, & q \gg q^*. \end{cases}$$

For instance, the $Q(q)$ dependence can be calculated analytically for a spherical QD of radius R_D with infinitely high walls and has the form

$$\begin{aligned} Q(q) &= \frac{\text{Si}(\pi q/q^*) - (1/2)[\text{Si}(\pi q/q^* - 2\pi) + \text{Si}(\pi q/q^* + 2\pi)]}{\pi q/q^*}, \\ Q(q/q^* > 1) &\approx \frac{8 \cos(\pi q/q^*)}{\pi^2 (q/q^*)^4}, \end{aligned} \quad (31)$$

where $\text{Si}(x) = \int_0^x [\sin(y)/y] dy$ is the integral sine.

In the case of a spherical well with finite walls and equal effective masses inside and outside the QD,

$$Q(q/q^* > 1) \approx \left[\left(\frac{2R_D}{\pi} \right)^3 |\phi(R_D)|^2 \frac{2mR_D^2 U_0}{\hbar^2} \right] \frac{\cos^2(\pi q/q^*)}{(q/q^*)^4}, \quad (32)$$

where U_0 is the QD potential well depth, and m is the effective electron mass of the QDSL material.

One can show for the general case of a QD with an arbitrary shape that the exponent in (30) $\beta = 4$ if $|\phi(\mathbf{r})|^2$ exponentially falls outside the QD and has no first derivative discontinuity. If the effective electron masses are different inside and outside the QD and a first derivative discontinuity appears, oscillations induced by it yield $\beta = 3$.

Such a rapid decrease of the form factor with increasing phonon wave vector allows us to suppress significantly the scattering by acoustic phonons between the transverse minibands of the Stark ladder (Fig. 4). In actuality, it follows from (30) that if the energy gap between the transverse minibands exceeds the actual acoustic phonon energy $\hbar\omega^* \equiv \hbar s\pi/R_D$, which is determined by the form factor

$$\hbar\Omega - \Delta_{\perp} > \hbar\omega^*, \quad (33)$$

then the probability of an acoustic-phonon-assisted transition between the minibands, which is proportional to $Q^2(q)$, falls as $(\hbar\Omega - \Delta_{\perp})^{-2\beta}$, $\beta \geq 3$.

When conditions (23), (24), and (33) are satisfied, acoustic-phonon scattering within the transverse minibands becomes the dominant scattering channel. Generally speaking, it is not apparent that such scattering leads to the damping of oscillations, since BOs occur along the electric field direction, while only the transverse momentum of carriers is scattered. That is why it does not suffice to calculate transition probabilities in order to estimate the BO damping rate due to the scattering within the miniband: a more rigorous and consistent theory is necessary. Since BOs can be regarded in the Stark representation as quantum beats between the Stark ladder states, the BO damping is, in this representation, a consequence of the decoherence between these states due to electron transitions with the emission of a photon or phonon. Then a natural way to describe the BO damping is to use the formalism of the density matrix whose off-diagonal elements describe the degree of coherence of the states.

4. QUANTUM RELAXATION EQUATION

In deriving the quantum relaxation equation, we follow the procedure developed by Kohn and Luttinger [15], which was then applied to the analysis of the carrier kinetics in layered SLs [16–19]. We assume that the effective BO damping time significantly exceeds the oscillation period:

$$\tau_{\text{eff}} \gg \Omega^{-1}. \quad (34)$$

Let us demonstrate how this condition allows us to derive the quantum relaxation equation. After the Laplace transform, the equation for the density matrix (DM) for the system with the Hamiltonian (25)

$$i\hbar \frac{d\hat{\rho}}{dt} = [\hat{H}, \hat{\rho}], \quad (35)$$

written in the Stark representation (15) for electrons $|Nk\rangle$ and the occupation number representation for phonons $|\{\eta_q\}\rangle$, takes the form

$$\begin{aligned} & i\hbar \left[s + i \sum_q \omega_q (\eta_q - \eta'_q) + i\Delta\varepsilon_{NN'}^{kk'} \right] \rho \{ Nk\eta_q | N'k'\eta'_q \} \\ & = V_{Nk, N_1k_1}^{\eta_q, \eta_q \pm 1} \rho \{ N_1k_1, \eta_q \pm 1 | N'k', \eta'_q \} \\ & + \rho \{ Nk, \eta_q | N_1k_1, \eta'_q \pm 1 \} V_{N_1k_1, N'k'}^{\eta_q \pm 1, \eta'_q} \\ & + \rho \{ Nk, \eta_q | N'k', \eta'_q \} \Big|_{t=0}, \end{aligned} \quad (36)$$

where s is the Laplace transform variable; $\Delta\varepsilon_{NN'}^{kk'} = \varepsilon_N^k - \varepsilon_{N'}^{k'}$ (15); and, on the right-hand side of the equation, summing over the intermediate indices and phonon wave vectors, as well as summing of terms with “+” and “-” signs, is assumed.

This equation relates the DM elements with the phonon occupation numbers differing by unity. Let us substitute expressions for the DM off-diagonal elements into the right-hand side of the equation for diagonal elements. Only the DM elements that are diagonal in phonon occupation numbers and whose occupation numbers differ by 2 remain after this. Terms related to a change of the phonon number by 2 must be dropped if we take into account only single-phonon processes [18, 19]. This gives

$$\begin{aligned} & i\hbar^2 [s + i\Delta\varepsilon_{NN'}^{kk'}] \rho \{ Nk, \eta_q | N'k', \eta_q \} \\ & - \rho \{ Nk, \eta_q | N'k', \eta_q \} \Big|_{t=0} \\ & = \frac{V_{Nk, N_1k_1}^{\eta_q, \eta_q \pm 1} (V_{N_1k_1, N_2k_2}^{\eta_q \pm 1, \eta_q}) \rho \{ N_2k_2, \eta_q | N'k', \eta_q \}}{is - \Delta\varepsilon_{N_1N'}^{k_1k'} \mp \omega_q} \\ & - \frac{\rho \{ N_1k_1, \eta_q \pm 1 | N_2k_2, \eta_q \pm 1 \} V_{N_2k_2, N'k'}^{\eta_q \pm 1, \eta_q}}{is - \Delta\varepsilon_{N_1N'}^{k_1k'} \mp \omega_q} \\ & - \frac{(V_{Nk, N_1k_1}^{\eta_q, \eta_q \pm 1} \rho \{ N_1k_1, \eta_q \pm 1 | N_2k_2, \eta_q \pm 1 \})}{is - \Delta\varepsilon_{NN_2}^{kk_2} \pm \omega_q} \\ & - \frac{\rho \{ Nk, \eta_q | N_1k_1, \eta_q \} V_{N_1k_1, N_2k_2}^{\eta_q, \eta_q \pm 1} V_{N_2k_2, N'k'}^{\eta_q \pm 1, \eta_q}}{is - \Delta\varepsilon_{NN_2}^{kk_2} \pm \omega_q}. \end{aligned} \quad (37)$$

Then, assuming the thermalization rate of the phonon subsystem to be higher than the collision frequency $\rho \{ Nk, \eta_q | N'k', \eta_q \} = Z^{-1} \prod_q e^{-\eta_q \hbar \omega_q / T} \rho_{NN'}^{kk'}$ and averaging the equation over the phonon degrees of

freedom, we obtain the following equation for the reduced DM:

$$\begin{aligned}
& i\hbar^2 [s + i\Omega(N - N')] \rho_{NN'}^{kk} - \rho_{NN'}^{kk} \Big|_{t=0} \\
& = [(\mathbf{v}_q + 1) V_{Nk, N_1k}^{01} V_{N_1k', N_2k}^{10} \rho_{N_2k'}^{kk} \\
& - \mathbf{v}_q V_{Nk, N_1k}^{01} \rho_{N_1N_2}^{k'k'} V_{N_2k', N'k}^{10} (is - \Delta\varepsilon_{N_1N'}^{k'k} - \omega_q)^{-1} \\
& + [\mathbf{v}_q V_{Nk, N_1k}^{10} V_{N_1k', N_2k}^{01} \rho_{N_2N'}^{kk} - (\mathbf{v}_q + 1) \\
& \times V_{Nk, N_1k}^{10} \rho_{N_1N_2}^{k'k'} V_{N_2k', N'k}^{01} (is - \Delta\varepsilon_{N_1N'}^{k'k} + \omega_q)^{-1} \quad (38) \\
& - [\mathbf{v}_q V_{Nk, N_1k}^{01} \rho_{N_1N_2}^{k'k'} V_{N_2k', N'k}^{10} - (\mathbf{v}_q + 1) \\
& \times \rho_{NN_1}^{kk} V_{N_1k, N_2k}^{01} V_{N_2k', N'k}^{10} (is - \Delta\varepsilon_{NN_2}^{kk'} + \omega_q)^{-1} \\
& - [(\mathbf{v}_q + 1) V_{Nk, N_1k}^{10} \rho_{N_1N_2}^{k'k'} V_{N_2k', N'k}^{01} \\
& - \mathbf{v}_q \rho_{NN_1}^{kk} V_{N_1k, N_2k}^{10} V_{N_2k', N'k}^{01} (is - \Delta\varepsilon_{NN_2}^{kk'} - \omega_q)^{-1},
\end{aligned}$$

where $\mathbf{v}_q = (e^{\hbar\omega_q/T} - 1)^{-1}$. We have also neglected on the right-hand side of this equation the DM elements that are off-diagonal in transverse momenta; these elements are significantly less diagonal than in the case of weak scattering [15].

In the absence of scattering, $\rho_{NN'}^{kk} = \rho_{NN'}^{kk} \Big|_{t=0} \exp[-i(N - N')\Omega t]$ is a solution to (38). In the weak scattering case $\tau_{\text{eff}}^{-1} \ll \Omega$, the singularities of $\rho_{NN'}^{kk}$ are located near the pole $s = -i\Omega(N - N')$. Therefore, only the terms with DM elements of the form $\rho_{N+n, N'+n}^{kk}$ are important on the right-hand side. If, in addition, τ_{eff}^{-1} is less than the actual phonon frequencies, we can pass to the limit $s + i\Omega(N - N') \rightarrow 0$ on the right-hand side of (38):

$$\frac{1}{is - \Omega(N - N') + \Lambda} \rightarrow i\pi\delta(\Lambda) + P\left(\frac{1}{\Lambda}\right). \quad (39)$$

Here, we neglect the principal-value integrals related to the oscillation frequency shift, since scattering by acoustic lattice vibrations with a wide spectrum is assumed. The equation takes the form

$$\begin{aligned}
& -[s + i\Omega(N - N')] \rho_{NN'}^{kk} + \rho_{NN'}^{kk} \Big|_{t=0} \\
& = \frac{\pi}{\hbar^2} (|V_{Nk, N+nk'}^{01}|^2 + |V_{N'k, N'+nk'}^{01}|^2) \\
& \times \{(\mathbf{v}_q + 1)\delta[\varepsilon(k') - \varepsilon(k) + n\Omega + \omega_q] \\
& + \mathbf{v}_q\delta[\varepsilon(k') - \varepsilon(k) + n\Omega - \omega_q]\} \rho_{NN'}^{kk} \quad (40) \\
& - \frac{2\pi}{\hbar^2} V_{Nk, N+nk'}^{01} V_{N'+nk, N'k'}^{10} \{ \mathbf{v}_q\delta[\varepsilon(k') - \varepsilon(k) + n\Omega + \omega_q] \\
& + (\mathbf{v}_q + 1)\delta[\varepsilon(k') - \varepsilon(k) + n\Omega - \omega_q]\} \rho_{N+n, N'+n}^{k'k'}.
\end{aligned}$$

Equation (40) describes a loss of coherence between the states $|N, k\rangle$ and $|N', k\rangle$ due to electron transitions with the absorption or emission of phonons; the first and second terms are related, respectively, to the loss of an electron from these states and to the arrival of an electron from the states with other Stark indices and wave vectors of transverse motion.

The structure and the physical nature of the loss term are absolutely clear: it contains a half-sum of probabilities of the electron loss from the states $|N, k\rangle$ and $|N', k\rangle$ and the decoherence process occurs due to a decrease in the amount of electrons forming the coherent superposition; a phase factor is absent.

The structure of the arrival term is essentially more complicated. It follows from (26) that $V_{Nk, N+nk'}^{01} V_{N'+nk, N'k'}^{10} = \exp[iq_{\parallel}a_{\parallel}(N - N')]|V_n^q|^2$. We see that transitions in the arrival term can lead both to weakening or enhancement of coherence between the states N and N' , depending on the phase shift between $\rho_{NN'}^{kk}$ and $\rho_{N+n, N'+n}^{k'k'}$ and the tapering of the phonon phase $q_{\parallel}a_{\parallel}(N - N')$ across the distance between the corresponding QDSL sites (the form of the phase factor will be explained below). As rigorously proven in [20], the presence of the phase factor in the electron arrival term ensures a predominance of escape over arrival, which leads to damping of BOs in the course of time.

It should be noted that, in deriving the quantum kinetic equation (40), we have assumed that a coherent superposition of the Stark states is formed at zero time and, therefore, owing to (34), the amplitude of the current of Bloch oscillations is essentially larger than the dc current. The latter can exist due to scattering only and is disregarded in the obtained equation. However, with BO damping, the dc current becomes comparable with the BO current amplitude. At long intervals of time, when the coherence between the Stark states is completely destroyed, the diagonal elements of DM become dominant on the right-hand side of (38), while the off-diagonal ones are nonzero only if the charge carriers are scattered. Therefore, the procedure that we used here is invalid for calculating the dc current. The procedure for deriving equations for DM at large times and calculating the dc current is described in detail in [19]. This procedure can also be successfully used to calculate the static current–voltage characteristic of a QDSL.

The equations (40) are sufficiently complex for analysis under arbitrary initial conditions; that is why, for the remainder of this paper, we confine our consideration to an analysis of the spatially uniform initial state of the system.

4.1. Spatially Uniform Case

The equations (40) are significantly simplified for the case of a spatially uniform initial distribution:

$$\rho_{N+n, N'+n}^{kk} = \rho_{NN'}^{kk}. \quad (41)$$

The set of equations relating the DM elements with the form $\rho_{N+n, N'+n}^{kk}$ with different n is reduced to a set of independent closed equations.

Moreover, when the electric field is directed along one of the basis directions of a rectangular 2D QDSL (or tetragonal 3D QDSL), the nearest neighbor tight binding approximation is valid and it suffices to solve one of these equations in order to describe the BO. Indeed, expressing the current density in the Wannier site representation (20) in terms of the DM in the Stark representation

$$j = -\frac{en_e\Delta_{\parallel}a}{\hbar} \times \text{Im} \left(\sum_{N, k, N', k', n_{\perp}} \langle N, k | n_{\parallel}, n_{\perp} \rangle \langle n_{\parallel} + 1, n_{\perp} | N', k' \rangle \rho_{NN'}^{kk} \right) \quad (42)$$

and using the orthogonality of the Stark states, we find that, under condition (41), the current density within the nearest neighbor approximation can be expressed in terms of a single DM element $\rho_{N, N+1}^{kk}$ describing coherent transitions between neighboring Stark states:

$$j = \frac{en_e\Delta_{\parallel}a^2}{4\pi\hbar} \int dk \text{Im} \rho_{N, N+1}^{kk}. \quad (43)$$

The uniformity (41) occurs, in particular, when the electric field is switched on instantaneously. For a non-degenerate electron gas, this gives

$$\begin{aligned} \rho_{N, N+1}^{kk} \Big|_{t=0} &= \int d\mathbf{K}^0 \exp(iK_{\parallel}^0 a_{\parallel}) F(\mathbf{K}^0) \delta(K_{\perp}^0 - k) \\ &= \langle \cos(K_{\parallel}^0 a_{\parallel}) \rangle f k, \quad (44) \\ \langle \cos(K_{\parallel}^0 a_{\parallel}) \rangle &= \frac{I_1(\Delta_{\parallel}/T)}{I_0(\Delta_{\parallel}/T)}, \end{aligned}$$

where I_0 and I_1 are modified Bessel functions; $F(\mathbf{K}^0)$, $f(k)$ are the Boltzmann distributions in the total energy in the QDSL miniband (3) and in the transverse motion energy, respectively.

Let us now suppose that $\rho_{N, N+1}^{kk}(t) \equiv \exp(-i\Omega t) \langle \cos(k_{\parallel}^0 a_{\parallel}) \rangle g_k(t)$. Then, (40) gives, with account of (26) and (41) for the slowly varying amplitude $g_k(t)$, the following closed equation:

$$-\frac{\partial}{\partial t} g_k(t) = \int dk' [W_{k, k'}^{\text{out}} g_k(t) - W_{k', k}^{\text{in}} g_k'(t)],$$

$$W_{k, k'}^{\text{out}} = \frac{2\pi}{\hbar^2} \sum_{l, n, g} |V_n^q|^2 \{ (v_q + 1) \delta[\varepsilon(k') - \varepsilon(k) + n\Omega + \omega_q] + v_q \delta[\varepsilon(k') - \varepsilon(k) + n\Omega + \omega_q] \} \delta(k' - k - q_{\perp} + \frac{2\pi l}{a_{\perp}}), \quad (45)$$

$$W_{k', k}^{\text{in}} = \frac{2\pi}{\hbar^2} \sum_{l, n, g} \cos(q_{\parallel} a_{\parallel}) |V_n^q|^2 \times \{ (v_q + 1) \delta[\varepsilon(k') - \varepsilon(k) + n\Omega + \omega_q] + v_q \delta[\varepsilon(k') - \varepsilon(k) + n\Omega + \omega_q] \} \delta(k' - k - q_{\perp} + \frac{2\pi l}{a_{\perp}}),$$

where summing over l ensures that the Umklapp processes in the transverse minibands are taken into account; q varies within the Brillouin zone of the QDSL material; and the transverse electron motion wave vector k varies, within the first Brillouin zone of the transverse chain of QDs in the 2D QDSL (or transverse plane of QDs in the 3D QDSL).

This is the basic equation of the theory which will be used in the second part of the study (see [20]) for calculating BO damping in QDSLs of different dimensionalities. The equation obtained is useful when there is a high electric field, i.e., when the electron is localized on a small number of QDs in the electric field direction: $L_{\text{loc}} = \Delta_{\parallel}/eF \approx a_{\parallel}$. Equation (45) becomes inconvenient because of the necessity to sum over a large number of transitions n in the case of a weak electric field, when the localization length becomes large: $L_{\text{loc}} \gg a_{\parallel}$. Meanwhile, summing over n can be done analytically using the Fourier representation for the delta function and expression (26) for the interaction matrix elements. Then, we obtain in a natural way the equation (see [19]) describing the BO damping in the Houston representation (7):

$$\begin{aligned} -\frac{\partial}{\partial t} g_k(t) &= \int d\mathbf{K}_{\parallel} \int d\mathbf{K}' \int_0^t dt' \\ &\times [W(\mathbf{K}, \mathbf{K}') g_k(t) - \cos[(K_{\parallel} - K'_{\parallel}) a_{\parallel}] W(\mathbf{K}', \mathbf{K}) g_k'(t)], \\ W(\mathbf{K}, \mathbf{K}') &= (v_q + 1) w^+(\mathbf{K}, \mathbf{K}') + v_q w^-(\mathbf{K}, \mathbf{K}'), \\ w^{\pm}(\mathbf{K}, \mathbf{K}') &= \frac{2}{\hbar} \sum_{l, g} |A_g|^2 Q^2(q) \exp \left\{ \frac{i}{\hbar} \int_0^t dt_1 [\mathcal{E}(\mathbf{K} - e\mathbf{F}t_1) - \mathcal{E}(\mathbf{K}' - e\mathbf{F}t_1) \pm \hbar\omega_q] \right\} \delta(\mathbf{K} - \mathbf{K}' - \mathbf{q}_l), \quad (46) \end{aligned}$$

$$\mathbf{K} = K_{\parallel}, k, \quad \hbar\mathbf{K}_t = \hbar\mathbf{K} + e\mathbf{F}t,$$

$$\mathbf{q}_l = \mathbf{q} + l_1 \frac{2\pi}{a_{\parallel}} \mathbf{a}_{\parallel} + l_2 \frac{2\pi}{a_{\perp}} \mathbf{a}_{\perp}.$$

Here, \mathbf{K} is the total electron wave vector in the QDSL miniband; $\mathcal{E}(\mathbf{K}) = (\Delta_{\parallel}/2) \cos(K_{\parallel} a_{\parallel}) + (\Delta_{\perp}/2) \cos(k a_{\perp})$ describes the QDSL miniband spectrum (3); $iA_g Q(q)$ is

the electron–phonon interaction matrix element calculated with the use of the miniband of the Bloch wave functions [see (4) and (26)]. The values $W(\mathbf{K}, \mathbf{K}')$ in (46) are the conventional probabilities of a transition between the states \mathbf{K}_i and \mathbf{K}_f in the Houston representation (7) [see (19)]; the temporal exponential exactly accounts for the electric field effect on the electron–phonon collisions.

If we formally pass in (46) to the limit $F \rightarrow 0$, then the temporal exponential gives a delta function of energy and we obtain

$$-\frac{\partial}{\partial t}g_k(t) + g_k(0) = \int dK_{\parallel} \int d\mathbf{K}'$$

$$\times [W_{\text{cl}}(\mathbf{K}, \mathbf{K}')g_k(t) - \cos[(K_{\parallel} - K'_{\parallel})a_{\parallel}]W_{\text{cl}}(\mathbf{K}', \mathbf{K})g_k(t)],$$

$$W_{\text{cl}}(\mathbf{K}, \mathbf{K}') = (v_q + 1)w_{\text{cl}}^+(\mathbf{K}, \mathbf{K}') + v_q w_{\text{cl}}^-(\mathbf{K}, \mathbf{K}'), \quad (47)$$

$$w_{\text{cl}}^{\pm}(\mathbf{K}, \mathbf{K}') = \frac{2}{\hbar} \sum_{l, q} |A_q|^2 Q^2(q) \delta[\varepsilon(\mathbf{K} - \varepsilon(\mathbf{K}') \pm \hbar\omega_q] \\ \times \delta(\mathbf{K} - \mathbf{K}' - \mathbf{q}_l).$$

The physical meaning of the phase factor $\cos[(K_{\parallel} - K'_{\parallel})a_{\parallel}] = \cos(q_{\parallel}a_{\parallel})$ becomes clear, with respect to the electron arrival term, from (46, 47). Indeed, the phase of the function $g_k(t)$ does not depend on the wave vector of transverse motion, since it is a diagonal in k DM element $\rho_{N, N+1}^{kk}$ (44). The element

$$\rho_{N, N+1}^{kk} = \exp\{iK_{\parallel}a_{\parallel}[N - (N+1)]\} \\ = \exp(-i\mathbf{K}_{\parallel}a_{\parallel}) \quad (48)$$

is related to an electron in the Bloch state with the wave vector \mathbf{K} , and the wave vector itself varies in the presence of a field as $\hbar\mathbf{K}_t = \hbar\mathbf{K}^0 + e\mathbf{F}t$, which is in accordance with (7). After averaging over the initial wave vectors, we see that the function $g_k(t) = \exp(i\Omega t) \langle \cos(K_{\parallel}^0 a_{\parallel}) \rangle^{-1} \rho_{N, N+1}^{kk}(t)$ is real at the initial moment of time; i.e., its phase is the same for all the states of the transverse spectrum with different values of k .

The function g_k decreases upon electron transitions from the states $|N, k\rangle, |N+1, k\rangle$ to any other states simply because of a decrease of the number of electrons with the transverse wave vector k and which are involved in the coherent superposition. That is why no phase factor is present in the escape term (46), (47). On the contrary, the phase acquired by electrons via interaction with a phonon in transitions to the states $|N, k\rangle, |N+1, k\rangle$ is important. The arrival of electrons corresponds to a decrease or increase of coherence between the states $|N, k\rangle, |N+1, k\rangle$, depending on the longitudinal momentum $\hbar(K_{\parallel} - K'_{\parallel})$ lost (acquired) during the emission (absorption) of a phonon. Taking into account

(48) and the fact that the phase g_k is the same for all k prior to the interaction, we obtain the phase factor $\exp(\pm iq_{\parallel}a_{\parallel})$ in the arrival term (the imaginary, antisymmetric part of the exponential does not contribute to the integral over q_{\parallel} and can be dropped).

One can pass to the limit $F \rightarrow 0$ in (46) only under the condition $\tau_{\text{eff}}^{-1} \ll \Omega \ll \Delta_{\parallel}/\hbar$. Then, the condition for the weak scattering of oscillations, used in deriving the equation, is satisfied and, at the same time, the electron is weakly localized by the electric field, which allows us to neglect the effect of the field upon the electron–phonon collisions.

5. CONCLUSION

The kinetic equation (40) that describes BO damping was derived from the general equation for the density matrix. The theory is valid for the arbitrary excitation of BO in the miniband of a QDSL of any symmetry in an electric field with an arbitrary magnitude and direction.

It is shown that, by varying the magnitude and direction of the electric field relative to the QDSL axes, one can completely suppress single-phonon scattering by optical phonons [conditions (24) and (23)], which is the main reason for the rapid damping of BO in layered superlattices based on III–V or II–VI compounds. Control of the QDSL spectrum by the electric field is shown to allow significant suppression of scattering by acoustic phonons between different states of the Stark ladder [condition (33)]. Then, the only remaining scattering channel for carriers in an ideal 2D or 3D QDSL is scattering by acoustic phonons within the transverse minibands of the Stark ladder.

A detailed analysis of Eqs. (45)–(47) for QDSLs of various dimensionalities is conducted in our next paper, which was published in this issue of the journal [20]; we would now like to draw attention to the most essential property of these equations which distinguishes them from the usual kinetic equations and indicates specific features of phase scattering.

Let us assume that the spatial nonuniformity scale of the scattering potential (in our case, it is the phonon wavelength) in the electric field direction significantly exceeds the QDSL period. Then, the longitudinal wave vector of the electron remains virtually unchanged during scattering and the phase factor $\cos[(K_{\parallel} - K'_{\parallel})a_{\parallel}] = \cos(q_{\parallel}a_{\parallel})$ in Eqs. (45)–(47) is close to unity. Recalling now that the oscillation current (43) is proportional to the integral of the function g_k over the transverse quasimomenta and integrating both sides of any of Eqs. (45)–(47) over k under the condition $q_{\parallel} = 0$, we find that the integral of the right-hand sides of these equations becomes identically zero: there is no damping of the BO current under these conditions. This reflects a specific feature of the phase scattering: a loss of coherence between the Stark states does not occur if

the perturbation affects both states similarly. In particular, BO damping is absent only if the electron wave vector that is transverse relative to the electric field direction changes during scattering, while $K_{\parallel} - K'_{\parallel} = q_{\parallel} = 0$. Thus, the BO damping rate is close in its physical meaning to the scattering rate of the electron longitudinal quasimomentum.

Such a concept, however, may lead to misunderstanding. The electron motion along a strong electric field is quantized, and the longitudinal quasimomentum makes no physical sense. However, it seems to follow from the aforesaid that scattering within transverse bands of the Stark ladder in the absence of transitions between them must not lead to BO damping, since this is the perturbation of the transverse motion of carriers. However, this conclusion is wrong. The longitudinal momentum component of a phonon emitted or absorbed by an electron can take arbitrary values ($q_{\parallel} \neq 0$) during transitions within the transverse miniband. The conservation law of the longitudinal momentum component is satisfied as before, but the recoil momentum is acquired by the SL as a whole, not by the field-localized electron. Thus, $\cos[(K_{\parallel} - K'_{\parallel})a_{\parallel}] = \cos(q_{\parallel}a_{\parallel}) \neq 1$ in scattering within transverse minibands and such scattering leads to BO damping. In addition, when conditions (23), (24), and (33) are satisfied, this scattering channel in an ideal QDSL becomes the principal one and the BO damping is completely determined from scattering by acoustic phonons within the transverse minibands of the Stark ladder. An analysis of the possible ways to reduce the BO damping rate during electron transitions within the transverse minibands is the subject of our next work [20]. A general analysis of Eqs. (45)–(47) for QDSLs of various dimensionalities and the numerical calculation of the BO damping rate will also be carried out.

ACKNOWLEDGMENTS

This study was supported by the Russian Foundation for Basic Research (project no. 99-02-16796), the State Program for the Support of Leading Scientific Schools (project no. 00-15-96812), and the program “Physics of Solid-State Nanostructures.”

REFERENCES

1. F. Bloch, *Z. Phys.* **52**, 555 (1928).
2. J. Feldmann, K. Leo, J. Shah, *et al.*, *Phys. Rev. B* **46**, 7252 (1992).
3. K. Leo, P. H. Bolivar, F. Bruggeman, *et al.*, *Solid State Commun.* **84**, 943 (1992).
4. L. V. Keldysh, *Fiz. Tverd. Tela (Leningrad)* **4**, 2265 (1962) [*Sov. Phys. Solid State* **4**, 1658 (1962)].
5. L. Esaki and R. Tsu, *IBM J. Res. Dev.* **14**, 61 (1970).
6. C. Washke, H. G. Roskos, K. Leo, *et al.*, *Semicond. Sci. Technol.* **9**, 416 (1994).
7. K. Leo, *Semicond. Sci. Technol.* **13**, 249 (1998).
8. F. Rossi, *Semicond. Sci. Technol.* **13**, 147 (1998).
9. T. Dekorsy, R. Ott, H. Kurz, and K. Kohler, *Phys. Rev. B* **51**, 17275 (1995).
10. I. A. Dmitriev and R. A. Suris, *Fiz. Tekh. Poluprovodn. (St. Petersburg)* **35**, 219 (2001) [*Semiconductors* **35**, 212 (2001)].
11. W. V. Houston, *Phys. Rev.* **57**, 184 (1940).
12. G. H. Wannier, *Phys. Rev.* **117**, 432 (1960).
13. J. Callaway, *Energy Band Theory* (Academic, New York, 1964; Mir, Moscow, 1969).
14. R. A. Suris, in *Future Trends in Microelectronics: Reflections on the Road to Nanotechnology*, Ed. by S. Luryi, J. Xu, and A. Zaslavsky (Kluwer, Dordrecht, 1996); NATO ASI Series, Ser. E: Applied Sciences, vol. 323, p. 197.
15. W. Kohn and J. M. Luttinger, *Phys. Rev.* **108**, 590 (1957).
16. R. F. Kazarinov and R. A. Suris, *Fiz. Tekh. Poluprovodn. (Leningrad)* **5**, 797 (1971) [*Sov. Phys. Semicond.* **5**, 707 (1971)].
17. R. F. Kazarinov and R. A. Suris, *Fiz. Tekh. Poluprovodn. (Leningrad)* **6**, 148 (1972) [*Sov. Phys. Semicond.* **6**, 179 (1972)].
18. R. F. Kazarinov and R. A. Suris, *Fiz. Tekh. Poluprovodn. (Leningrad)* **7**, 488 (1973) [*Sov. Phys. Semicond.* **7**, 347 (1973)].
19. R. A. Suris and B. S. Shchamkhalova, *Fiz. Tekh. Poluprovodn. (Leningrad)* **18**, 1178 (1984) [*Sov. Phys. Semicond.* **18**, 738 (1984)].
20. I. A. Dmitriev and R. A. Suris, *Fiz. Tekh. Poluprovodn. (St. Petersburg)* **36** (12), 1460 (2002) [*Semiconductors* **36**, 1375 (2002)].

Translated by S. Kitorov

LOW-DIMENSIONAL SYSTEMS

Damping of Bloch Oscillations in One-, Two-, and Three-Dimensional Quantum-Dot Superlattices

I. A. Dmitriev* and R. A. Suris

*Ioffe Physicotechnical Institute, Russian Academy of Sciences,
ul. Politekhnikeskaya 26, St. Petersburg, 194021 Russia*

* e-mail: dmitriev@theory.ioffe.rssi.ru

Submitted May 14, 2002; accepted for publication May 16, 2002

Abstract—In the preceding paper by the same authors, the density-matrix formalism was used to derive a quantum kinetic equation describing the damping of Bloch oscillations (BOs) in perfect one-, two-, and three-dimensional quantum-dot superlattices (QDSLs) and the conditions were determined under which the only process of the charge-carrier scattering by phonons in 2D and 3D QDSLs that contributes to the BO damping is the acoustic-phonon scattering within the transverse minibands of the Stark ladder of the carrier states. In this paper, the possibilities of suppressing this remaining scattering channel are analyzed. It is shown that the BO damping time in 2D and 3D QDSLs at room temperature may exceed the oscillation period by a factor of several hundreds and the conditions necessary for such strong suppression of the scattering are revealed. This makes a considerable difference between the QDSLs and the quantum-well superlattices, where, in reality, the BOs damping over a single oscillation period at room temperature. © 2002 MAIK “Nauka/Interperiodica”.

1. INTRODUCTION

In the authors' preceding paper [1], the density-matrix formalism was used to derive a quantum kinetic equation describing the damping of Bloch oscillations (BOs) in superlattices (SLs) composed of quantum dots (QDs). It was shown that, varying the strength of the electric field and its orientation with respect to the axes of the quantum-dot SL (QDSL), it is possible to suppress completely the optical-phonon scattering of the charge carriers, which is largely responsible for the fast damping of BOs in layered SLs composed of quantum wells (QWSLs). It was also shown that the acoustic-phonon scattering between the different levels of the Stark ladder formed by the carrier states in a QDSL under an applied electric field can be very strongly suppressed by the field as well. Thus, conditions were revealed under which a single channel of the charge-carrier scattering remains: the acoustic-phonon scattering between the states of transverse motion within a Stark-ladder level.

In this study, we use the quantum equation for relaxation obtained in [1] to investigate the possibility of suppressing the scattering in this channel and, correspondingly, of increasing considerably the BO damping time for a chain of QDs (a one-dimensional QDSL) and for two- and three-dimensional QDSLs. We examine the dependences of the BO damping rate on the QDSL parameters and on the strength and orientation of the electric field, as well as its temporal dependence. We also show that the possibility of effectively controlling the spectrum of 2D and 3D QDSLs by the electric field enables one to suppress considerably the acoustic-phonon scattering within the transverse minibands of

the Stark ladder. The numerical calculations carried out in this study demonstrate that the BO damping time in 2D and 3D QDSLs at room temperature may exceed the oscillation period by several hundred times. This makes a considerable difference between QDSLs and QWSLs: in the latter case, at room temperature, the BOs actually damping over a single oscillation period [2].

For 2D and 3D QDSLs, Eqs. (45) and (47) of [1] are quite complicated due to the existence of a transverse spectrum. Thus, for the purpose of illustration, we first analyze the BO damping in a 1D chain of QDs and demonstrate in a simple way that the BO damping rate (which is, in fact, the rate of the phase scattering upon electron transitions between the Stark-ladder states) differs from the conventional rate of electron–phonon collisions.

2. ONE-DIMENSIONAL QUANTUM-DOT SUPERLATTICE

Consider a 1D chain with a period a composed of QDs the coupling between which is characterized by resonance integrals $\Delta_{\parallel}/4$. Equations (45) and (47) of [1], which describe the damping of the BOs that takes place after the field is instantaneously switched on, take the following simple form:

$$\begin{aligned} (\partial/\partial t + \gamma)g(t) &= 0, \\ \gamma &= \frac{\pi}{\hbar^2} \sum_n \int_{V_0} \frac{d^3 q}{(2\pi)^3} (2v_q + 1) \\ &\times \left| V_{N+1, N+1+n}^q - V_{N, N+n}^q \right|^2 \delta(n\Omega - \omega_q), \end{aligned} \quad (1)$$

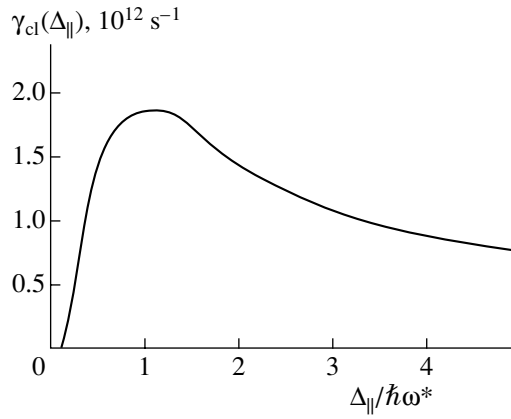


Fig. 1. Dependence of the BO damping constant in the quasi-classical limit on the miniband width in the 1D QDSL.

$$j(t) = \frac{en_e \Delta_{||} a_{||}}{\hbar} \langle \cos K_{||}^0 a_{||} \rangle \sin(\Omega t) \exp(-\gamma t).$$

One can see that, in the spatially uniform case, the BOs in 1D QDSLs experience exponential damping with the decrement γ . The value of the decrement depends on the difference between the interaction matrix elements in the neighboring Stark states (it is the loss of coherence between these states that is described by Eq. (1)). In this situation, the phase of the Stark electron in the phonon field becomes important:

$$V_{N, N+n}^q = V_n^q e^{iq_{||} a_{||} N},$$

$$|V_n^q| = \mathbf{A}_q Q(q) J_n[\lambda \sin(q_{||} a_{||}/2)], \quad \lambda = \frac{\Delta_{||}}{\hbar \Omega}, \quad (2)$$

$$|V_{N+1, N+1+n}^q - V_{N, N+n}^q|^2 = 2[1 - \cos(q_{||} a_{||})] |V_n^q|^2.$$

Thus, the expression for γ differs from the conventional expression for the probability of an electron transition with the emission or absorption of a phonon by the phase factor $[1 - \cos(q_{||} a_{||})]$. This is representative of phase scattering: the coherence between the states N and $N+1$ is not lost if the action of the scattering potential on both states is identical. In particular, this is the case for scattering by phonons whose wavelengths are much longer than the SL period.

In the limiting case of a weak electric field ($\tau_{\text{eff}}^{-1} \ll \Omega \ll \Delta_{||}/\hbar$), the expression for the damping constant γ takes the following form, according to Eq. (47) of [1]:

$$\gamma_{\text{cl}} = \frac{\pi}{\hbar^2} \oint \frac{adK}{2\pi} \int \frac{v_0 d^3 q}{(2\pi)^3} (2v_q + 1) |A_q|^2 Q^2(q) \times [1 - \cos(q_{||} a_{||})] \delta[|\varepsilon(K) - \varepsilon(K + q_{||})| - \omega_q], \quad (3)$$

where $\varepsilon(K) = \Delta_{||}/2\hbar \cos(Ka)$ describes the miniband spectrum of the QD chain in the absence of an electric field.

The dependence $\gamma_{\text{cl}}(\Delta_{||})$ is shown in Fig. 1.¹ Let us comment on the shape of this curve.

(a) For $\Delta_{||} a/2\hbar < s$, the electron group velocity in the miniband is always smaller than the sound velocity and the one-phonon scattering processes are forbidden by the energy and momentum conservation laws.

(b) For $\Delta_{||} a/2\hbar > s$, phonons of increasingly high energy become involved in the scattering as the miniband width increases. In the vicinity of $\Delta_{||} a/\hbar = s$, the damping constant grows as $\Delta_{||}^{3/2}$; then, the growth becomes linear, while the energy of participating phonons is now limited by the miniband width.

(c) Finally, for $\Delta_{||} \geq \hbar\omega^*$, the form factor $Q(q)$ given by formula (27) of [1] comes into play, which leads to a suppression of the processes with the participation of the short-wavelength phonons, and the scattering becomes quasi-elastic. Meanwhile, the density of electron states falls as $\Delta_{||}^{-1}$ with an increase in the miniband width; for $\Delta_{||} \gg \hbar\omega^*$, this results in a similar dependence for the oscillation damping constant: $\gamma_{\text{cl}}(\Delta_{||}) \propto \Delta_{||}^{-1}$.

Next, let us consider the field dependence of the damping constant. Integration of Eq. (1) with (2) taken into account yields

$$\gamma = \frac{2G^2 \theta}{\pi \hbar^2 s^2 \rho_a a^2} \sum_{n>0} n q_F Q^2(n q_F/a) \int_0^{n q_F/2} dx \sin^2 x J_n^2(\lambda \sin x). \quad (4)$$

¹ In the numerical calculations throughout this paper, we consider only the case of high temperatures, which is the most interesting for practical applications of BOs, and assume that $T = 300$ K. The material parameters of GaAs are used to describe the electron-phonon interaction: sound velocity $s = 5.22 \times 10^5$ cm/s, deformation potential constant $G = 6$ eV, and mass density $\rho_a = 5.3$ g/cm³. Neglecting the difference between the material constants inside and outside the QDs, we assume the phonon spectrum to be linear and isotropic: $\omega_q = sq$. In the calculations, we assume that the QD diameter is smaller than the QDSL period by a factor of 2 ($|\mathbf{a}_i| = a = 4R_D = 100$ Å) and disregard the existing relation between the QD size R_D , the QDSL periods $|\mathbf{a}_i|$, and the resonance integrals Δ_{a_i} that characterize the coupling between the QDs in the corresponding directions. The last approximation has virtually no effect on the calculation results since the resonance integrals depend exponentially on the QD spacing, and their values change considerably with a logarithmically small variation in $|\mathbf{a}_i|$ or R_D . In the calculations, we use formula (31) of [1] for the form factor $Q(q)$ for the well with infinitely high walls. For the QDSL parameters listed above, the energy of significant phonons, determined by the form factor, is equal to $\hbar\omega^* = \hbar s \pi/R_D = 4.3$ meV $\ll T$ (where $T = 300$ K is the lattice temperature); thus, the phonon occupation numbers can be calculated by the asymptotic relation $(v_q + 1/2) \approx T/\hbar\omega_q$. The wavelength of significant phonons greatly exceeds the maximum wave vector of the electron in the QDSL Brillouin zone $q^* = \pi/R_D \gg \pi/a$; consequently, the Umklapp processes are of significance.

Here, $q_F = \Omega a/s = eFa^2/\hbar s$ and $\lambda = \Delta_{\parallel}/\hbar\Omega$ determines the size of the electron localization region in the electric field.

Figure 2 represents the dependence of the damping constant $\gamma(\Omega, \Delta_{\parallel}/\hbar\omega^*)$. At weak fields, γ approaches its classical limit (3). With increasing electric field, the interval between the Stark levels increases and the transitions between the Stark states separated by a large number of chain periods (which are described by large n in (4)) become suppressed due to the field-induced localization and the decrease of the form factor. In weak fields ($\Omega < \omega^*$) in QDSLs with narrow minibands ($\Delta_{\parallel} < \hbar\omega^*$), the transitions with $n \gg 1$ are suppressed mainly due to the electron localization by the electric field; in QDSLs with wide minibands ($\Delta_{\parallel} > \hbar\omega^*$), only the form factor limits the values of n that are significant.

For the chosen set of QDSL parameters, $\omega^* = 6.3 \times 10^{12} \text{ s}^{-1}$. From Fig. 2, one can easily determine where the damping constant becomes smaller than the Stark frequency and, thus, the minimum field strength required in order to observe BOs in the QDSL of a given miniband width Δ_{\parallel} .

When $\Omega > \omega^*$, the reduction in the form factor leads to the suppression of the transitions between the neighboring Stark levels, which results in a rapid decrease in γ for any value of Δ . It was established in [1] that the asymptotic behavior of the form factor for the short-wavelength phonons is expressed by $Q(q > q^*) \propto q^{-\beta}$, $\beta \geq 3$ (see (30) in [1]). Thus, it follows from (4) that, if in the fields F exceeding $\hbar\omega^*/ea$ the electrons are already strongly localized (i.e., $\lambda \ll 1$), then $\gamma \propto F^{-2\beta}$; if $\lambda > 1$, then $\gamma \propto F^{2-2\beta}$. By increasing the field strength, one can obtain arbitrarily long BO damping times. In the actual experimental conditions, this would mean that the damping of the BOs at $\Omega \gg \omega^*$ will be determined by the degree of imperfection of the real QDSL structure, while the damping originating from the phonon scattering can be suppressed as strongly as is wished.

3. TWO- AND THREE-DIMENSIONAL QUANTUM-DOT SUPERLATTICES

In 2D and 3D QDSLs, the charge carriers can move in the direction perpendicular to the electric field, which leads to significant complication of their behavior. The damping of the BOs is no longer exponential. The time-dependent damping rate is still determined by $\gamma(k)$; the mathematical structure and physical meaning of this quantity are similar to those of the damping constant γ for the BOs in 1D QDSLs (see Eq. (1)), but now it depends on the wave vector k characterizing the electron motion in the transverse miniband. However, along with $\gamma(k)$, the quantum equation for relaxation in 2D and 3D QDSLs contains terms describing specific mixing processes in the transverse minibands, which will be considered below. It will be seen that the mixing itself does not result in BO damping, but it appears to

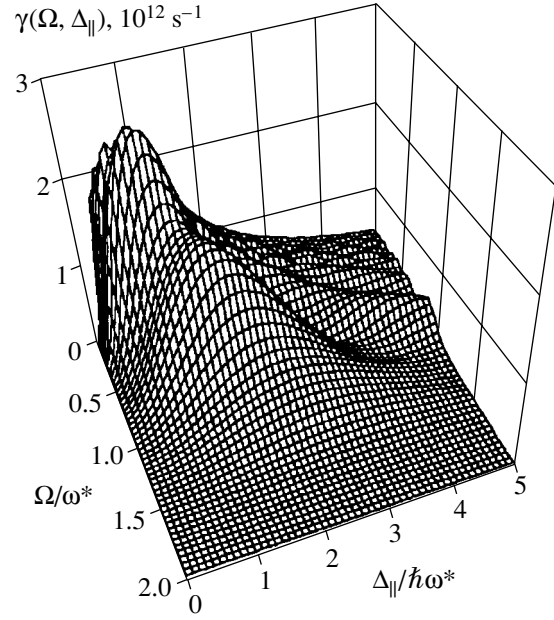


Fig. 2. Dependence of the BO damping constant in the 1D QDSL on the electric field strength $\Omega/\omega^* = eFa/(\hbar s\pi/R_D)$ and the miniband width $\Delta_{\parallel}/\hbar\omega^*$.

have a significant effect on the form of the temporal dependence of the oscillation damping.

In the case of 2D QDSLs, Eq. (45) of [1] for $g_k(t) \equiv e^{i\Omega t} \langle \cos(K_{\parallel}^0 a_{\parallel})^{-1} \rho_{N, N+1}^{kk} \rangle$, describing the loss of coherence between the states $|N, k\rangle$ and $|N+1, k\rangle$, can be written as

$$\begin{aligned} -\frac{\partial}{\partial t} g_k(t) &= \sum_{k'} J_{kk'} g_{k'}(t) \\ &= \sum_{k'} \left[\delta_{k, k'} \sum_{k_1} W_{kk_1}^{\text{out}} - W_{kk'}^{\text{in}} \right] g_{k'}(t), \end{aligned}$$

$$\begin{aligned} W_{kk'}^{\text{out}} &= \frac{2\pi}{\hbar^2} \sum_{l, n, g} |V_n^q|^2 \{ (v_q + 1) \delta[\varepsilon(k') - \varepsilon(k) + n\Omega + \omega_q] \\ &+ v_q \delta[\varepsilon(k') - \varepsilon(k) + n\Omega - \omega_q] \} \delta\left(k' - k - q_{\perp} + \frac{2\pi l}{a_{\perp}}\right), \end{aligned} \quad (5)$$

$$\begin{aligned} W_{kk'}^{\text{in}} &= \frac{2\pi}{\hbar^2} \sum_{l, n, g} \cos(q_{\parallel} a_{\parallel}) |V_n^q|^2 \\ &\times \{ (v_q + 1) \delta[\varepsilon(k') - \varepsilon(k) + n\Omega - \omega_q] \\ &+ v_q \delta[\varepsilon(k') - \varepsilon(k) + n\Omega + \omega_q] \} \\ &\times \delta\left(k' - k - q_{\perp} + \frac{2\pi l}{a_{\perp}}\right). \end{aligned}$$

Here, the wave vector q varies within the first Brillouin zone of the constituent material of the QDSL, and the wave vector k of the electron transverse motion varies within the first Brillouin zone of the transverse chain of QDs. The spectrum of the transverse miniband is given by the expression $\epsilon(k) = \Delta_{\perp}/2\cos(ka_{\perp})$. The Umklapp processes are taken into account by the summation over l . The matrix elements V_n^q are determined by formulas (26) and (28) of [1].

According to (43) of [1], the BO current is expressed in terms of $g_k(t)$ as

$$j(t) = j_0(t)\tilde{j}(t), \quad j_0(t) = \frac{en_e\Delta_{\parallel}a_{\parallel}}{2\hbar}\langle\cos(K_{\parallel}^0a_{\parallel})\rangle\sin(\Omega t), \quad (6)$$

$$\tilde{j}(t) = \sum_k g_k(t).$$

Here, $j_0(t)$ is the BO current in the absence of scattering, and $\tilde{j}(t)$ describes the damping of the BO current amplitude.

The structure of the operator \hat{J} in (5) implies that, in contrast to the case of 1D QDSLs, the BO damping in the presence of the continuous spectrum of the transverse motion is not, in general, exponential. Thus, it is convenient to introduce the time-dependent damping rate as

$$\Gamma_j(t) = -\frac{d}{dt}\ln\tilde{j}(t). \quad (7)$$

The damping rate at the instant when the electric field is switched on ($t=0$) can be easily calculated analytically. Substituting the initial conditions $g_k(t=0)$ into the right-hand side of (5), we obtain

$$\Gamma_j(t=0) = \sum_{k,k'} g_k^{-1}(t=0)J_{kk'}g_{k'}(t=0). \quad (8)$$

To gain some insight into the temporal dependence of the BO damping rate $\Gamma_j(t)$, it is useful to express formally the solution to the equation set (5) in the following form:

$$g_k(t) = \sum_i c_k^i \exp(-\eta_i t), \quad (9)$$

$$\tilde{j}(t) = \sum_i \operatorname{Re}\left[\sum_k c_k^i \exp(-i\operatorname{Im}\{\eta_i\}t)\right] \exp(-\operatorname{Re}\{\eta_i\}t).$$

Here, η_i are the eigenvalues of the operator \hat{J} . One can see from (9) that, in general, the temporal dependence of the current amplitude is not monotonic; in particular, it can change sign, which corresponds to the shift of the oscillation phase by π . Since the matrix $J_{kk'}$ is not symmetric, the eigenvalues and the expansion coefficients are complex quantities.

It can be strictly demonstrated that the amplitude of the oscillations calculated by solving Eq. (5) cannot grow at infinity; i.e., the real parts $\operatorname{Re}\{\eta_i\}$ of all eigenvalues of the matrix $J_{kk'}$ are positive. This can be proven with the use of the following theorem (Gershgorin, 1931) [3, 4].

Theorem. Any eigenvalue ν of an arbitrary complex $n \times n$ matrix $\|a_{ij}\|$ lies within one of the circles

$$|a_{ii} - \nu| \leq \sum_{j \neq i} |a_{ij}| \quad (i = 1, \dots, n). \quad (10)$$

Applying this theorem to Eq. (5), one finds that, due to the presence of the phase factor $\cos(q_{\parallel}a_{\parallel})$ in the terms describing electron influx, the sum of the absolute values of the nondiagonal elements $W_{kk'}^{\text{in}}$ in any row (any column) of the matrix $J_{kk'}$ does not exceed the value of the diagonal element $\sum_{k'} W_{kk'}^{\text{out}}$; i.e.,

$$\sum_{k'} W_{kk'}^{\text{out}} \geq \sum_{k'} |W_{kk'}^{\text{in}}|. \quad (11)$$

Then, it follows from the above theorem that the real parts of all eigenvalues $\operatorname{Re}\{\eta_i\}$ are nonnegative and the oscillation amplitude does not grow with time:

$$\operatorname{Re}\{\eta_i\} \geq \Lambda \equiv \min_k \left\{ \sum_{k'} W_{kk'}^{\text{out}} - |W_{kk'}^{\text{in}}| \right\} \geq 0. \quad (12)$$

Note that the equality sign appears in (11) and (12) only when all elements in some row of the matrix $J_{kk'}$ equal zero, i.e., when there is no scattering in a certain energy range of the transverse motion.

It will be seen below that the quantity Λ from (12) can be a good estimate for the asymptotic value of the damping rate $\Gamma_j(t)$ at $t \rightarrow \infty$, although, strictly speaking, it does not follow from the expansion (9) that the damping rate at long periods of time approaches the smallest of $\operatorname{Re}\{\eta_i\}$.

Thus, without solving the equation set, one can obtain an analytic expression for the initial damping rate $\Gamma_j(0)$ of the BO current and estimate the value $\Gamma_j(\infty)$ of the damping rate at long periods of time. The above reasoning is valid in the general case as well (see (40) in [1]), regardless of how a coherent mixture of the Stark states is formed and what the field orientation is with respect to the QDSL axes.

Here, we shall restrict our consideration to a detailed analysis of the most simple situation—which is, at the same time, most interesting from the practical point of view—where only the transitions within the transverse minibands of the Stark ladder with the participation of acoustic phonons are possible, with all other scattering mechanisms being strongly suppressed.

3.1. The damping of Bloch Oscillations due to Scattering within the Transverse Minibands

The conditions necessary for the full suppression of optical-phonon scattering were obtained in [1] as $n\Omega + \Delta_{\perp}/2\hbar < \omega_0 < (n+1)\Omega - \Delta_{\perp}/2\hbar$ and $\hbar\omega_0 > \Delta_{\perp}$. Let us suppose that they are satisfied and that the acoustic-phonon interminiband scattering is also strongly suppressed: $\hbar\Omega - \Delta_{\perp} \geq \hbar\omega^* = \hbar s\pi/R_D$. Then, the set of equations (5) takes the following form:

$$\begin{aligned} (\partial/\partial t + \gamma_k)g_k(t) &= \sum_k W_{kk'}^{\text{in}} g_{k'}(t) - W_{k'k}^{\text{in}} g_k(t), \\ \gamma_k &= \frac{\pi}{\hbar^2} \sum_q |V_{N+1, N+1}^q - V_{NN}^q|^2 \{(\nu_q + 1) \\ &\quad \times \delta[\varepsilon(k + q_{\perp}) - \varepsilon(k) + \omega_q] \\ &\quad + \nu_q \delta[\varepsilon(k + q_{\perp}) - \varepsilon(k) - \omega_q]\}, \end{aligned} \quad (13)$$

$$\begin{aligned} W_{kk'}^{\text{in}} &= \frac{2\pi}{\hbar^2} \sum_{l, q} \cos(q_{\parallel} a_{\parallel}) |V_0^q|^2 \{(\nu_q + 1) \delta[\varepsilon(k') - \varepsilon(k) - \omega_q] \\ &\quad + \nu_q \delta[\varepsilon(k') - \varepsilon(k) - \omega_q]\} \delta\left(k' - k - q_{\perp} + \frac{2\pi l}{a_{\perp}}\right). \end{aligned}$$

Here, a part of the term (5) describing the electron outflow was introduced into the left-hand side in such a way that the integral on the right-hand side over the transverse momentum k equals zero. The expression for γ_k differs from that for the BO damping constant in 1D QDSLs (see Eq. (1)) only by the appearance of the transverse-motion energy in the arguments of δ functions that account for the energy conservation law. It can be easily demonstrated that, in the presence of transverse motion, the BO damping is still mainly governed by the function γ_k , which depends on the difference between the interaction matrix elements in the neighboring Stark states. Integrating Eq. (13) over the transverse-motion wave vectors, we obtain

$$\frac{\partial}{\partial t} \int dk g_k(t) = - \int dk \gamma_k g_k(t).$$

Taking into account the relationship $\tilde{j} = \int dk g_k(t)$ (see (6)), we arrive at the conclusion that, if $\gamma_k = \text{const}(k) \equiv \gamma$, the BO amplitude dampings with the decrement γ . However, since γ_k actually exhibits some dispersion, it determines only the initial value $\Gamma_j(0)$ of the time-dependent BO-current damping rate. Indeed, substitution of the initial distribution $g_k(0) = f_k$ into the right-hand side of the equation yields zero, and we have

$$\begin{aligned} g_k(t)|_{t \rightarrow 0} &= f_k \exp(-\gamma t), \\ \Gamma_j(0) &= \int dk f_k \gamma_k \equiv \langle \gamma \rangle. \end{aligned} \quad (14)$$

Due to the nonzero dispersion of γ_k , the function $g_k(t)$ starts to deviate from the equilibrium one as time passes; thus, the right-hand side of the equation, which describes mixing within the transverse miniband, begins to contribute significantly to the oscillation damping rate. This manifests itself most clearly in the limiting case when the lattice temperature is high with respect to the energy of significant acoustic phonons and the width of the transverse miniband.

3.1.1. The damping of the Bloch oscillations for $T \gg \hbar\omega^*$, Δ_{\perp} . When $T \gg \hbar\omega^*$, the phonon occupation numbers can be approximated as $\nu_q + 1/2 \approx T/\hbar\omega_q \gg 1$ and the contribution of the processes with spontaneous phonon emission may be neglected. The set of equations (13) takes the following form:

$$-\frac{\partial}{\partial t} g_k(t) = J_{kk'} g_{k'}(t) = \gamma_k g_k(t) - \hat{M}\{g_k(t)\},$$

$$\hat{M}\{g_k(t)\} = \sum_{k'} W_{kk'}^{\text{in}} [g_{k'}(t) - g_k(t)],$$

$$\begin{aligned} \gamma_k &= \frac{\pi}{\hbar^2} \sum_q \frac{T}{\hbar\omega_q} |V_{N+1, N+1}^q - V_{NN}^q|^2 \\ &\quad \times \delta[|\varepsilon(k + q_{\perp}) - \varepsilon(k)| - \omega_q], \end{aligned} \quad (15)$$

$$\begin{aligned} W_{kk'}^{\text{in}} &= \frac{2\pi}{\hbar^2} \sum_{l, q} \frac{T}{\hbar\omega_q} \cos(q_{\parallel} a_{\parallel}) |V_0^q|^2 \\ &\quad \times \delta[|\varepsilon(k') - \varepsilon(k)| - \omega_q] \delta\left(k' - k - q_{\perp} + \frac{2\pi l}{a_{\perp}}\right). \end{aligned}$$

In contrast to the general case (see (5)), the matrix $W_{kk'}^{\text{in}}$ in (15) and, consequently, the operators \hat{M} and \hat{J} are symmetric. Then, all eigenvalues of \hat{J} η_i are real and the eigenvectors g_k^i are real and orthogonal, $\sum_i g_{k'}^i g_k^i = \delta_{k, k'}$. Taking into account the second assumption $T > \Delta_{\perp}$, the initial conditions can be written as $g_k(0) \equiv f = \text{const}(k)$, where $\sum_k f = 1$, and the formal solution (9) becomes simplified considerably:

$$\begin{aligned} g_k(t) &= \sum_i \left[\sum_{k'} f g_{k'}^i \right] g_k^i \exp(-\eta_i t), \\ \hat{j}(t) &= f \sum_i \left[\sum_k g_k^i \right]^2 \exp(-\eta_i t). \end{aligned} \quad (16)$$

It can be seen that, in contrast to the general case (9), in the limiting case of high temperatures and in the absence of transitions between the transverse minibands, the amplitude of the BO current is always positive and the rate of its damping $\Gamma_j(t)$ decreases steadily,

approaching over a long period of time the minimum eigenvalue of the operator \hat{J} .

Now, let us consider the influence of the mixing described by operator \hat{M} in (15) on the oscillation damping rate. One can see that this operator represents nonlocal diffusion in the transverse miniband. Indeed, in the case of quasi-elastic scattering, i.e., when the transverse miniband energy considerably exceeds the energy of the significant phonons ($\Delta_{\perp} > \hbar\omega^*$), \hat{M} is reduced to the conventional differential operator of diffusion over the transverse-motion energy:

$$-\sum_k W_{kk'}^{\text{in}}(g_k(t) - g_k(t)) \longrightarrow -\frac{\partial}{\partial t} \mathcal{D}(\varepsilon) \frac{\partial}{\partial \varepsilon} g(\varepsilon, t),$$

$$\mathcal{D}(\varepsilon) = \mathcal{R}(\varepsilon) \int W^{\text{in}}(\varepsilon, \varepsilon + \delta\varepsilon) \frac{\delta\varepsilon^2}{2} d\delta\varepsilon, \quad (17)$$

$$W^{\text{in}}(\varepsilon, \varepsilon') = \mathcal{R}^{-1}(\varepsilon) \oint dk \delta[\varepsilon - \varepsilon(k')] \delta[\varepsilon - \varepsilon(k)] W_{kk'}^{\text{in}},$$

$$\varepsilon(k) = \frac{\Delta_{\perp}}{2\hbar} \cos(ka_{\perp}), \quad \mathcal{R}(\varepsilon) = \left[\left(\frac{\Delta_{\perp}}{2\hbar} \right)^2 - \varepsilon^2 \right]^{-1/2},$$

where $\mathcal{R}(\varepsilon)$ is the density of states in the transverse miniband.

In contrast to the conventional diffusion operator, operator \hat{M} is nonlocal and the values $W_{kk'}^{\text{in}}$ are not necessarily positive, since they describe phase relaxation rather than the probability of transition. The diffusion coefficient may become negative. Let us consider the two cases separately.

1. $W_{kk'}^{\text{in}} > 0$ for all k and k' .

In this case, the estimation of the minimum eigenvalue η_{min} of the operator \hat{J} (see (12)) resulting from the Gershgorin theorem yields

$$\eta_{\text{min}} \geq \Lambda = \gamma_{\text{min}} \equiv \min_k \{ \gamma_k \}. \quad (18)$$

Next, in the case under consideration, the following statement is quite evident: if any of the matrix elements $W_{kk'}^{\text{in}} > 0$ from (15) is increased while γ_k is kept constant, this will lead to a narrowing of the spectrum of the operator \hat{J} and to an increase in η_{min} . Indeed, for $\gamma_k \neq \text{const}$, the effect of the first term on the right-hand side of (15) causes $g_k(t)$ to depend on the wave vector k as time passes. The effect of the diffusion term, however, reduces the dispersion of $g_k(t)$, since it results in the transport from the regions of the transverse miniband with lower γ_k to the ‘‘depletion’’ regions where γ_k exceeds the average. Thus, the diffusion actually narrows the spectrum of the operator \hat{J} . It is useful to consider the two limiting cases.

(a) If there is no diffusion ($W_{kk'}^{\text{in}} = 0$), then the matrix \hat{J} is diagonal, with its eigenvalues being γ_k ; this leads to

$$\hat{j}(t) = f \sum_k \exp(-\gamma_k t), \quad (19)$$

$$\Gamma_j(0) = \langle \gamma \rangle, \quad \Gamma_j(\infty) = \gamma_{\text{min}}.$$

(b) For a given γ_k and $W_{kk'}^{\text{in}} \rightarrow \infty$, the diffusion term results in the rapid equalization of $g_k(t)$ over the transverse miniband. However, $g_k(t) = \text{const}$ corresponds to $\Gamma_j = \langle \gamma \rangle$. It can be seen that, in the limiting case of an infinitely large mixing rate, the current dampings with a constant decrement $\Gamma_j(t) = \langle \gamma \rangle$.

2. $W_{kk'}^{\text{in}} < 0$ for all k and k' .

This case corresponds to a negative diffusion coefficient. The action of the operator \hat{M} transfers electrons from the regions of the miniband with larger γ_k to those with smaller γ_k , thus, actually widening the spectrum of \hat{J} . The current amplitude still remains finite due to the Gershgorin theorem, but the current damping rate over a long period of time becomes lower than γ_{min} :

$$0 \leq \min_k \left\{ \sum_{k'} W_{kk'}^{\text{out}} - |W_{kk'}^{\text{in}}| \right\} \quad (20)$$

$$= \Lambda \leq \Gamma_j(\infty) < \min_k \left\{ \sum_{k'} W_{kk'}^{\text{out}} + |W_{kk'}^{\text{in}}| \right\} = \gamma_{\text{min}}.$$

3.1.2. Dependence of the Bloch oscillation damping rate on the width of the transverse minibands and the strength of the electric field. We established in the previous section that the damping rate of the BO current in 2D and 3D QDSLs is time-dependent. In the case of interest (i.e., when the intraminiband scattering is dominant and the temperature is high), this rate steadily decreases with time. At the initial moment, the damping rate $\Gamma_j(0) = \langle \gamma \rangle$ (see (14)). After long periods of time have elapsed, it approaches the smallest eigenvalue of the operator \hat{J} ; this value cannot be calculated analytically, but an estimate (12), following from the Gershgorin theorem, is valid: $\langle \gamma \rangle > \Gamma_j(\infty) = \eta_{\text{min}} \geq \Lambda$.

Calculating these quantities for a QDSL, whose basic parameters were listed at the beginning of the paper, and assuming $T = 300$ K, we find that all of them depend on two variables: the ratio $\lambda = \Delta_{\perp}/(eFa_{\parallel})$, which determines the length of electron localization in the electric field, and the width of the transverse miniband Δ_{\perp} ; it is convenient to measure Δ_{\perp} in units of the energy of significant phonons, $\hbar\omega^* = \hbar s\pi/R_D$, determined by the form factor (27) from [1].

The dependences of $\Gamma_j(0)$ and $\Gamma_j(\infty)$ on λ and Δ_{\perp} are plotted in Figs. 3 and 4. One can see that the damping rate depends heavily on both parameters, which makes

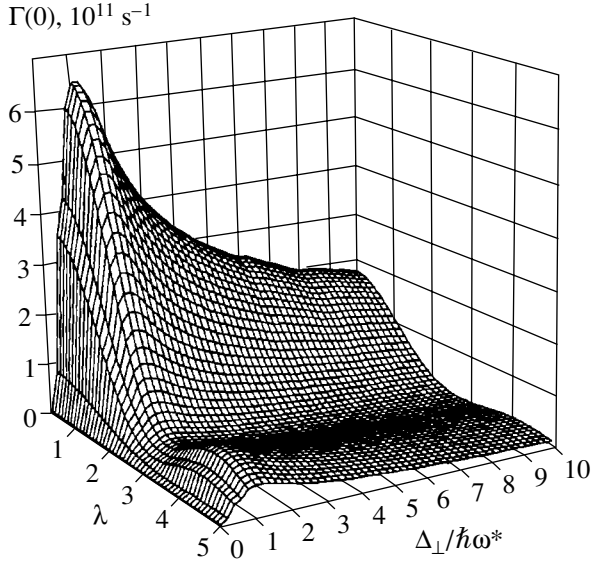


Fig. 3. The initial damping rate of the BOs (the highest damping rate).

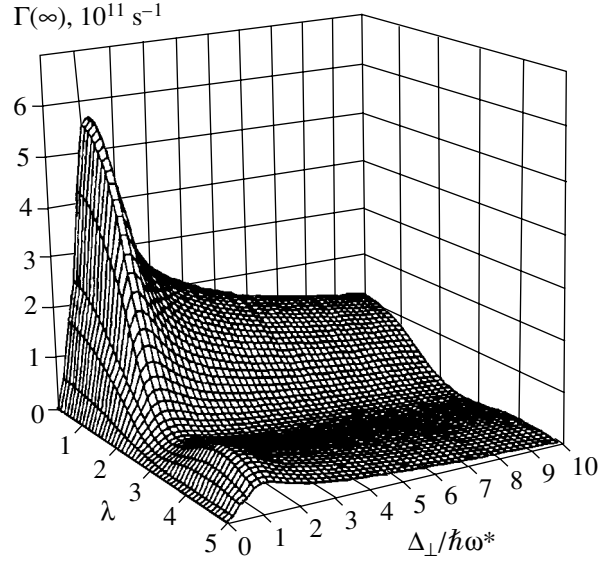


Fig. 4. The damping rate of the BOs over long times (the lowest damping rate).

it possible to effectively control the BO damping time by varying the strength and orientation of the electric field. The plot of $\Lambda/\Gamma_j(\infty)$, presented in Fig. 5, indicates that the value of Λ may serve as a good estimate for $\Gamma_j(\infty)$ for any combination of the parameters.

To explain the shape of these dependences, it is necessary to analyze in more detail the quantities that enter Eq. (15). Integrating over the phonon wave vectors, we obtain

$$W_{kk'}^{\text{in(out)}} = \frac{2\pi G^2 T}{\hbar^2 s^3 \rho_a a^2} \sum_l \frac{qa}{\pi} Q(q) \theta(p) \Phi_p^{\text{in(out)}}(\lambda),$$

$$\Phi_p^{\text{in}}(\lambda) = \frac{1}{2\pi} \int_0^{2\pi} d\varphi \cos(p a \sin \varphi) J_0^2\left(\lambda \sin \frac{p a \sin \varphi}{2}\right), \quad (21)$$

$$\Phi_p^{\text{out}}(\lambda) = \frac{1}{2\pi} \int_0^{2\pi} d\varphi J_0^2\left(\lambda \sin \frac{p a \sin \varphi}{2}\right),$$

with $\hbar s q = |\varepsilon_k - \varepsilon_{k'}|$, $q_{\perp} = k' - k + 2\pi l/a$, and $p = \sqrt{a^2 - q_{\perp}^2}$.

Here, p has the meaning of the maximum value of the longitudinal component of the phonon wave vector that is possible for given k , k' , and l . The transverse component of the phonon wave vector q_{\perp} cannot exceed the wave vector magnitude q , which is accounted for by the unit-step function $\theta(p)$.

The structure of the integrals in (21) enables one to make certain important conclusions. First of all, it can be noted that both the phase factor and the Bessel function in (21) are periodic functions of the quantity $q_{\parallel} a =$

$p a \sin \varphi$. If the transverse miniband is wide ($\Delta_{\perp} > \hbar \omega^*$), the magnitude of the significant phonon wave vectors, $q^* = \pi/R_D$, considerably exceeds the period π/a of the phase factor and the function $J_0^2[\lambda \sin\{p a \sin(\varphi/2)\}]$. Then, the integrals can be approximated by their average values, which yields

$$\langle \Phi^{\text{in}}(\lambda) \rangle \equiv \frac{1}{\pi} \int_0^{\pi} dx \cos(x) J_0^2\left(\lambda \sin \frac{x}{2}\right),$$

$$\begin{aligned} \gamma_k &= \oint \frac{dk' a}{2\pi} (W_{kk'}^{\text{out}} - W_{kk'}^{\text{in}}) \propto \langle \Phi^{\gamma}(\lambda) \rangle \\ &\equiv \frac{1}{\pi} \int_0^{\pi} dx [1 - \cos(x)] J_0^2\left(\lambda \sin \frac{x}{2}\right), \end{aligned} \quad (22)$$

$$\tau_k^{-1} = \oint \frac{dk' a}{2\pi} W_{kk'}^{\text{out}} \propto \langle \Phi^{\text{out}}(\lambda) \rangle \equiv \frac{1}{\pi} \int_0^{\pi} dx J_0^2\left(\lambda \sin \frac{x}{2}\right).$$

Dependences of the BO damping rate on the degree of electron localization in the electric field. The plots of $\langle \Phi^{\text{out}}(\lambda) \rangle$, $\langle \Phi^{\text{in}}(\lambda) \rangle$, and $\langle \Phi^{\gamma}(\lambda) \rangle = \langle \Phi^{\text{out}}(\lambda) \rangle - \langle \Phi^{\text{in}}(\lambda) \rangle$ vs. $\lambda = \Delta_{\parallel}/e F a_{\parallel}$, shown in Fig. 6, reflect the dependence of the collision rate, the efficiency of the diffusive mixing described by the operator \hat{M} in (15), and the initial damping rate of the oscillations, respectively, on the degree of electron localization in the electric field. For strongly localized electrons ($\lambda \ll 1$), the scattering probability τ_k^{-1} is the highest: the Bessel function in (22) equals unity. At the same time, averaging the cosine yields zero and, correspondingly, the effect of

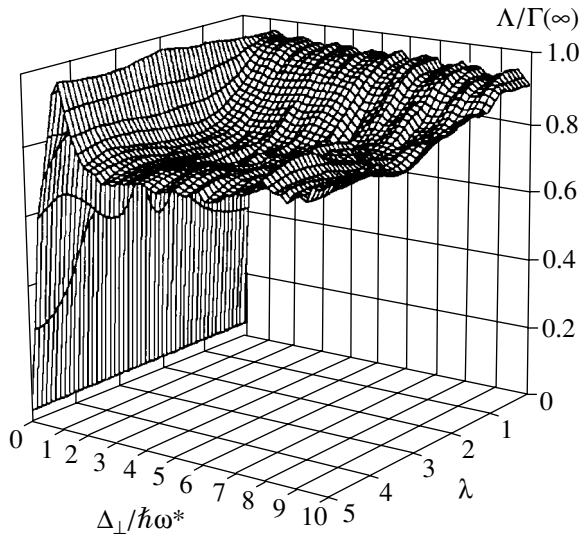


Fig. 5. The ratio of the estimate for the minimum BO damping rate obtained from the Gershgorin theorem to the actual damping rate over long times.

the diffusive mixing of the oscillation damping rate is negligibly small: expression (19) is valid for the amplitude of the current oscillations, with γ_k being identical to τ_k^{-1} . With a decrease in the field strength (i.e., with an increase in λ), the wavelength of significant phonons becomes smaller than the localization length $L_{loc} = \lambda a$ and scattering probability falls off rapidly. Meanwhile, $\langle \Phi^{in}(\lambda) \rangle$ increase with λ , and the effect of the diffusive mixing on the BO damping rate becomes important.

At $\lambda \approx 2.8$, the dependence $\langle \Phi^\gamma(\lambda) \rangle$ has a minimum. At this point, the oscillation damping rate has become three times lower than the collision rate τ_k^{-1} and one

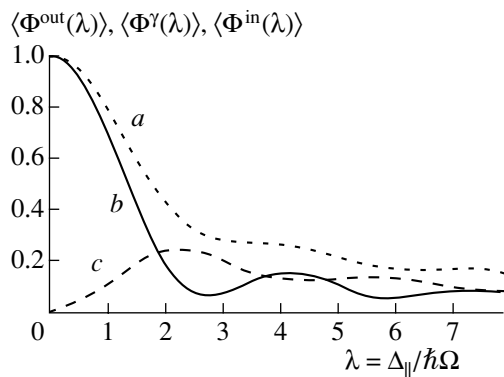


Fig. 6. Dependence of the values (a) $\langle \Phi^{out}(\lambda) \rangle$, (b) $\langle \Phi^\gamma(\lambda) \rangle$, and (c) $\langle \Phi^{in}(\lambda) \rangle$, describing the collision frequency, the BO damping rate, and the efficiency of the diffusive mixing in the transverse miniband, respectively, on the length of electron localization in the electric field measured in units of the SL period, $\lambda = L_{loc}/a$.

order of magnitude smaller than its value at $\lambda = 0$. Comparing the dependence of $\Gamma_j(0)$ and $\Gamma_j(\infty)$ on λ (Figs. 3, 4) with the function $\langle \Phi^\gamma(\lambda) \rangle$, one can see that the latter adequately describes the general behavior of the oscillation damping rate both for QDSLs with wide and narrow transverse minibands.

For $\lambda \geq 1.6$, the integral $\Phi_p^{in}(\lambda)$ in (21) is always positive for all values of p and the conclusions made in the previous section regarding the case $W_{kk'}^{in} > 0$ can be applied; in particular, the inequality $\Gamma_j(\infty) > \gamma_{min}$ is valid.

For $\lambda \leq 1.6$, the matrix elements $W_{kk'}^{in}$ can be either positive or negative. As we have shown (see Fig. 6), in the case of wide minibands for $\lambda \leq 1$, they nearly equal zero and the diffusive mixing can be neglected. However, if the transverse minibands are sufficiently narrow, the energy of significant phonons is determined by the miniband width rather than the form factor and the influence of the diffusive mixing can be significant.

Dependence of the oscillation damping rate on the width of the transverse miniband. The general run of this dependence is governed by the ratio of the transverse miniband width and the maximum energy of phonons $\hbar\omega^*$ involved in the transitions; this energy is determined by the form factor. As an example, we plot in Fig. 7 the dependence of $\Gamma_j(0)$, $\Gamma_j(\infty)$, and Λ on the transverse miniband width for the fixed parameter $\lambda = 2.8$ (this value corresponds to the first minimum in $\Phi^\gamma(\lambda)$). Let us comment on the shape of this dependence.

In the case of a narrow transverse miniband ($\Delta_\perp = \hbar\omega^*$), the energy of significant phonons is lower than the miniband width and the scattering is quasi-elastic; thus, the decrement of the damping, along with the density of states, decreases inversely proportional to the miniband width.

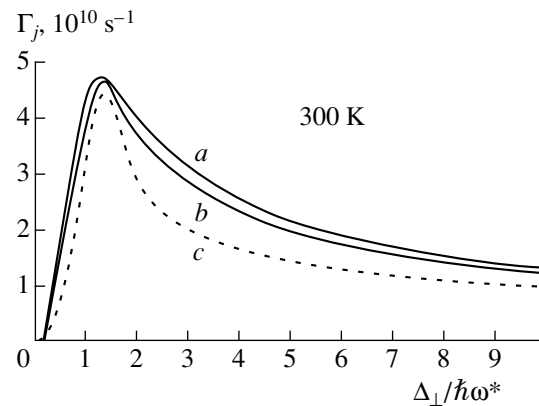


Fig. 7. Dependence of the BO damping rate on the width of the transverse miniband in the 2D QDSL for $\lambda = 2.8$ at $T = 300$ K: (a) initial damping rate of the BOs $\Gamma_j(0)$, (b) damping rate of the BOs over long times $\Gamma_j(\infty)$, and (c) estimate for the lowest BO damping rate obtained from the Gershgorin theorem, $\Lambda = \min\{\gamma_k\}$.

The increase in the damping rate at $\Delta_{\perp} \leq \hbar\omega^*$ is related to the fact that, in this case, the energy of important phonons is determined by the miniband width, rather than the form factor, and increases with the former.

Finally, in the case of very narrow minibands, $\Delta_{\perp} < 2\hbar s/a$, the group velocity of electrons is lower than the velocity of sound, and it becomes impossible to satisfy simultaneously the energy and the transverse quasi-momentum conservation laws; thus, one-phonon scattering is absent. In this case, allowance for strongly suppressed scattering between the transverse minibands (we assume that $\hbar\Omega - \Delta_{\perp} > \hbar\omega^*$) should be made. Taking into consideration that the transverse minibands are narrow ($\Delta_{\perp} < \hbar s/a \ll \hbar\omega^*$), we find that this case is equivalent to the case of 1D QDSLs.

One can see from Fig. 7 that the long damping rate $\Gamma_j(\infty)$ considerably exceeds the estimate given by $\Lambda = \min\{\gamma_k\}$ and is very close to $\Gamma_j(0) = \langle\gamma\rangle$. This is due to the fact that, for $\lambda = 2.8$, the diffusive mixing is pronounced, $\langle\Phi^{\text{in}}(2.8)\rangle \approx 3\langle\Phi^{\text{v}}(2.8)\rangle$. Thus, our arguments about the role of diffusive mixing are corroborated.

In the case of sufficiently wide transverse minibands, $\Delta_{\perp} \geq T$, which corresponds to the region $\Delta_{\perp}/\hbar\omega^* \geq 6$ in Fig. 7, the assumption about the uniform initial distribution of electrons in the transverse miniband ($f_k = \text{const}$) becomes incorrect, which should be taken into account in the calculation of $\Gamma_j(0) = \langle\gamma\rangle$. However, it appears that the corrections to be made are small provided there is no scattering by optical phonons within the transverse miniband; i.e., Δ_{\perp} should be smaller than $\hbar\omega_0$, which corresponds to $\Delta_{\perp}/\hbar\omega^* < 8$.

The condition necessary for the absence of scattering by acoustic phonons between the transverse minibands, $\hbar\Omega - \Delta_{\perp} > \hbar\omega^*$, limits the BO frequency from below by the value $f_{\text{BO}} = \omega^*/2\pi = 10^{12}$ Hz. Thus, one can see that the BO damping time in 2D QDSLs at room temperature may be as long as several hundred oscillation periods (Fig. 7), while in QWSLs at room temperature the BOs damping drastically over a single oscillation period [2].

The BO damping rate can be made even lower than 10^{10} Hz by increasing the size of the QDs that compose the SL. Indeed, the wave vectors of the phonons involved in the scattering are limited by the value $q^* = \pi/R_D$ determined by the form factor. Thus, the scattering rate (in the case of wide transverse minibands, $\Delta_{\perp} > \hbar\omega^*$) is inversely proportional to the third power of the linear dimension of a QD. Certainly, a restriction on the increase in the QD size is imposed by condition (2) of [1], which implies that the miniband originating from the ground state of quantum confinement in the dots is isolated from the other ones.

The main features of the physical pattern developed above for 2D QDSLs hold true in the 3D case as well. Both the dependence of the damping rate on the degree of electron localization in the electric field and the gen-

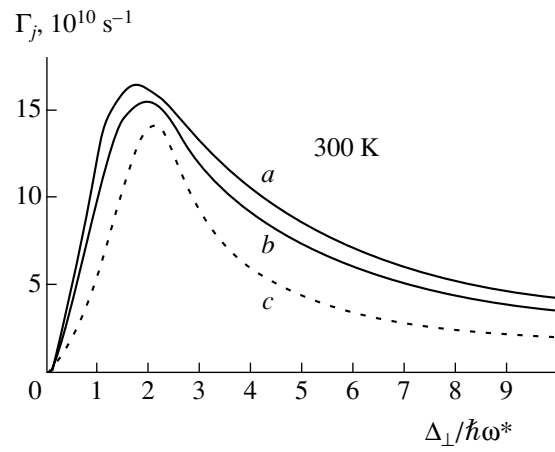


Fig. 8. Dependence of the BO damping rate on the width of the transverse miniband in the 3D QDSL for $\lambda = 2.8$ at $T = 300$ K: (a) initial damping rate of the BOs $\Gamma_j(0)$, (b) damping rate of the BOs over long times $\Gamma_j(\infty)$, and (c) estimate for the lowest BO damping rate obtained from the Gershgorin theorem, $\Lambda = \min\{\gamma_k\}$.

eral behavior of the dependence on the transverse miniband width remain the same. To account for the specific features of 3D QDSLs, the damping rate derived in the 2D case should be multiplied by a geometrical factor describing the change in the density of electron states upon the transition from a 1D to a 2D transverse miniband. It can be seen from Fig. 8 that, for the chosen QDSL parameters and the assumed dependence of the form factor Q on the phonon wave vector q , this geometrical factor is approximately equal to 4.

4. CONCLUSION

In this study, we analyzed qualitatively and quantitatively the dependence of the BO damping rate on the QDSL parameters and the strength and orientation of the electric field; the analysis was carried out on the basis of a quantum kinetic equation that describes the damping of BOs and which was derived in our preceding paper [1]. The temporal dependence of the BO damping rate was studied. We obtained analytic expressions for the initial value of the BO damping rate (i.e., at the instant when the BOs are excited) and the asymptotic value of the damping rate over long periods of time. We demonstrated that the BO damping rate is proportional to the square of the absolute value of the difference between the scattering-potential matrix elements calculated using the wave functions of neighboring Stark states. This dependence reflects the specific features of the phase scattering, and, in particular, this implies that long-wavelength excitations do not result in a loss of coherence between the Stark states or in BO damping. Due to this dependence of the damping rate on the difference between the matrix elements, this rate may be significantly lower than the reciprocal scattering time. In particular, for the case of intraminiband

scattering, the BO damping rate becomes three times lower than the collision rate when the length of electron localization in the electric field is equal to three QDSL periods.

Thus, in our preceding publication [1] and in this paper, we have demonstrated the possibility of suppressing all phonon-scattering channels in 2D and 3D QDSLs. Due to the exponential dependence of the width of the transverse-motion spectrum in QDSLs on the orientation of the electric field, the following results can be attained by varying the strength and direction of the electric field.

(i) Single-optical-phonon scattering, which is the main scattering mechanism in QWSLs and leads to a rapid damping of the BOs there, can be suppressed completely.

(ii) Scattering by acoustic phonons between the transverse minibands of the Stark ladder can be suppressed almost completely.

(iii) The BO damping rate due to the scattering by acoustic phonons within the transverse minibands can be reduced by at least two orders of magnitude.

It should be stressed once again that the density of states in a QD system is considerably higher than that in QWs and even more so in bulk semiconductors (in GaAs, the rate of collisions with acoustical phonons at room temperature is 10^{11} s^{-1}). Correspondingly, the scattering probability in the absence of an electric field is higher. Nevertheless, effective control over the spectrum of QDSLs by varying the strength and orientation of the electric field makes it possible to reduce the damping rate of the BOs in QDSLs at room temperature to $\sim 10^{10} \text{ s}^{-1}$ when the oscillation frequency f_{BO} exceeds 10^{12} Hz . This makes a considerable difference between QDSLs and QWSLs with similar parameters: in the lat-

ter case, the damping rate of the BOs at room temperature is 10^{13} s^{-1} [2] and the scattering cannot be suppressed significantly by varying the SL parameters and the strength of the electric field.

To summarize, we have shown that, in periodic quantum-dot structures of sufficiently high quality, the scattering of the charge carriers by lattice vibrations can be effectively suppressed by choosing an appropriate strength and orientation of the applied electric field. This is a significant advantage of QDSLs over layered SLs, as the former can be used to develop radiation emitters and detectors operating in the THz frequency range.

ACKNOWLEDGMENTS

This study was supported by the Russian Foundation for Basic Research (project no. 99-02-16796), the State Program for the Support of Leading Scientific Schools (grant no. 00-15-96812), and the program "Physics of Solid-State Nanostructures".

REFERENCES

1. I. A. Dmitriev and R. A. Suris, *Fiz. Tekh. Poluprovodn. (St. Petersburg)* **36** (12), 1449 (2002) [*Semiconductors* **36**, 1364 (2002)].
2. T. Dekorsy, R. Ott, H. Kurz, and K. Kohler, *Phys. Rev. B* **51**, 17275 (1995).
3. S. A. Gershgorin, *Izv. Akad. Nauk SSSR, Ser. Mat.-Fiz.* 749 (1931).
4. F. R. Gantmakher, *The Theory of Matrices* (Nauka, Moscow, 1988), p. 390.

Translated by M. Skorikov

LOW-DIMENSIONAL
SYSTEMS

MBE Growth and Photoluminescent Properties of InAsSb/AlSbAs Quantum Wells

V. A. Solov'ev[^], Ya. V. Terent'ev*, A. A. Toropov*, B. Ya. Meltser*,
A. N. Semenov*, A. A. Sitnikova*, S. V. Ivanov*,
J. R. Meyer**, and P. S. Kop'ev*

* *Ioffe Physicotechnical Institute, Russian Academy of Sciences,
Politekhnikeskaya ul. 26, St. Petersburg, 194021 Russia*
[^]*e-mail: vasol@beam.ioffe.rssi.ru*

** *Naval Research Laboratory, Washington DC, DC 20375 USA*

Submitted May 16, 2002; accepted for publication May 17, 2002

Abstract—Heterostructures with a single InAs_{1-x}Sb_x/AlSb_{1-y}As_y quantum well (QW) on (001) GaSb substrates have been grown by MBE and studied using X-ray diffraction, transmission electron microscopy, and photoluminescence (PL) spectroscopy. High-intensity PL was observed at a temperature of 80 K, with a peak half-width of 30–50 meV and a peak wavelength in the range from 2 to 4.5 μm, depending on the QW width, which varied between 4 and 20 nm, respectively. The fundamental absorption edge of such QWs was calculated for a wide range of alloy compositions, x and y . Good correlation between the experimental and calculated dependences of the band gap on the InAsSb/AlSbAs QW thickness was obtained. © 2002 MAIK “Nauka/Interperiodica”.

1. INTRODUCTION

The semiconductor system InAsSb/AlSbAs offers promise for the design of mid-IR lasers (of 2–5 μm wavelength) [1, 2], because it combines the narrow (<0.4 eV) band gap of an InAsSb solid solution with the large conduction band offset at the interface. Further, when the content of Sb in InAsSb and As in AlSbAs is high enough, these solid solutions form a type-I heterojunction, in contrast to the binary compounds InAs and AlSb, forming a type-II heterojunction [3]. Varying the InAsSb and AlSbAs composition, it is possible to grow pseudomorphic quantum-confinement structures on both GaSb and InAs substrates.

This report is devoted to a systematic study of the morphology and photoluminescence (PL) of structures with a single InAs_{1-x}Sb_x/AlSb_{1-y}As_y quantum well (QW) in a wide range of compositions x and y and MBE-grown on (001) GaSb substrates. The fundamental absorption edge of a QW has been calculated in the effective mass approximation, using the Van de Walle method [4] to account for the elastic stresses in the layers. The calculated results correlate well with the PL data.

2. MBE GROWING

The samples were grown in a Riber 32P MBE machine with a standard As source supplying a flow of As₄ molecules and a cracking Sb source equipped with an additional high-temperature zone to allow the decomposition of Sb₄ molecules and produce a flow

with a predominance of Sb₂ molecules. To diminish the defect density in the active region of a structure, a 0.5-μm-thick GaSb buffer layer containing a 10-period superlattice in its middle, 10 × [Al_{0.5}Ga_{0.5}Sb (5 nm)/GaSb (5 nm)], was initially grown at the substrate temperature $T_S = 500^\circ\text{C}$. An InAs(Sb) QW confined between the top and bottom AlSbAs barriers of 23 and 38 nm thickness, respectively, and also a capping 5-nm thick GaSb layer were grown at a lower temperature (420°C), which is the optimal temperature for the fabrication of InAs and InAsSb layers with high luminescent properties [5]. The QW thickness was varied in the range of 4–20 nm. All the epitaxial layers were nominally undoped.

Previously, we found an effect from the unintentional incorporation of Sb atoms into InAs layers (with the Sb-source maintained at the operation temperature, but with its shutter closed). This effect is typical of the employed configuration of sources of volatile components and is presumably due to the essentially higher incorporation factor of Sb₂ molecules as compared with As₄ [6]. It was also shown that the Sb content in the formed InAs_{1-x}Sb_x solid solution is $x = 0.05$ for $T_S = 480^\circ\text{C}$. To estimate the Sb content in a QW, in the present study, a test structure of two InAs layers was grown on (001) InAs substrate. In this structure, a 0.25-μm-thick buffer layer was grown at $T_S = 480^\circ\text{C}$ and another 0.15-μm-thick InAs layer, at 420°C. The X-ray diffraction (XRD) rocking curve and the PL spectrum of this structure are presented in Figs. 1a and 1b, respectively. Along with the substrate peak ($\theta = 0$),

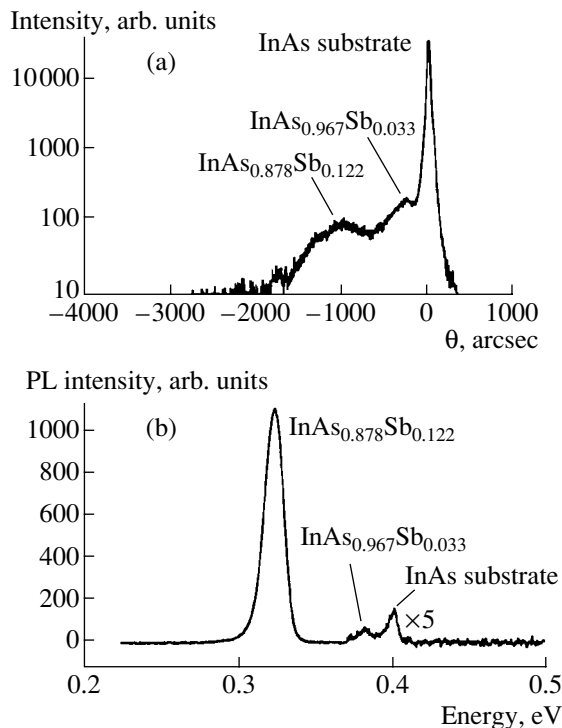


Fig. 1. (a) XRD double-crystal ($\theta - 2\theta$) rocking curve and (b) PL spectrum at $T = 77$ K for a structure containing two InAsSb layers.

the XRD rocking curve exhibits two peaks near the angles $\theta_1 = -1000''$ and $\theta_2 = -250''$, which is related to the diffraction from $\text{InAs}_{1-x_1}\text{Sb}_{x_1}$ and $\text{InAs}_{1-x_2}\text{Sb}_{x_2}$ layers grown at $T_S = 420$ and 480°C , respectively. Assuming that the layers are completely relaxed, the simulation of XRD curves yields $x_1 = 0.122$ and $x_2 = 0.033$. The PL spectrum (Fig. 1b) also shows the substrate peak (a photon energy $E_{\text{PL}} = 0.403$ eV) and two peaks with energies $E_{\text{PL}1} = 0.324$ eV and $E_{\text{PL}2} = 0.382$ eV. The Sb content in InAs layers estimated from the PL, with due account taken for the band bending (the bending parameter $C = 0.67$ eV [7]), is $x_1 = 0.114$ and $x_2 = 0.035$, which correlates well with the analysis of XRD data.

Thus, the presented results allow for the conclusion that InAs(Sb) QWs grown at $T_S = 420^\circ\text{C}$ contain $\sim 12\%$ Sb. It is necessary to note that the $\text{InAs}_{1-x}\text{Sb}_x$ solid solution is completely lattice-matched with GaSb at $x \approx 0.09$. Therefore, the lattice parameter of the QW material is larger, and the QW is subjected to compressive stress. As is known, effective compensation of elastic stresses in a structure as a whole is possible in multilayer structures by means of the alternate growing of layers with opposite stresses (compressive and tensile) [8]. In our case, such compensation is possible if AlSb is replaced in barriers by a ternary $\text{AlSb}_{1-y}\text{As}_y$ solid solution, where the lattice parameter decreases as the As content rises. It is noteworthy that this solid solu-

tion becomes completely lattice-matched with GaSb at $y \approx 0.08$. An addition of As to AlSb also enhances the band offsets at the QW interfaces and gradually transforms the InAsSb/AlSbAs heterojunction from type II to type I, as already mentioned above. To study the influence of the As content in barrier layers on the energy of optical emission from QWs experimentally, we have grown structures in which the $\text{AlSb}_{1-y}\text{As}_y$ composition varied in the range $y = 0.02-0.35$. To modify the composition of the solid solution, only the Sb flux was varied under constant Al, Ga, and As fluxes and growth temperature [6]. Assuming the absence of any relaxation of elastic stresses in the epitaxial layers, the average value of y was estimated from the angular position of the related peak of the XRD rocking curve.

3. STRUCTURAL STUDIES

A series of structures differing in their QW thickness were studied via cross-sectional transmission electron microscopy (TEM) using a Philips EM-420 setup with 100 kV accelerating voltage. As is known, (200) diffraction reflections are sensitive to variations in the chemical composition of materials with a face-centered cubic lattice and can be effectively used to visualize spatial fluctuations of the composition [9]. Figure 2 shows dark-field TEM images of samples with different QW thicknesses, which demonstrates the high quality and planarity of the layers.

4. OPTICAL STUDIES

Photoluminescence of the structures was measured at a temperature of 80 K. The PL was excited with a InGaAs diode laser operating in the CW mode at a 1.05- μm wavelength, and also with the 514-nm line of an Ar-ion laser. The pumping power density incident on the sample was ~ 2 W cm^{-2} . The PL signal was detected with a cooled InSb detector. High-intensity PL was observed during excitation with an Ar-ion laser, with the energy of quanta above the edge of the Γ band in the AlSbAs barriers (Fig. 3). The PL spectra contain two relatively narrow peaks, one of which (about 0.78 eV) corresponds to the edge PL in GaSb. The position of the second peak, with a half-width of 30–50 meV, varied in the wavelength range of 2–4.5 μm , depending on the QW thickness. It is necessary to note that the intensity of the PL peak related to the emission from the QW decreased drastically as a result of pumping with a laser of 1.05 μm wavelength; this indicates a subbarrier excitation mode, that is, the direct pumping of a thin QW.

Simultaneously with the experimental study, we performed calculations of the band gap value for InAsSb/AlSbAs QWs in a wide range of QW and barrier compositions and QW thicknesses. The calculations were performed via the effective mass approximation using a two-band model. The influence of elastic stresses on the band structure of solid solutions was taken into account in terms of the van de Walle theory [4].

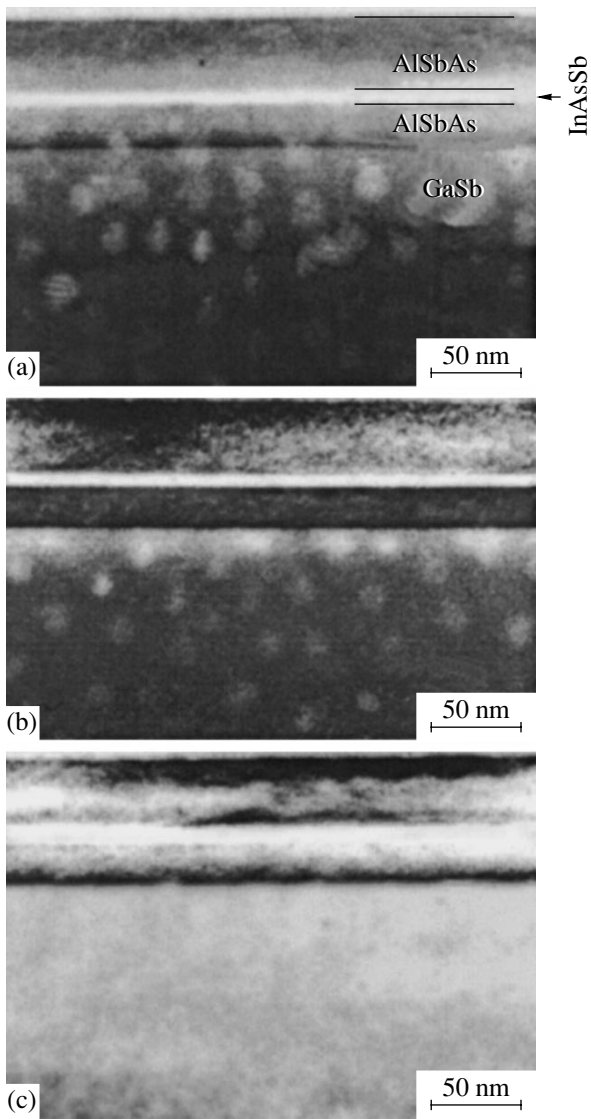


Fig. 2. Dark-field cross-sectional TEM images of structures containing an InAsSb QW of the thickness: (a) 4.8, (b) 6.2, and (c) 10 nm. The bright spotlike defects are artifacts formed during the ionic etching at the time of sample preparation.

According to the calculations, the offset of the conduction band at the interface exceeds 1.5 eV in the entire range of compositions under study [7]. The situation with the valence band is more complicated, because the valence band offset is considerably smaller, and the value and even the sign of this offset depend on the composition of both compounds ($\text{InAs}_{1-x}\text{Sb}_x$ and $\text{AlSb}_{1-y}\text{As}_y$). Figure 4 presents the energies of the top of heavy and light hole bands (solid and dashed lines, respectively) versus y for the $\text{AlSb}_{1-y}\text{As}_y$ solid solution. The pseudomorphic growth of a structure on GaSb substrate was assumed in the calculation. In the same figure, the corresponding data for $\text{InAs}_{0.88}\text{Sb}_{0.12}$ are shown. As seen in the figure, the type of the band structure changes at $y \approx 0.05\text{--}0.06$. At $y > 0.06$, an

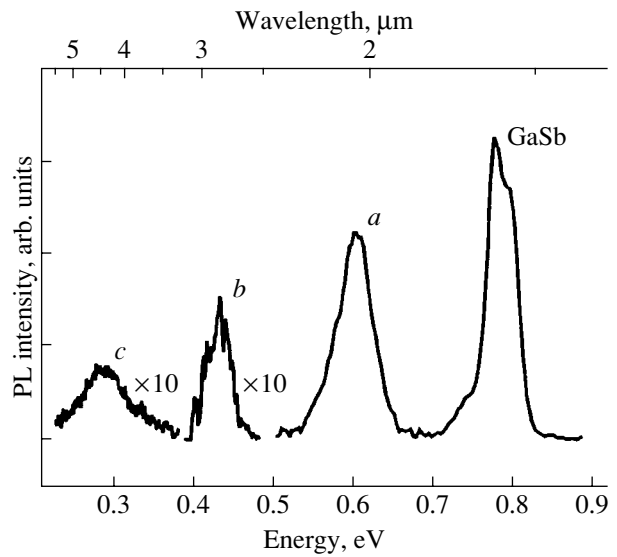


Fig. 3. PL spectra of $\text{InAs}_{0.88}\text{Sb}_{0.12}/\text{AlSb}_{1-y}\text{As}_y$ QW structures with well thickness and As content y in the barrier of, respectively, (a) 4.2 nm, 0.3; (b) 6.2 nm, 0.2; and (c) 14 nm, 0.03.

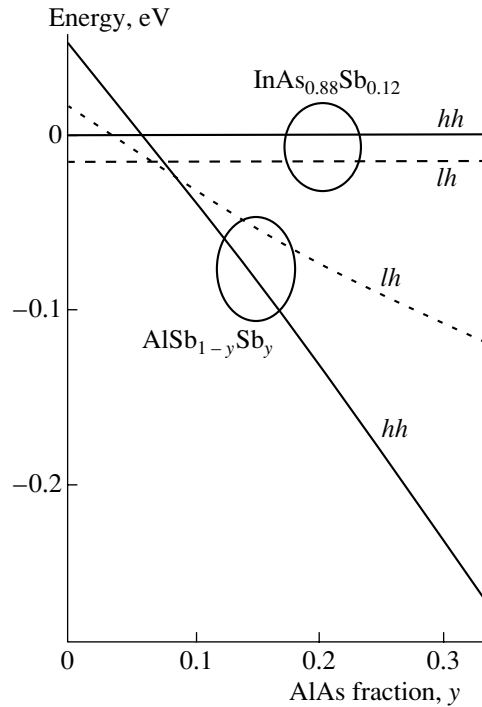


Fig. 4. Calculated positions of the valence band top in $\text{AlSb}_{1-y}\text{As}_y$ solid solution vs. the As content y for heavy and light holes ((solid and dashed lines, respectively). Horizontal lines indicate the corresponding values for $\text{InAs}_{0.88}\text{Sb}_{0.12}$. Stresses lift the degeneracy in the valence band of $\text{AlSb}_{1-y}\text{As}_y$, except for the case of matched lattices at $y \approx 0.08$.

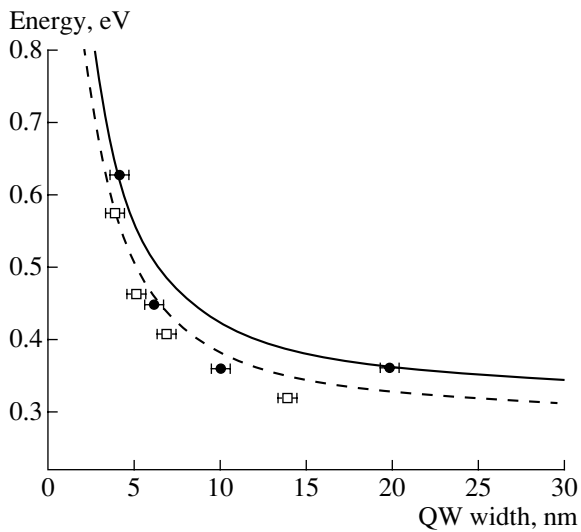


Fig. 5. Band gap of a single $\text{InAs}_{0.88}\text{Sb}_{0.12}/\text{AlSb}_{1-y}\text{As}_y$ QW vs. the well thickness: (lines) calculated and (points) experiment. Calculations for y of 0.02 (dashed line) and 0.3 (solid line). Experimental data: (squares) samples with low ($0.02 < y < 0.04$) As content in the barriers and (circles) those with high As content ($0.2 < y < 0.3$).

$\text{InAs}_{0.88}\text{Sb}_{0.12}/\text{AlSb}_{1-y}\text{As}_y$ QW exhibits a type-I band diagram; that is, electrons and holes are spatially localized in the same $\text{InAs}_{0.88}\text{Sb}_{0.12}$ layer. At $y < 0.05$, the valence band offset reverses its sign and the QW becomes type II. In this case, electrons are localized in the $\text{InAs}_{0.88}\text{Sb}_{0.12}$ layer, and holes, in the neighboring $\text{AlSb}_{1-y}\text{As}_y$ layers. It is necessary to note that, in both cases, the material with a higher energy of the valence band top ($\text{AlSb}_{1-y}\text{As}_y$ at $y < 0.05$ or $\text{InAs}_{0.88}\text{Sb}_{0.12}$ at $y > 0.06$) experiences compressive elastic stresses and, consequently, the heavy hole band becomes the lower state.

Figure 5 shows calculated dependences of the band gap (E_g) as a function of the thickness of the $\text{InAs}_{0.88}\text{Sb}_{0.12}/\text{AlSb}_{1-y}\text{As}_y$ QW for the extreme compositions of $\text{AlSb}_{1-y}\text{As}_y$ barriers: $y = 0.02$ (type-II heterojunction, dashed line) and $y = 0.3$ (type-I, solid line). It was established that, in spite of the band structure transformation from type II to type I and the slight improvement of the hole confinement as the As content in the $\text{AlSb}_{1-y}\text{As}_y$ barriers rises, the related shift of the optical transition energy is less than the experimentally observed half-width of the PL peak. The experimental values of the band gap in the QW were estimated from the PL data using the approach described in [10], where a semi-empirical relation $E_g = E_{\text{PL}} + 0.6\Delta E_{\text{PL}}$ was obtained (here, E_{PL} and ΔE_{PL} are the spectral position and half-width of the PL peak, respectively). Thus, the obtained E_g values are also shown in Fig. 5 as squares for structures with a low ($0.02 < y < 0.04$) arsenic content and as circles for structures with a high ($0.2 < y < 0.3$) arsenic content in the barriers. On the whole, these

data correlate well with the calculated dependences, showing somewhat lower E_g values for the samples with small y . It is also necessary to note that the PL intensity in the samples with a higher As content in the barriers was on average 3 times greater than that in the samples with small y . The results obtained show that the PL observed in these structures arises from interband optical transitions in the $\text{InAs}_{0.88}\text{Sb}_{0.12}/\text{AlSb}_{1-y}\text{As}_y$ QW, and they also validate the proposed model of the band structure and transformation of the heterojunction type in the heterostructures under study.

5. CONCLUSION

The results of structural and optical studies of $\text{InAs}_{1-x}\text{Sb}_x/\text{AlSb}_{1-y}\text{As}_y$ QW heterostructures grown by MBE on (001) GaSb substrates have been presented. The structures exhibit intense photoluminescence in the range of 2–4.5 μm , depending on the QW thickness. The calculation of the band offset at the $\text{InAs}_{1-x}\text{Sb}_x/\text{AlSb}_{1-y}\text{As}_y$ interface reveals a heterojunction transformation from type II to type I as the As content in the barriers rises, which is indirectly confirmed by the PL experimental data.

ACKNOWLEDGMENTS

We are grateful to M.V. Baïdakova for performing the XRD studies.

This study was supported by the Russian Foundation for Basic Research (project no. 01-02-17933) and CRDF (no. RP1-2265).

REFERENCES

1. S. J. Eglash and H. K. Choi, *Appl. Phys. Lett.* **64**, 833 (1994).
2. H. K. Choi, G. W. Turner, and Z. L. Liao, *Appl. Phys. Lett.* **65**, 2251 (1994).
3. B. Brar, H. Kroemer, J. Ibbetson, and J. H. English, *Appl. Phys. Lett.* **62**, 3303 (1993).
4. C. G. Van de Walle, *Phys. Rev. B* **39**, 1871 (1989).
5. A. Wilk, F. Genty, B. Fraisse, *et al.*, *J. Cryst. Growth* **223**, 341 (2001).
6. A. N. Semenov, V. A. Solov'ev, B. Ya. Mel'tser, *et al.*, in *Proceedings of the 9th International Symposium "Nanostructures: Physics and Technology"*, St. Petersburg, Russia, 2001, p. 78.
7. I. Vurgaftman, J. R. Meyer, and L. R. Ram-Mohan, *J. Appl. Phys.* **89**, 5815 (2001).
8. D. C. Houghton, M. Davies, and M. Dion, *Appl. Phys. Lett.* **64**, 505 (1994).
9. E. Bithnel and W. Stobbs, *Philos. Mag. A* **60**, 39 (1989).
10. K. P. Q'Donell, P. J. Parbrook, F. Yang, *et al.*, *Physica B (Amsterdam)* **191**, 45 (1993).

Translated by D. Mashovets

LOW-DIMENSIONAL
SYSTEMS

Weak Antilocalization and Spin–Orbit Interaction in a $\text{In}_{0.53}\text{Ga}_{0.47}\text{As}/\text{InP}$ Quantum Well in the Persistent Photoconductivity State

D. D. Bykanov*, S. V. Novikov, T. A. Polyanskaya, and I. G. Savel'ev

*Ioffe Physicotechnical Institute, Russian Academy of Sciences,
Politekhnicheskaya ul. 26, St. Petersburg, 194021 Russia*

*e-mail: dbyk@mail.ioffe.ru

Submitted June 10, 2002; accepted for publication June 17, 2002

Abstract—Low-field quantum magnetoresistance of two-dimensional electron gas at the $\text{In}_{0.53}\text{Ga}_{0.47}\text{As}/\text{InP}$ interface was studied in the persistent photoconductivity state. The sign-alternating property of the dependences of the magnetoresistance on the magnetic field indicates that the spin–orbit interaction affects the quantum well conductivity. The mechanism caused by the electric field built in at the interface was shown to contribute dominantly to the spin–orbit scattering frequency $1/\tau_{\text{so}}$. This is the Rashba mechanism, which is linear in the electron wave vector. These data allowed us to estimate the parameters of spin–orbit splitting of the energy spectrum as $\alpha = (84 \pm 10) \text{ \AA}^2$ (by the Rashba mechanism) and $\gamma = (73 \pm 5) \text{ eV \AA}^3$ (by the Dyakonov–Perel and Dresselhaus mechanisms). © 2002 MAIK “Nauka/Interperiodica”.

1. INTRODUCTION

As is known, classical (Lorentzian) magnetoresistance is absent in semiconductors and semiconductor structures with two-dimensional electron gas (2DEG) at a low (liquid-helium) temperature. The magnetoresistance exponentially increasing with the magnetic field is observed instead of classical magnetoresistance at the insulator side of the metal–insulator transition in the region of low temperatures. This magnetoresistance is caused by spin transformation of the Hubbard bands [1] or by contraction of electron wave functions [2]. The absence of the Lorentzian magnetoresistance at the metal side of the transition is caused by electron gas degeneracy [3]. Instead of this, the quantum negative magnetoresistance (NMR) is observed in a weak magnetic field at $\omega_c \tau \ll 1$, where ω_c is the cyclotron frequency and τ is the transport time (time of the electron momentum relaxation). This is caused by suppression of the weak localization effect by the magnetic field and a corresponding increase in the conductivity [4]. The positive quantum magnetoresistance caused by another type of quantum corrections to the conductivity manifests itself in a stronger magnetic field. These corrections are related to the modified electron–electron interaction characteristic of conductors with disordered electron gas [4–7]. At $\omega_c \tau \gg 1$, Shubnikov–de Haas oscillations set in.

The conductivity decrease in the absence of a magnetic field (weak localization) is caused by the interference of wave functions of electrons that passed the same path in forward and backward directions. This interference depends on the total spin J of two electron

waves. During spin–orbit (SO) interaction, only interference of the waves with $J = 1$ in the triplet state yields the weak localization effect and thus reduces the conductivity. The singlet state of interfering waves with the total number $J = 0$ causes an increase in the conductivity (the antilocalization effect). Hence, suppression of interference of waves with $J = 1$ and 0 by the magnetic field increases the negative-magnetoresistance effect and decreases the conductivity, respectively. In the latter case, weak antilocalization is suppressed, which results in positive magnetoresistance.

In the first studies concerned with the theory of weak localization and antilocalization, the times τ_ϕ and τ_{so} of the dephasing of an electron wave function were considered as the parameters defining the dependences of the magnetoresistance on the magnetic field. The former time (τ_ϕ) corresponds to the dephasing due to inelastic scattering related to the electron–electron or electron–phonon interactions. The latter time (τ_{so}) corresponds to the dephasing due to SO scattering of electrons. It was assumed that τ_{so} is controlled only by the SO interaction mechanism. As the process controlling τ_{so} , the Elliot–Yafet spin relaxation mechanism [8] or the Dyakonov–Perel mechanism (often referred to as the Dresselhaus mechanism) arising in semiconductors without a center of inversion [4, 9] were considered. Later on, several theoretical studies showed that, if there are several SO interaction mechanisms, they have different effects on the dependence of the 2DEG conductivity on the magnetic field [10, 11]. A new type of dependence was suggested in order to take into account these different effects. As a result, an analysis of the

experimental dependences allowed for a separate estimation of the contributions of different SO scattering mechanisms.

In this paper, we report the results of studying 2DEG magnetoresistance at the $\text{In}_{0.53}\text{Ga}_{0.47}\text{As}/\text{InP}$ heteroboundary in the case when one subband of size quantization is populated in the persistent conductivity state and compare these results with theory [10, 11]. Previously, such an experimental study was carried out for 2DEG at the $\text{GaAs}/\text{In}_{0.15}\text{Ga}_{0.85}\text{As}$ heteroboundary using samples in the equilibrium state (in the dark) [11].

2. THEORETICAL PREMISES

The theory of quantum corrections is valid for a weakly disordered electron gas if the following condition is met:

$$k_{\text{F}}l > 1. \quad (1)$$

Here, k_{F} is the wave vector of an electron at the Fermi level and l is the free path length. The theoretical dependences of the magnetoconductivity on the magnetic field are valid only up to the magnetic field corresponding to the inequality

$$L_{\text{B}} > l, \quad (1a)$$

where $L_{\text{B}} = (\hbar c/2eB)^{1/2}$ is the magnetic length.

The sign-alternating dependence of the quantum magnetoresistance may be illustrated using the theoretical dependence of the 2DEG magnetoconductivity on the magnetic field (see [8])

$$\begin{aligned} \frac{\sigma(B) - \sigma(0)}{G_0} = \frac{\Delta\sigma(B)}{G_0} = f_2\left(\frac{B}{H_s + H_\phi}\right) \\ + \frac{1}{2}f_2\left(\frac{B}{2H_s + H_\phi}\right) - \frac{1}{2}(1 + \beta)f_2\left(\frac{B}{H_\phi}\right), \end{aligned} \quad (2)$$

where B is the magnetic field, $G_0 = e^2/2\pi\hbar$, and β is the coefficient defining the Mackey–Thompson correction (see [12]),

$$\Delta\sigma_{\text{MT}}(B) = -\beta G_0 f_2\left(\frac{B}{H_\phi}\right); \quad (3)$$

the function $f_2(x)$ is defined by the diagram function $\Psi(z)$:

$$f_2(x) = \Psi\left(\frac{1}{2} + \frac{1}{x}\right) + \ln x.$$

The parameter H_ϕ is related to the SO dephasing time as

$$H_\phi = \frac{\hbar c}{4eD\tau_\phi}; \quad (4)$$

the parameter H_s is related to the relaxation time τ_{so} of SO interactions as

$$H_s = \frac{\hbar c}{4eD\tau_{\text{so}}}. \quad (5)$$

If the frequency $1/\tau_{\text{so}}$ of SO scattering is much lower than the frequency $1/\tau_\phi$, we have $2/H_s + H_\phi \approx H_\phi$ and, summing the terms on the right-hand side of (2), we arrive at

$$\frac{\Delta\sigma(B)}{G_0} = (1 - \beta)f_2\left(\frac{B}{H_\phi}\right) > 0;$$

i.e., the quantum correction to the conductivity is positive and negative magnetoresistance is observed, controlled by the dephasing time.

Hereafter, as in most of the theoretical [10, 11] and experimental studies, we neglect the Mackey–Thompson correction (3), assuming that $\beta \rightarrow 0$.

For semiconductors with a strong SO interaction of electrons, e.g., p -type IV and III–V semiconductors, as well as for quantum wells (QWs) based on hole conduction, the inverse inequality $1/\tau_{\text{so}} \gg 1/\tau_\phi$ is valid, i.e.,

$$H_s \ll H_\phi, \quad (6)$$

and a dominant role is played by the last term on the right-hand side of (2). The quantum correction to the conductivity becomes negative; i.e., positive magnetoresistance is observed. This effect, as well as negative magnetoresistance, is defined only by the value and temperature dependence of τ_ϕ ,

$$\frac{\Delta\sigma(B)}{G_0} = -\frac{1}{2}f_2\left(\frac{B}{H_\phi}\right) < 0. \quad (7)$$

If the frequencies $1/\tau_{\text{so}}$ and $1/\tau_\phi$ are comparable in magnitude, we have

$$H_s \gtrsim H_\phi \quad (8)$$

and the last term on the right-hand side of (2) with a larger argument also plays a dominant role in the weak magnetic field, maintaining the positive magnetoresistance. As the magnetic field increases and as this dependence is flattened, the first terms begin to prevail and the magnetoconductivity changes its sign, while the magnetoresistance becomes negative. This sign-alternating magnetoresistance can be observed in the III–V-based structures with 2DEG (see, e.g., [9, 11, 13]). It manifests itself as a peak of the positive magnetoresistance in the region of a weak magnetic field with a sign reversal and a transition to the negative magnetoresistance.

As was shown in [10], dependence (2) should be changed if the Hamiltonian

$$H = \frac{k^2}{2m^*} + (\boldsymbol{\sigma}\boldsymbol{\Omega}) \quad (9)$$

for spin splitting of the conduction band includes linear (with respect to k) terms describing the SO interaction (the heteroboundary plane [100] in III–V was considered). In Eq. (9), $\hbar = 1$, $k^2 = k_x^2 + k_y^2$, $\boldsymbol{\sigma} = (\sigma_x, \sigma_y)$, $\boldsymbol{\Omega} = (\Omega_x, \Omega_y)$ are the two-dimensional vectors with components in the QW plane, and σ_i are elements of the Pauli matrix. The vector $2\boldsymbol{\Omega}/\hbar$ has a physical meaning of the precession vector: its length is equal to the spin precession frequency, and its direction defines the precession axis. The spin-related energy splitting is 2Ω .

In the case under consideration, the spin relaxation time is calculated as

$$\frac{1}{\tau_{so}} = 2(\Omega_1^2\tau_1 + \Omega_{1R}^2\tau_1 + \Omega_3^2\tau_3), \quad (10)$$

where

$$\frac{1}{\tau_n} = \int W(\theta)(1 - \cos n\theta)d\theta, \quad n = 1, 3; \quad (11)$$

$$\Omega_1 = \gamma k \left(\langle k_z^2 \rangle - \frac{1}{4}k^2 \right)$$

is the term linear with respect to the wave vector (the Dyakonov–Perel mechanism) [14]. Here, $\langle k_z^2 \rangle$ is the mean squared wave vector in the direction perpendicular to the 2DEG plane.

$$\Omega_3 = \gamma \frac{k^3}{4} \quad (12)$$

is a cubic term with respect to the wave vector in the heteroboundary plane (the Dresselhaus mechanism). Hereafter, we designate the transport relaxation time as $\tau_1 = \tau$. It is noteworthy that magnetoconductivity expression (2) is valid only if Ω_3 contributes to SO scattering.

Furthermore, in the case of an asymmetric QW, an additional term suggested by Rashba [15] arises in the Hamiltonian,

$$\Omega_{1R} = \alpha Fk \quad (13)$$

(F is the electric field at the heteroboundary); this term is also linear with respect to the electron wave vector. The coefficients α and γ are the constants characterizing the energy spectrum of a semiconductor with a 2DEG layer.

Theoretical analysis [10] showed that it is incorrect to employ merely the total time for the spin relaxation in expression (2) in order to take into account the linear terms related to weak localization when calculating the

quantum corrections. In [10], the magnetoconductivity expression was written as

$$\frac{\Delta\sigma(B)}{G_0} = -\frac{1}{a_0} - \frac{2a_0 + 1 + \frac{H_s}{B}}{a_1 \left(a_0 + \frac{H_s}{B} \right) - 2\frac{H_{s1}}{B}} + \sum_{n=0}^{\infty} \left(\frac{3}{n} - \frac{3a_n^2 + 2a_n \frac{H_s}{B} - 1 - 2(2n+1) \frac{H_{s1}}{B}}{\left(a_n + \frac{H_s}{B} \right) a_{n-1} a_{n+1} - 2((2n+1)a_n - 1) \frac{H_{s1}}{B}} \right) - 2 \ln \frac{H_{tr}}{B} - \Psi \left(\frac{1}{2} + \frac{H_\phi}{B} \right) - 3C, \quad (14)$$

where $a_n = n + \frac{1}{2} + \frac{H_\phi}{B} + \frac{H_s}{B}$ and C is the Euler constant. In contrast to (2), formula (14) incorporates two characteristic magnetic fields to describe the SO scattering: apart from H_s , defined by the total relaxation time τ_{so} (10) of the spin,

$$H_s = \frac{2}{4\hbar eD} (\Omega_1^2\tau + \Omega_3^2\tau_3 + \Omega_{1R}^2\tau), \quad (15)$$

an additional parameter H_{s1} arises, defined by the largest term of (11) or (13), which are linear with respect to the wave vector

$$H_{s1} = \frac{2\tau \max\{\Omega_1^2, \Omega_{1R}^2\}}{4\hbar eD}. \quad (16)$$

The condition (1a) for the applicability of all the theoretical dependences of the magnetoconductivity on the magnetic field for 2DEG may be written as

$$B < H_{tr} = \frac{\hbar c}{4eD\tau}. \quad (16a)$$

3. EXPERIMENTAL

Selectively doped $\text{In}_{0.53}\text{Ga}_{0.47}\text{As}/\text{InP}$ heterostructures were produced by liquid-phase epitaxy [16]. A p -type Sm-doped InP buffer layer (with a hole concentration $p \approx 10^{15} \text{ cm}^{-3}$ at room temperature) about $1.5 \mu\text{m}$ thick was grown on a substrate of semi-insulating Fe-doped InP. Then, an Si-doped ($N_{\text{Si}} \approx (2-3) \times 10^{17} \text{ cm}^{-3}$) n -InP layer $0.5-0.6 \mu\text{m}$ thick was grown (as an electron source in the QW), as was a p -type $\text{In}_{0.53}\text{Ga}_{0.47}\text{As}$ solid-solution layer $4-5 \mu\text{m}$ thick with a hole concentration $p \approx 10^{15} \text{ cm}^{-3}$. These structures were used to produce (by photolithography) samples shaped as double Hall crosses with six contacts and intended for galvanomagnetic measurements. Indium drops were fused onto contact pads of the samples in vacuum at 450°C to ensure an ohmic contact with the 2DEG layer. The electron concentration in the samples was varied by light pulses of a GaAs light-emitting diode

Table 1. Parameters of the samples in the equilibrium state at $T = 1.8$ K

Sample	R, Ω	$n_s, 10^{11} \text{ cm}^{-2}$	$\mu, 10^4 \text{ cm}^2(\text{V s})^{-1}$	τ, ps	H_{tr}, G	$k_F l$
1	552	2.93	3.86	0.90	28	47
2	649	4.06	2.37	0.55	53	40
3	717	3.38	2.573	0.60	54	36

Note: R is the resistance per film area, n_s and μ are the Hall concentration and mobility of electrons, τ is the elastic-scattering time, H_{tr} is parameter (16a), and $k_F l$ is parameter (1).

(LED) using the persistent photoconductivity effect (nonequilibrium, but a quasi-steady process), which is accompanied by charge redistribution and a decrease in the built-in electric field at the heteroboundary [17]. The chemical potential ε_F was located in the first subband of size quantization in the range of concentration variation in the samples.

The measurements were carried out in the range $T = 1.8$ – 4.2 K using samples with an initial 2DEG concentration from $n_s = 2.9 \times 10^{11}$ to $n_s = 4.1 \times 10^{11} \text{ cm}^{-2}$. The

technique used for taking galvanomagnetic measurements was described elsewhere [18]. The 2DEG parameters at $T = 1.8$ K are listed in Table 1.

4. RESULTS AND ANALYSIS

The dependences of the sign-alternating magnetoresistance on the magnetic field B were measured in weak magnetic fields for all the sample states (both in the dark and under illumination); positive magnetoresistance was observed at $B < 50$ G and had a maximum. Figure 1 displays examples of such dependences of the magnetoresistance $[R(B) - R(0)]/R(0) = \Delta R/R_0$ on the magnetic field. The dependence $\Delta R/R_0 = f(B)$ was recalculated into the dependence of the magnetoconductivity on the magnetic field, $[\sigma(B) - \sigma(0)] = \Delta\sigma(B)$, which was normalized to the value $G_0 = e^2/2\pi\hbar$ in the following way:

$$\frac{\sigma(B) - \sigma(0)}{G_0} = \frac{\Delta\sigma(B)}{G_0} = -\frac{\sigma_0}{G_0} \left[\frac{\Delta R(B)}{R_0} + \left(\frac{\sigma_{xy}(B)}{\sigma_{xx}(B)} \right)^2 \right].$$

Here,

$$\left(\frac{\sigma_{xy}(B)}{\sigma_{xx}(B)} \right)^2 \approx (\mu H)^2$$

and μ is the Hall mobility. It was assumed that $(\mu H)^2 \ll 1$ in a weak magnetic field, but it can be comparable in magnitude to the values $\Delta R(B)/R_0$. The dependences obtained in such a manner (see Fig. 2) were compared to the theoretical one (14) to determine the parameters H_ϕ (4), H_s (15), and H_{s1} (16).

Figure 1a displays the data for one of the samples in the initial state as the temperature varies; Fig. 1b and Fig. 2 show the data for different 2DEG concentrations varied by illuminating the sample with pulses of the GaAs LED. Figure 2 (solid lines) also displays the theoretical dependences (14) that best fit the experimental data.

The obtained values of H_ϕ were used to determine the dephasing time τ_ϕ according to relation (4). The diffusivity was calculated as

$$D = \frac{\sigma}{e^2 \nu} = \frac{\hbar}{m^* 2\pi G_0 R_0},$$

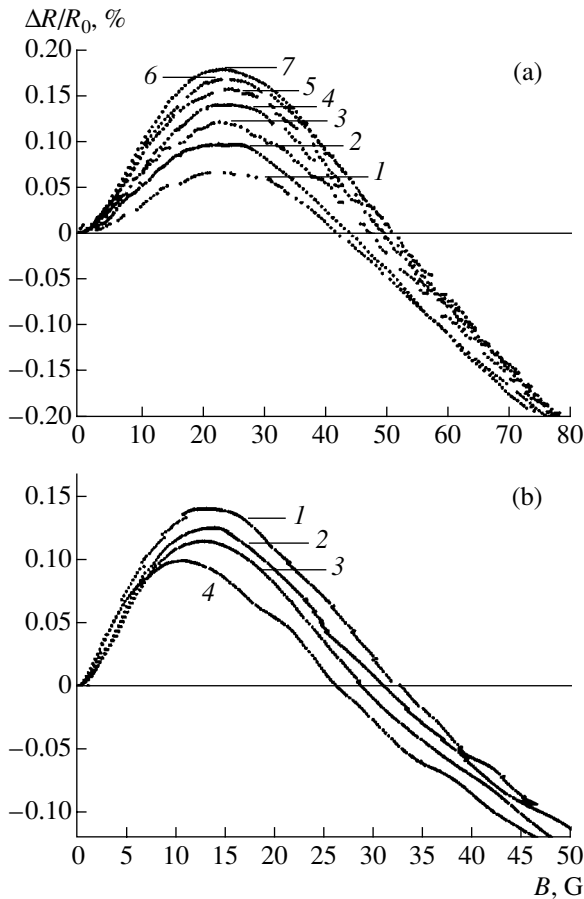


Fig. 1. Dependences of the magnetoresistance $\Delta R/R_0$ on the magnetic field B for samples 3 (a) and 1 (b) (see Table 1) at (a) the temperatures $T = 4.21$ (1), 3.74 (2), 3.27 (3), 2.78 (4), 2.45 (5), 1.99 (6), and 1.81 (7) K and (b) the electron densities n_s (10^{11} cm^{-3}) = 2.93 (1), 3.08 (2), 3.103 (3), and 3.202 (4).

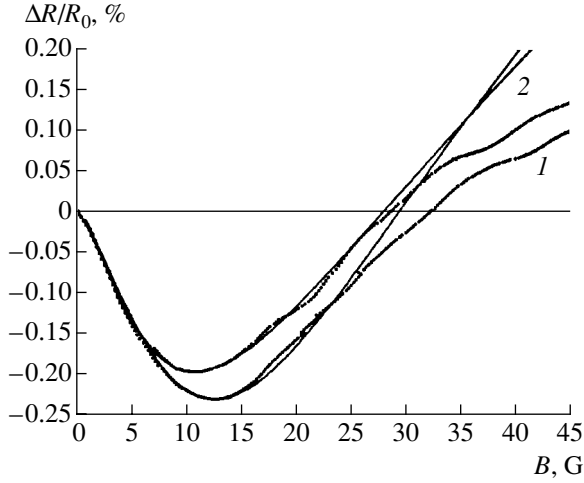


Fig. 2. Dependences of the magnetoconductivity $\Delta\sigma/G_0$ on the magnetic field B for sample 1 (see Table 1) at the electron density n_s (10^{11} cm^{-3}) = 3.14 (1) and 3.20 (2). Solid lines are the fitted theoretical dependences (14).

where v is the density of 2DEG states. The experimental dephasing frequencies $1/\tau_\phi$ are shown by points in the temperature (Fig. 3) and electron-density (Fig. 4) dependences of $1/\tau_\phi$.

Before comparing these results with theoretical data, we note that, as was shown in our previous papers (e.g., [19]), the relaxation of the wave function phase in the main band of III-V-based heterostructures at the liquid-helium temperature is controlled by electron-electron interaction. The first type of such an interaction, characteristic of weakly disordered conductors, is defined by the so-called Nyquist time [20]

$$\frac{\hbar}{\tau_d^{ee}} = \frac{2\pi G_0}{\sigma} T \ln\left(\frac{\sigma}{2\pi G_0}\right). \quad (17)$$

The other interaction type is characteristic of a perfect Fermi liquid. For 2DEG, the corresponding time is given by (see [21])

$$\frac{\hbar}{\tau_p^{ee}} = \frac{\pi T^2}{2\varepsilon_F} \ln\left(\frac{\varepsilon_F}{T_M}\right), \quad T_M = \max\left(\frac{\hbar}{\tau}, T\right).$$

With the constraint $T < \hbar/\tau$, we have $T_M = \hbar/\tau$. Then,

$$\frac{\hbar}{\tau_p^{ee}} = \frac{\pi T^2}{2\varepsilon_F} \ln\left(\frac{\sigma}{2\pi G_0}\right). \quad (18)$$

The sum frequency of the electron-electron interaction is calculated on the basis of the measured sample conductivities σ and electron densities n_s as

$$\frac{1}{\tau_\phi^{ee}} = \frac{1}{\tau_d^{ee}} + \frac{1}{\tau_p^{ee}}. \quad (19)$$

Figures 3 and 4 also show the theoretical dependences of the times $1/\tau^{ee}$ (17)–(19) on the temperature

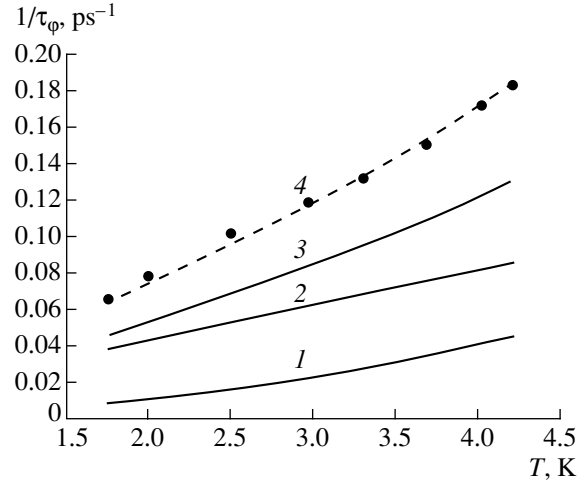


Fig. 3. Temperature dependences of the dephasing frequency $1/\tau_\phi$ for sample 3 in the equilibrium state. The experimental data (points) were obtained by comparison of the dependences $\Delta\sigma(B)/G_0$ with expression (14). The theoretical dependences of $1/\tau_p^{ee}$ (1), $1/\tau_d^{ee}$ (2), and $1/\tau_\phi^{ee}$ (3) correspond to (18), (17), and (19), respectively; curve 4 is for $1.5/\tau_\phi^{ee}$.

and electron density. One can see that there is qualitative agreement between the calculated $1/\tau_\phi^{ee}$ and experimental $1/\tau_\phi$ dependences on n_s and T . The quantitative disagreement of theory with the numerical values τ_ϕ (within 50%) in the case under consideration (see dashed curves 4 in Figs. 3 and 4) is observed rather frequently when comparing experimental and calculated values (see [6], Subsection 4.2).

The dephasing of the electron wave function can also be caused by inelastic electron-phonon scattering.

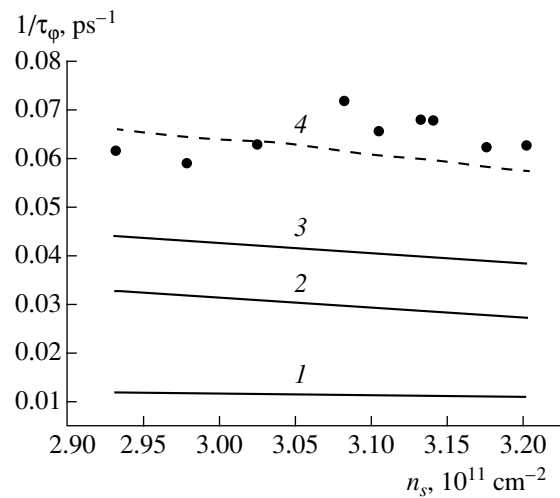


Fig. 4. Dependences of the dephasing frequency $1/\tau_\phi$ on the electron density n_s in the persistent-conductivity state. The same notation as in Fig. 3 is used.

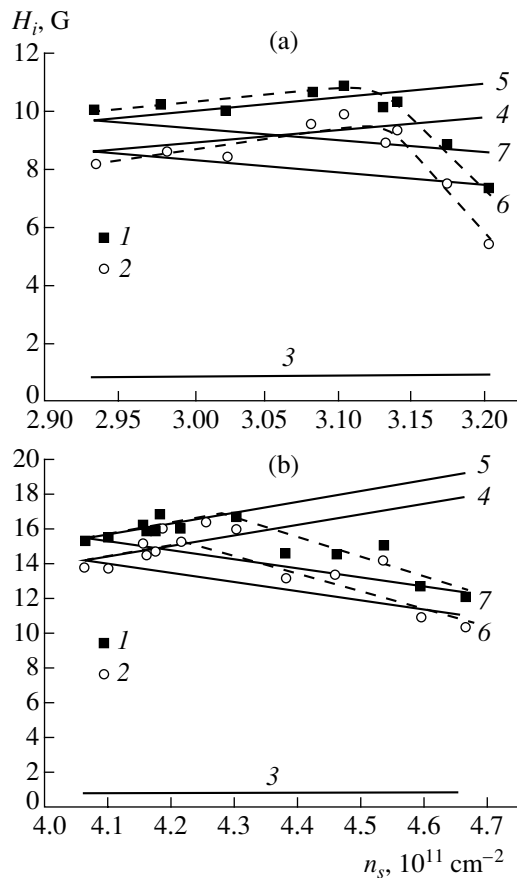


Fig. 5. Parameters of the spin-orbit interaction versus the 2DEG concentration in the persistent-conductivity state for samples 1 (a) and 2 (b) (see Table 1). The experimental values ((1) H_s (15) and (2) H_{s1} (16)) were obtained by comparison of the dependences $\Delta\sigma(B)/G_0$ with expression (14). Dashed curves are plotted by estimation through the experimental points. The theoretical dependences correspond to (3) H_{s3D} (23), (4) H_{s1D} (20), (5) $H_{s1D} + H_{s3D} + H_{s1R}$, (6) H_{s1R}^{pp} (25), and (7) $H_{s1D} + H_{s3D} + H_{s1R}^{pp}$.

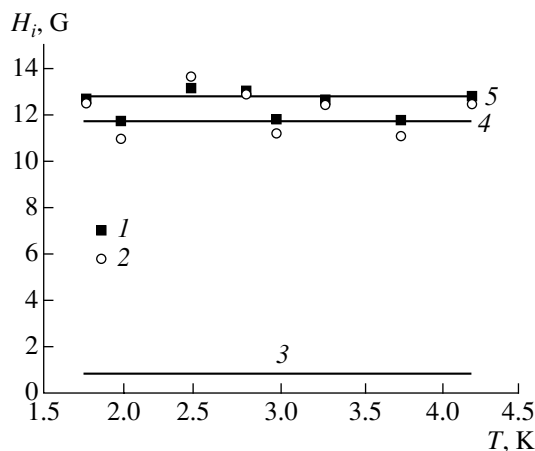


Fig. 6. Parameters of the spin-orbit interaction versus the temperature for sample 3 in the equilibrium state. The same notation as in Fig. 5 is used.

To estimate theoretically the corresponding frequency, we used the relaxation time of the average electron energy in the case of scattering under the deformation (DA) and piezoelectric (PA) potential of acoustical phonons. The corresponding equations (based on the Karpus theory [22]) are presented, e.g., in [23] (Subsection 4.3.2). As a result, it turns out that the frequency of electron-phonon interactions when there is DA scattering varies from $\sim 0.004 \text{ ps}^{-1}$ at $T = 1.8 \text{ K}$ to $\sim 0.01 \text{ ps}^{-1}$ at $T = 4.2$ for all the samples. The frequency of the PA electron-phonon interaction is even lower (by an order of magnitude). Hence, these mechanisms of inelastic scattering are virtually unimportant in the course of dephasing in the temperature and electron density ranges under consideration.

Thus, as the lower subband of size quantization is populated in the persistent photoconductivity state (under exposure to light pulses), the dephasing time τ_ϕ is controlled, as in the steady state (Fig. 3), by the electron-electron interaction time (19).

Figures 5 and 6 (points 1 and 2) show the values of $H_s(n_s)$, $H_s(T)$ and $H_{s1}(n_s)$, $H_{s1}(T)$ determined from comparison of the experimental dependences of the magnetoconductivity on the magnetic field with expression (14).

The concentration dependences of these parameters in the persistent conductivity state (Fig. 5) are qualitatively similar to those observed in [18, 24] for the values H_s . However, we emphasize that the data of [18, 24] on the dependences $H_s(n_s)$ and $H_\phi(n_s)$ in the first subband of size quantization are qualitative since they were processed using theoretical dependence (2), which is, in general, valid only for the mechanism of SO scattering (12). More comprehensive measurements and an analysis carried out in this study on the basis of the theory in (14) show that the SO-interaction parameters H_s and H_{s1} do not decrease immediately as the electron density increases: when they are first exposed to light, these parameters continue to increase slightly with n_s and then decrease.

The temperature dependences (see Fig. 6) were measured using a sample in the equilibrium state. As expected, the parameters H_s and H_{s1} characterizing SO scattering are independent of temperature (to within the experimental error).

As is evident from Figs. 5 and 6, the experimental values of H_{s1} are close in magnitude to the values of H_s . This means that the last term in sum (15) has a dominant role; i.e., the experimental values of H_{s1} (16) are defined by the Rashba mechanism,

$$H_{s1} = \frac{2\tau\Omega_{1R}^2}{4\hbar eD}.$$

For comparison with the theory, the parameters H_s (15) and H_{s1} (16) were calculated as follows. The value $\langle k_z^2 \rangle$ was determined as (see [25])

$$\langle k_z^2 \rangle = \left[\frac{48\pi m^* e^2 \left(N_0 + \frac{11}{32} n_s \right)}{\chi \hbar^2} \right]^{2/3}.$$

In the calculations, the dielectric constant, effective electron mass, and the residual-impurity concentration were taken as $\chi = 14.1$, $m^* = 0.0141m_0$, and $N_0 = 5 \times 10^{10} \text{ cm}^{-2}$, respectively. As a result, we obtain the following expression for H_{s1D} , defined by Ω_1^2 (11):

$$H_{s1D} = 1.132 \times 10^7 \gamma^2 \left(\frac{m^*}{m_0} \right)^2 \times \left\{ 0.0233 \left[\frac{m^*}{m_0} \frac{1}{\chi} \frac{\left(N_0 + \frac{11}{32} n_s \right)}{10^{12}} \right]^{2/3} - 1.57 \times 10^{-4} \frac{n_s}{10^{12}} \right\}^2. \quad (20)$$

Hereinafter, the substitution $k = k_F = (2\pi n_s)^{1/2}$ is used, the unit of concentration is cm^{-2} , and the coefficient γ is expressed in $\text{\AA}^3 \text{ eV}$.

Another term which is linear with respect to k , defined by Ω_{1R}^2 (13) and characteristic of an asymmetric QW, is written as

$$H_{s1R} = 3710\alpha^2 \left(\frac{m^*}{m_0} \right)^2 \frac{1}{\chi^2} \left(\frac{\frac{1}{2} n_s + N_0}{10^{12}} \right)^2. \quad (21)$$

The coefficient α is expressed in \AA^2 . Here, we used the following expression for the mean electric field of the QW (see [25]):

$$F = \frac{4\pi e \left(N_0 + \frac{1}{2} n_s \right)}{\chi}. \quad (22)$$

The Dresselhaus term, which is cubic with respect to the wave vector k and is defined by Ω_3^2 (12), yields the following expression for the SO scattering parameter:

$$H_{s3D} = 0.283\gamma^2 \frac{\tau_3}{\tau} \left(\frac{m^*}{m_0} \right)^2 \left(\frac{n_s}{10^{12}} \right)^2. \quad (23)$$

Hereafter, we assume that $\tau_3/\tau = 1$.

The parameters calculated using (20) and (21) are shown in Figs. 5 and 6 by curves 3 and 4, respectively. Curves 5 correspond to the calculated dependences $H_s = H_{s1D} + H_{s3D} + H_{s1R}$ (15) on the concentration n_s . The constants $\gamma = (73 \pm 5) \text{\AA}^3 \text{ eV}$ and $\alpha = (84 \pm 10) \text{\AA}^2$ were used in these calculations.

Figure 5 also displays the parameters H_{s1R} calculated for the nonequilibrium mode (H_{s1R}^{PP}). The persistent photoconductivity in the structures under study is caused by separation of carriers by the built-in electric field F , hole capture by residual ionized acceptors in the $\text{In}_{0.35}\text{Ga}_{0.46}\text{As}$ narrow-gap layer, and capture by surface states if the upper layer is thin [17]. This means that, if the value n_s is increased by Δn_s when the system is exposed to interband-absorption light, the concentration N_0 simultaneously decreases by the same value. Therefore, the mean field in the persistent-photoconductivity state can be written as

$$F = F_0 - \frac{4\pi e}{2\chi} \Delta n_s, \quad (24)$$

and the parameter of SO scattering according to the Rashba mechanism in the persistent-photoconductivity state is given by

$$H_{s1R}^{\text{PP}} = 3710\alpha^2 \left(\frac{m^*}{m_0} \right)^2 \frac{1}{\chi^2} \left(\frac{N_0 + n_{s0} - \frac{1}{2} n_s}{10^{12}} \right)^2, \quad (25)$$

where F_0 and n_{s0} are the built-in field (22) of the heterostructure and the electron density in the initial state, and n_s is the electron density in the persistent-conductivity state. The concentration dependences of H_{s1R}^{PP} calculated by (25) and of the sums $H_{s1D} + H_{s3D} + H_{s1R}^{\text{PP}}$ are shown in Fig. 5 by curves 6 and 7, respectively. Such a calculation of H_{s1R}^{PP} allows only a qualitative explanation of the run of the experimentally determined parameters $H_{s1} = H_{s1R}^{\text{PP}}$ and $H_{s1} \approx H_{s1R}^{\text{PP}}$ in relation to the electron density, which increases with the number of illumination pulses (cf. points 2 with curves 6 and points 1 with curves 7 in Fig. 5).

The constants α and γ may be rather roughly estimated by linear extrapolation of the parameters (see [11]) of the three-band $\mathbf{k} \cdot \mathbf{p}$ model of energy bands for $\text{In}_x\text{Ga}_{1-x}\text{As}$ compounds at $x = 0, 0.15$, and 1 to determine the values at $x = 0.53$ (see Table 2), as well as the $\mathbf{k} \cdot \mathbf{p}$ -model formulas (see [11]); i.e.,

$$\gamma = -\frac{4}{3} \frac{PP'Q}{E_g(E_g' + \Delta')} \left(\frac{\Delta}{E_g + \Delta} + \frac{\Delta'}{E_g'} \right),$$

$$\alpha = \frac{2}{3} \left\{ P^2 \frac{\Delta}{E_g(E_g + \Delta) \left(E_g + \frac{1}{3} \Delta \right)} + P'^2 \frac{\Delta'}{E_g'(E_g' + \Delta') \left(E_g' + \frac{2}{3} \Delta' \right)} \right\}.$$

Table 2. Band structure parameters of GaAs, InAs, $\text{In}_{0.15}\text{Ga}_{0.85}\text{As}$, and $\text{In}_{0.53}\text{Ga}_{0.47}\text{As}$ determined experimentally and calculated according to the $\mathbf{k} \cdot \mathbf{p}$ model

Band structure parameters	Data of [11]			This study		
	$\mathbf{k} \cdot \mathbf{p}$			Experiment	$\mathbf{k} \cdot \mathbf{p}$	Experiment
	GaAs	InAs	$\text{In}_{0.15}\text{Ga}_{0.85}\text{As}$	$\text{In}_{0.53}\text{Ga}_{0.47}\text{As}$		
E_g , eV	1.519	0.42	1.35		0.8215	
Δ , eV	0.341	0.38	0.347		0.362	
E'_g , eV	2.97	3.97	3.12'		3.49	
Δ' , eV	0.171	0.24	0.181		0.207	
P , eV Å	10.49	9.2'	10.29		9.81	
P' , eV Å	4.78	0.87'	4.20		2.80	
Q , eV Å	-8.16	-8.33	-8.18		-8.24	
γ , eV Å ³	27.5	26.9	27.7	24	36	73 ± 5
α , Å ²	5.33	116.74	7.2	7.2	25	84 ± 8

The three-band $\mathbf{k} \cdot \mathbf{p}$ model allows for the states of the conduction band Γ_6 with the Bloch functions S ; valence band $\Gamma_8 + \Gamma_7$ with functions X, Y, Z ; and the higher band $\Gamma_{8c} + \Gamma_{7c}$ with functions X', Y', Z' . These states at $k = 0$

correspond to $E_{\Gamma_6} = 0$, $E_{\Gamma_8} = -E_g$, $E_{\Gamma_7} = -(E_g + \Delta)$, $E_{\Gamma_{7c}} = -E'_g$, $E_{\Gamma_{8c}} = -E'_g + \Delta'$, $P = (i\hbar/m_0)\langle S|p_z|Z\rangle$, $P' = (i\hbar/m_0)\langle S|p_z|Z'\rangle$, and $Q = (i\hbar/m_0)\langle X|p_z|Z'\rangle$ (interband matrix elements); $\mathbf{p} = -i\hbar\nabla$.

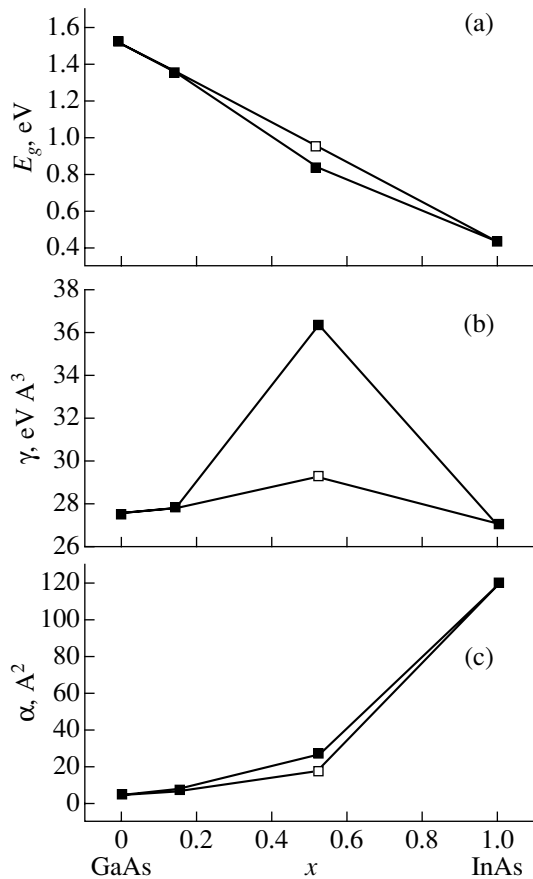


Fig. 7. Dependences $E_g(x)$ (a), $\gamma(x)$ (b), and $\alpha(x)$ (c) on the In concentration (x) in the $\text{In}_x\text{Ga}_{1-x}\text{As}$ solid solution according to the data of [11] and their linear extrapolation (unshaded squares). The same dependences, but with the use of the value $E_g = 0.8215$ eV known for $x = 0.53$ [26] (shaded squares).

The linear extrapolation of the dependence $E_g(x)$ yields the value $E_g = 0.94$ eV (Fig. 7a, unshaded squares). However, the experimental value $E_g = 0.8215$ eV was determined to a high accuracy in [26] (Fig. 7a, shaded squares). Such a moderate “sag” of the dependence $E_g(x)$ causes a significant increase in the coefficient γ for the $\text{In}_{0.53}\text{Ga}_{0.47}\text{As}$ solid solution (Fig. 7b). The parameters determined for $\text{In}_{0.53}\text{Ga}_{0.47}\text{As}$ are listed in Table 2 together with the data of [11].

As a result, we obtain theoretical estimates of $\gamma \approx 36$ Å³ eV and $\alpha \approx 25$ Å² for $x = 0.53$. These values differ from those determined by fitting dependence (14) to the experimental data by a factor of 2–3 (see Table 2). However, it is known that other parameters of the band structure, except for E_g , can nonlinearly depend on the solid solution composition at the center of the interval $x = 0-1$.

The linear extrapolation is much more accurate at the beginning of this interval ($x = 0.15$). Therefore, it is not surprising that the calculated and experimental data for γ and α in [11] virtually coincide. Furthermore, the band parameters near the GaAs/ $\text{In}_{0.15}\text{Ga}_{0.85}\text{As}$ heteroboundary (studied in [11]) and near the InP/ $\text{In}_{0.53}\text{Ga}_{0.46}\text{As}$ heteroboundary can differ due to different lattice constants on either side of the heteroboundary. Finally, it is most probable that the heteroboundary defect structure was significantly modified, as well as the lattice strain, after repeated cooling-illumination-heating cycles, to which the samples were exposed. As a result, the energy band parameters, on which the coefficients γ and α depend, could also change.

5. CONCLUSION

The quantum magnetoresistance of two-dimensional electron gas at the $\text{In}_{0.53}\text{Ga}_{0.47}\text{As}/\text{InP}$ heteroboundary was studied in the persistent photoconductivity state. The sign-alternating magnetoresistance in a weak (100 G) magnetic field is indicative of the influence of the spin-orbit interaction on the quantum well conductivity.

It was shown that a major contribution to the spin-orbit scattering frequency $1/\tau_{\text{so}}$ is made by the mechanism controlled by the electric field built in at the heteroboundary; i.e., the Rashba mechanism linear with respect to the electron wave vector. The data obtained allowed us to estimate the parameters of the spin-orbit splitting of the energy spectrum on the basis of available theories as $\alpha = (84 \pm 4) \text{ \AA}^2$ (according to the Rashba mechanism) and $\gamma = (73 \pm 3) \text{ eV \AA}^3$ (according to the Dyakonov-Perel and Dresselhaus mechanisms). The dephasing frequency of the electron wave function is defined by the sum of electron-electron interaction frequencies characteristic of perfect and disordered two-dimensional Fermi liquids.

ACKNOWLEDGMENTS

This study was supported in part by the federal program (the Ministry of Science and Industry) "Physics of Solid-State Nanostructures".

REFERENCES

1. N. V. Agrinskaya, V. I. Kozub, and T. A. Polyanskaya, *Phys. Status Solidi B* **218** (1), 68 (2000).
2. B. I. Shklovskii and A. L. Efros, *Electronic Properties of Doped Semiconductors* (Nauka, Moscow, 1979; Springer-Verlag, New York, 1984).
3. A. C. Beer, *Galvanomagnetic Effects in Semiconductors* (Academic, New York, 1963), *Solid State Physics*, Suppl. 4.
4. B. L. Altshuler, A. G. Aronov, A. I. Larkin, and D. E. Khmel'nitskii, *Zh. Éksp. Teor. Fiz.* **81** (8), 768 (1981) [*Sov. Phys. JETP* **54**, 411 (1981)].
5. B. L. Altshuler and A. G. Aronov, *Electron-Electron Interaction in Disorderd Systems*, Ed. by A. L. Efros and M. Pollak (North-Holland, Amsterdam, 1985); *Modern Problems in Condensed Matter Sciences*, Vol. 10, p. 1.
6. T. A. Polyanskaya and Yu. V. Shmartsev, *Fiz. Tekh. Poluprovodn. (Leningrad)* **23** (1), 3 (1989) [*Sov. Phys. Semicond.* **23**, 1 (1989)].
7. A. M. Paalanen, D. C. Tsui, and J. C. M. Hwang, *Phys. Rev. Lett.* **51** (24), 2226 (1983).
8. S. Hikami, A. I. Larkin, and Y. Nagaoka, *Prog. Theor. Phys.* **44** (2), 707 (1980).
9. P. D. Dresselhaus, C. M. Papavassiliou, R. G. Wheeler, and R. N. Sacks, *Phys. Rev. Lett.* **68** (1), 106 (1992).
10. S. V. Iordanskii, Yu. B. Lyanda-Geller, and G. E. Pikus, *Pis'ma Zh. Éksp. Teor. Fiz.* **60** (3), 199 (1994) [*JETP Lett.* **60**, 206 (1994)].
11. W. Knap, C. Skierbiszewski, A. Zduniak, *et al.*, *Phys. Rev. B* **53**, 3912 (1996).
12. A. I. Larkin, *Pis'ma Zh. Éksp. Teor. Fiz.* **31**, 239 (1980) [*JETP Lett.* **31**, 219 (1980)].
13. Zh. I. Alferov, A. T. Gorelenok, V. V. Mamutin, *et al.*, *Fiz. Tekh. Poluprovodn. (St. Petersburg)* **18** (11), 1999 (1984) [*Sov. Phys. Semicond.* **18**, 1247 (1984)].
14. M. I. D'yakonov and Yu. Yu. Kachorovskii, *Fiz. Tekh. Poluprovodn. (Leningrad)* **20**, 210 (1986) [*Sov. Phys. Semicond.* **20**, 110 (1986)].
15. Yu. L. Bychkov and E. I. Rashba, *J. Phys. C* **17**, 6093 (1984).
16. L. V. Golubev, A. M. Kreshchuk, S. V. Novikov, *et al.*, *Fiz. Tekh. Poluprovodn. (Leningrad)* **22** (11), 1948 (1988) [*Sov. Phys. Semicond.* **22**, 1234 (1988)].
17. N. A. Bert, V. V. Vorob'eva, M. V. Vorontsova, *et al.*, *Fiz. Tekh. Poluprovodn. (Leningrad)* **24** (4), 653 (1990) [*Sov. Phys. Semicond.* **24**, 410 (1990)].
18. D. D. Bykanov, A. M. Kreshchuk, S. V. Novikov, *et al.*, *Fiz. Tekh. Poluprovodn. (St. Petersburg)* **32** (9), 1100 (1998) [*Semiconductors* **32**, 985 (1998)].
19. I. G. Savel'ev and T. A. Polyanskaya, *Fiz. Tekh. Poluprovodn. (Leningrad)* **22** (10), 1818 (1988) [*Sov. Phys. Semicond.* **22**, 1150 (1988)].
20. B. L. Altshuler, A. G. Aronov, and D. E. Khmel'nitskii, *J. Phys. C* **15**, 7367 (1982).
21. H. Fukuyama and E. Abrahams, *Phys. Rev. B* **27** (10), 5976 (1983).
22. V. Karpus, *Fiz. Tekh. Poluprovodn. (Leningrad)* **22** (3), 439 (1988) [*Sov. Phys. Semicond.* **22**, 268 (1988)].
23. I. L. Drichko, A. M. D'yakonov, V. D. Kagan, *et al.*, *Fiz. Tekh. Poluprovodn. (St. Petersburg)* **31** (11), 1357 (1997) [*Semiconductors* **31**, 1170 (1997)].
24. D. D. Bykanov, A. M. Kreshchuk, S. V. Novikov, *et al.*, in *Proceedings of the 24th International Conference on the Physics of Semiconductors, Jerusalem, Israel, 1999*, Ed. by D. Gershenson (World Scientific, Singapore, 1999), CD-ROM, Papers No. 0219.
25. T. Ando, *Rev. Mod. Phys.* **54** (2), 437 (1982).
26. E. Zelinski, H. Schweizer, K. Sruebel, *et al.*, *J. Appl. Phys.* **59** (6), 2196 (1986).

Translated by A. Kazantsev

PHYSICS OF SEMICONDUCTOR DEVICES

Isotope-Pure ^{28}Si Layers Grown by VPE

O. N. Godisov*, A. K. Kaliteevsky*, A. Yu. Safronov*, V. I. Korolev**,
P. N. Aruev***, B. Ya. Ber***, V. Yu. Davydov***, N. V. Zabrodskaya***,
V. V. Zabrodsky***, M. A. Kaliteevsky***, P. S. Kop'ev***,
A. P. Kovarsky***, and V. L. Sukhanov***

* *Elektromekhanicheskii Zavod Production Association, Tsentrobezhnye Tekhnologii Scientific and Technological Center, St. Petersburg, 198096 Russia*

** *Radiyevyi Institute im. G. V. Khlopina Scientific and Production Association, St. Petersburg, 194021 Russia*

*** *Ioffe Physicotechnical Institute, Russian Academy of Sciences, St. Petersburg, 194021 Russia*

Submitted April 26, 2002; accepted for publication May 15, 2002

Abstract—Vapor-phase epitaxy was used to grow Si layers enriched to 99.96% with ^{28}Si isotope. Secondary-ion mass spectrometry and Raman spectroscopy were used to demonstrate the high quality of the epitaxial material obtained. © 2002 MAIK “Nauka/Interperiodica”.

Natural silicon is a mixture of three stable isotopes with atomic masses of 28 amu (content 92.21%), 29 amu (4.70%), and 30 amu (3.09%). The use of isotope-pure silicon opens up additional opportunities for the development of new silicon-based semiconductor devices and the improvement of properties of already existing devices. This is due to the higher heat conductivity of isotope-pure silicon [1, 2]; to the possibility of achieving a uniform dopant distribution with abrupt boundaries of the doped region by neutron transmutation doping [3, 4], which rules out diffusion-related redistribution of the impurity introduced, characteristic of conventional technologies; and to prospects for the development of components for a quantum computer based on solid-state isotope heterostructures [5, 6].

The aim of this study was to develop a technology for the deposition of epitaxial layers of isotope-pure silicon using vapor-phase epitaxy. The silicon isotopes were separated by centrifuging [7]. The silicon tetrafluoride employed in isotope separation was processed into silane via nucleophilic substitution [7].

The epitaxial growth was carried out in a vertical water-cooled glass reactor with induction heating. Substrates were placed on the lateral faces of a graphite pyramid.

Epilayers were grown in an atmosphere of purified hydrogen at 1100°C from a mixture of 4% silane ($^{28}\text{SiH}_4$) and 96% argon from the reaction $\text{SiH}_4 \rightarrow \text{Si} + 2\text{H}_2$. Single-crystal wafers of KEF-20 silicon 350 μm thick (*n*-type Si with resistivity of 20 $\Omega\text{ cm}$) with [100] orientation served us substrates.

The distribution of concentrations of various silicon isotopes across the thickness of a grown layer was determined using secondary-ion mass spectrometry (SIMS) with a CAMECA IMS4f secondary-ion microprobe. The secondary emission of analytical ions of the

isotopes, Si^- , was excited by bombarding an epilayer with 14.5 keV Cs^+ ions. The measurements were made in the high-mass-resolution mode ($M/\Delta M = 3500$), which ensured that the analytical signal of secondary Si^- ions was reliably distinguished from SiH^- clusters with a similar mass.

Figure 1 shows concentration profiles of ^{28}Si , ^{29}Si , and ^{30}Si isotopes across a 2.6- μm -thick layer grown from a crystalline substrate of natural unenriched silicon. The relative concentrations of the silicon isotopes in the substrate correspond to those in natural silicon. The content of ^{29}Si and ^{30}Si isotopes in the epilayer is more than 2 orders of magnitude lower: the epilayer

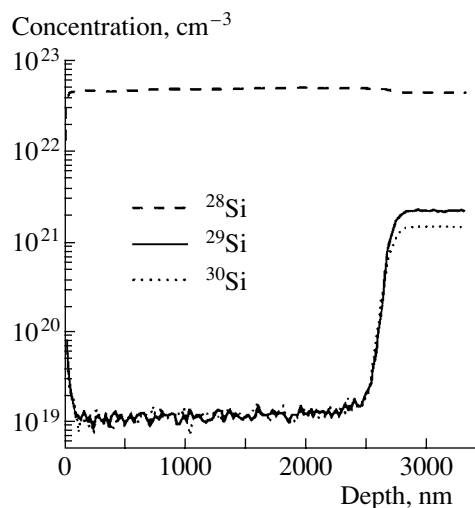


Fig. 1. Concentration profile of ^{28}Si , ^{29}Si , and ^{30}Si silicon isotopes in an isotope-enriched layer grown on a substrate with natural isotopic composition.

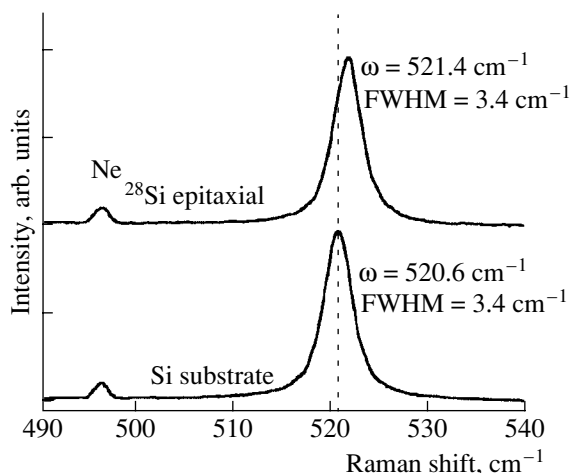


Fig. 2. Raman spectra of an isotope-enriched layer, sample Z1. The spectrum of a substrate with natural isotopic composition is given for comparison. $T = 300$ K.

contains 99.96% ^{28}Si (which is presently the world record [8]) and 0.02% of both ^{29}Si and ^{30}Si .

Figure 2 presents Raman spectra obtained for an isotope-pure ^{28}Si layer and, for comparison, that of a single-crystal substrate with natural isotopic composition. The Raman spectra were measured using an automated spectral installation based on a DFS-24 double-grating monochromator. The spectral width of the slit was 1 cm^{-1} . All the spectra were recorded in the backscattering mode at room temperature. The spectra were excited by the 488-nm line of an argon-ion laser with an incident power of 30 mW in a $50\text{-}\mu\text{m}$ spot.

It can be seen that the line of the isotope-pure ^{28}Si is shifted relative to that of natural silicon to higher frequencies. Such behavior is in agreement with the dependence of the phonon frequency on the mass, $\omega(\mathbf{k}) \propto$

$\bar{M}^{-1/2}$, and with the fact that natural silicon is a mixture of three stable isotopes with atomic masses of 28, 29, and 30 amu.

Thus, isotope-pure ^{28}Si layers with a record-breaking isotopic purity of 99.96% and high crystal perfection were obtained.

ACKNOWLEDGMENTS

This study was supported in part by the International Science and Technology Center (project no. 1354), the Russian Foundation for Basic Research (grant no. 02-02-17605), and the Ministry of Science and Technology of the Russian Federation (project "Physics of Solid-State Nanostructures: Methods for the Integrated Diagnostics of Nanostructures").

REFERENCES

1. W. S. Capinski, H. J. Maris, E. Bauser, *et al.*, *Appl. Phys. Lett.* **71** (15), 2109 (1997).
2. T. Ruf, R. W. Henn, M. Asen-Palmer, *et al.*, *Solid State Commun.* **115** (5), 243 (2000).
3. M. G. Gornov, O. M. Grebennikova, Y. B. Gurov, *et al.*, *Instrum. Exp. Tech.* **33** (3), 554 (1990).
4. A. N. Brykalov, E. I. Ignatenko, M. L. Kozhukh, *et al.*, *At. Énerg.* **65** (1), 558 (1988).
5. B. E. Kane, *Nature* **393**, 133 (1998).
6. A. A. Larionov, L. E. Fedichkin, A. A. Kokin, and K. A. Valiev, *Nanotechnology* **11** (4), 392 (2000).
7. O. N. Godisov, A. K. Kaliteevskii, V. I. Korolev, *et al.*, *Fiz. Tekh. Poluprovodn. (St. Petersburg)* **35** (8), 913 (2001) [*Semiconductors* **35**, 877 (2001)].
8. H. Bracht, E. E. Haller, and R. Clark-Phelps, *Phys. Rev. Lett.* **81** (2), 393 (1998).

Translated by M. Tagirdzhanov

**PHYSICS
OF SEMICONDUCTOR DEVICES**

Isotope-Pure Silicon Layers Grown by MBE

O. N. Godisov*, A. K. Kaliteevsky*, A. Yu. Safronov*, V. I. Korolev,
B. Ya. Ber***, V. Yu. Davydov***, D. V. Denisov***, M. A. Kaliteevsky***,
P. S. Kop'ev***, A. P. Kovarsky***, V. M. Ustinov***, and H.-J. Pohl******

* *Elektromekhanicheskii Zavod Production Association, Tsentrezhnye Tekhnologii Scientific and Technological Center,
St. Petersburg, 198096 Russia*

** *Kholpin Radium Institute Scientific and Production Association, St. Petersburg, 194021 Russia*

*** *Ioffe Physicotechnical Institute, Russian Academy of Sciences, St. Petersburg, 194021 Russia*

**** *VITCON Projectconsult GmbH, D-07745 Jena, Germany*

Submitted May 17, 2002; accepted for publication May 17, 2002

Abstract—Molecular-beam epitaxy with a solid source was used to grow silicon layers enriched with ^{28}Si and ^{30}Si isotopes to 99.93 and 99.34%, respectively. Secondary-ion mass spectrometry and Raman scattering spectroscopy were applied to demonstrate the high isotopic purity and crystal perfection of the layers obtained. © 2002 MAIK “Nauka/Interperiodica”.

Natural silicon is a mixture of three stable isotopes: ^{28}Si (92.23%), ^{29}Si (4.67%), and ^{30}Si (3.10%). The use of silicon with a monoisotopic composition allows for the solution of a number of important technological problems, such as heat removal in semiconductor devices [1] and fabrication of heavily doped *n*-type substrates with uniform impurity distribution [2]. Heterostructures with isotopes can be used as a basis for the development of a prototype quantum computer [3]. Recently, layers of isotope-pure silicon have been obtained by vapor-phase epitaxy [4, 5] and molecular-beam epitaxy (MBE) with a gaseous source [6]. The present study is concerned with the further development of the technology for the growth of isotope-pure silicon layers by MBE with a solid source.

Silicon isotopes were separated via centrifuge technology using silicon tetrafluoride [7]. Then, isotope-enriched silicon tetrafluoride was processed into silane by nucleophilic substitution [7]. Polycrystalline silicon was produced by pyrolysis of silane and charged into the sources in an MBE machine.

The MBE growth was carried out on a Riber Supra-32MBE machine whose growth chamber was equipped with three electron-beam evaporators (one of these had three crucibles for different materials) and four effusion sources. The analytical part of the growth chamber includes a quadrupole mass spectrometer, a Bayard–Alpert pressure gauge, and a device for measuring reflection high-energy electron diffraction (RHEED). The machine includes an analytical chamber equipped with an apparatus for Auger and X-ray photoelectron (XPS) spectroscopies and a transporting system for sample motion between the chambers without impairing the ultrahigh vacuum conditions. The residual pressure in the growth chamber did not exceed 3×10^{-10} Torr,

and during deposition of epitaxial silicon layers the pressure increased to about 1×10^{-8} Torr.

The structures studied were grown on *n*-type (100)Si substrates with a dopant concentration of $2 \times 10^{15} \text{ cm}^{-3}$. The substrates were subjected to chemical pretreatment using the Shiraki method [8]. Immediately after the chemical pretreatment was complete, the substrates were charged into the lock chamber of the machine, which was evacuated to ultrahigh vacuum. The pre-epitaxial treatment of the substrates in the growth chamber consisted of their stepwise degassing at 450 and 750°C and the subsequent sublimation of a thin ($\sim 10\text{--}15 \text{ \AA}$) protective layer of silicon oxides under a weak flux of Si atoms ($\sim 10^{13} \text{ atom cm}^{-2} \text{ s}^{-1}$) at 750°C. After the oxide removal, a streaky RHEED pattern was observed, which indicated that a clean, atomically smooth silicon surface had been obtained. The lack of contamination and microscopic roughness in the case of such substrate pretreatment was confirmed by studying the surface of control samples using XPS *in situ* and scanning electron microscopy *ex situ*.

Monoisotopic ^{28}Si and ^{30}Si films were grown by electron-beam evaporation of polycrystalline ^{28}Si and ^{30}Si ingots placed in molybdenum crucibles of the three-section electron-beam evaporator. The growth rate of an epitaxial film was 0.2 Å/s; the epitaxial growth took place at a substrate temperature of 620°C and was monitored with an Ircon-V IR pyrometer and a standard W–Re thermocouple. Figure 1 presents a typical RHEED pattern observed during growth. The two-dimensional (2D) nature of the diffraction pattern and the presence of superstructural reflections suggest a 2D nature of the epitaxial growth of monoisotopic silicon and indicate that the films obtained have an atomically smooth and atomically clean surface.

The concentration distribution of silicon isotopes across the layers grown was studied by secondary-ion mass spectrometry with a CAMECA IMS4f secondary-ion microprobe. The secondary emission of analytical ions of silicon isotopes, Si^- , was excited by bombarding an epilayer with 14.5 keV Cs^+ ions. The high-mass-resolution mode was employed ($M/\Delta M = 3500$), which ensured that the analytical signals of secondary Si^- ions were reliably distinguished from those of SiH^- clusters with approximately the same mass.

Figure 2a presents concentration profiles of the silicon isotopes across a film enriched with the ^{30}Si isotope and which was grown on a crystalline silicon substrate with a natural isotopic composition. The thickness of the layer is 270 nm, and its ^{30}Si isotopic purity, 99.30 at. %. The content of the ^{29}Si isotope is a factor of 10 lower and constituted 0.52 at. %; that of the ^{28}Si isotope is a factor of 500 lower (0.18 at. %) as compared with its natural content.

Figure 2b presents concentration profiles of silicon isotopes across a layer enriched with the ^{28}Si isotope and that was grown on a crystalline silicon substrate with a natural isotopic composition (i.e., with the relative content of the silicon isotopes in the substrate corresponding to that in natural silicon). The figure reveals a distinct boundary between the layer with a thickness of about 370 nm and the substrate. The isotopic purity of the ^{28}Si layer is 99.93 at. %. The content of ^{29}Si and ^{30}Si isotopes is more than a factor of 100 lower than in the natural case—0.04 and 0.03 at. %, respectively.

Figure 3 shows Raman spectra of isotope-pure ^{28}Si and ^{30}Si layers and, for comparison, the spectrum of a single-crystal substrate with a natural isotopic composition. The Raman spectra were measured using an automated spectral installation based on a DFS-24 double-grating monochromator. The spectral width of the slit was 1 cm^{-1} . All the spectra were recorded in the backscattering mode at room temperature. Excitation was performed with the 488-nm line of an argon-ion laser, with an incident power of 30 mW in a $50\text{-}\mu\text{m}$ spot.

For silicon with natural isotopic composition, which is a mixture of three stable isotopes with atomic masses of 28, 29, and 30 amu and an average atomic mass of 28.086 amu, the optical phonon frequency is 520.6 cm^{-1} , as shown in Fig. 3. The dependence of the phonon frequency on the average mass of atoms in a crystal must have the form $\omega(\mathbf{k}) \propto \bar{M}^{-1/2}$. The spectrum obtained by studying a ^{30}Si epilayer shows two lines. One of these has a frequency of 520.6 cm^{-1} , which corresponds to Raman scattering in a single-crystal silicon substrate with natural isotopic composition. The other line, which shifted to lower frequencies (503.8 cm^{-1}), corresponds to the ^{30}Si epilayer. The widths of both lines are 3.3 cm^{-1} , which confirms the high crystal perfection of the epilayer. The phonon line of the ^{28}Si layer



Fig. 1. RHEED pattern observed during epitaxial growth of monoisotopic silicon films. Direction of electron beam incidence: $[011]$; energy of electrons in the beam: 10 keV.

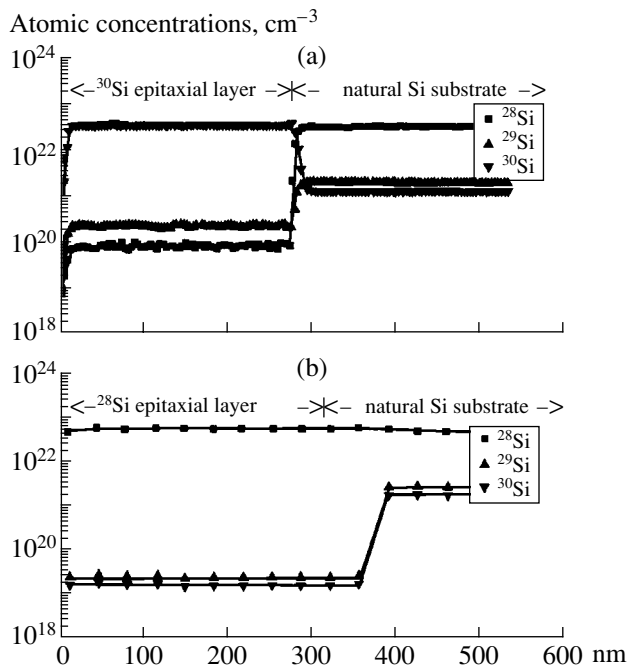


Fig. 2. Concentration profiles of ^{28}Si , ^{29}Si , and ^{30}Si silicon isotopes in isotope-enriched layers of (a) ^{30}Si and (b) ^{28}Si grown on silicon substrates with natural isotopic composition. Isotopic composition of epilayers: (a) ^{28}Si 0.18, ^{29}Si 0.52, and ^{30}Si 99.30 at. %; (b) ^{28}Si 99.93, ^{29}Si 0.04, and ^{30}Si 0.03.

is shifted to higher frequencies relative to that of natural silicon and has a frequency of 521.1 cm^{-1} . It should be noted that the influence exerted by the substrate on the spectrum observed is weaker when the layer is thicker and when the frequency of the exciting radiation is higher; this is accounted for by the absorption of light in the layer.

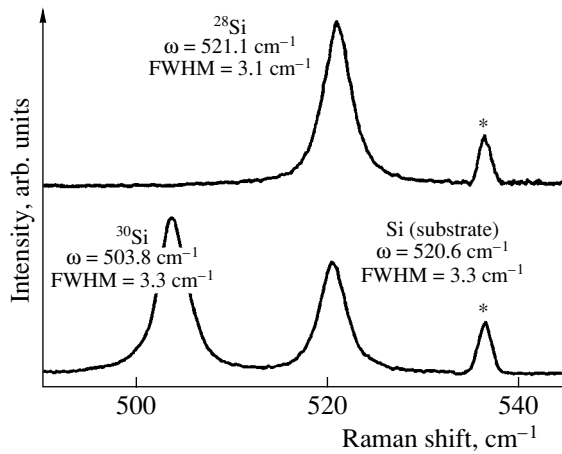


Fig. 3. Raman spectra of ^{28}Si and ^{30}Si epilayers. The spectral feature denoted by the asterisk corresponds to the emission of the neon Heusler lamp used to calibrate the monochromator. $T = 300$ K.

To conclude, the MBE technique with a solid source was successfully employed to obtain isotope-pure ^{28}Si and ^{30}Si epilayers with an isotopic purity of 99.96 and 99.34%, respectively, and high crystal perfection.

ACKNOWLEDGMENTS

We thank S.A. Smirnov and I.N. Goncharuk for the Raman measurements.

This study was supported by the International Science and Technology Center (project no. 1354), the Russian Foundation for Basic Research (grant no. 02-02-17605), and the Ministry of Science and Technology of the Russian Federation (project “Physics of Solid-State Nanostructures: Methods for the Integrated Diagnostics of Nanostructures”).

REFERENCES

1. T. Ruf, R. W. Henn, M. Asen-Palmer, *et al.*, *Solid State Commun.* **115**, 243 (2000).
2. M. L. Kozhukh, *Nucl. Instrum. Methods Phys. Res. A* **329**, 453 (1993).
3. B. E. Kane, *Nature* **393**, 133 (1998).
4. Y. Nakabayashi, T. Segawa, H. I. Osman, *et al.*, *Jpn. J. Appl. Phys.* **39**, L1133 (2000).
5. H. Bracht, E. E. Haller, and R. Clark-Phelps, *Phys. Rev. Lett.* **81**, 393 (1998).
6. A. Ural, P. B. Griffin, and J. D. Plummer, *Appl. Phys. Lett.* **73** (12), 1706 (1998).
7. O. N. Godisov, A. K. Kaliteevskii, V. I. Korolev, *et al.*, *Fiz. Tekh. Poluprovodn. (St. Petersburg)* **35** (8), 913 (2001) [*Semiconductors* **35**, 877 (2001)].
8. A. Ishizaka and Y. Shiraki, *J. Electrochem. Soc.* **133**, 666 (1986).

Translated by M. Tagirdzhanov